Stony Brook University

Structural Studies from Powder Diffraction

A Dissertation Presented

by

Kevin Hunter Stone

to

The Graduate School

in Partial Fulfillment of the Requirements

for the Degree of

Doctor of Philosophy

in

Physics

Stony Brook University

December 2009

Stony Brook University

The Graduate School

Kevin Hunter Stone

We, the dissertation committee for the above candidate for the Doctor of Philosophy degree, hereby recommend acceptance of this dissertation.

Peter W. Stephens – Dissertation Advisor
Professor, Department of Physics and Astronomy

Thomas Weinacht – Chairperson of Defense
Associate Professor, Department of Physics and Astronomy

Maria Victoria Fernandez-Serra
Assistant Professor, Department of Physics and Astronomy

Eric Dooryhee
Powder Diffraction Group Leader
National Synchrotron Light Source II, Brookhaven National Laboratory

This dissertation is accepted by the Graduate School.

Lawrence Martin
Dean of the Graduate School

Abstract of the Dissertation

Structural Studies from Powder Diffraction

by

Kevin Hunter Stone

Doctor of Philosophy

in

Physics

Stony Brook University

2009

In the fast moving field of new materials, it is often impossible to make samples of high quality at an early stage. As a result, most samples are first available in the form of powders, single crystals being available only after a great deal of additional effort. Fortunately, the art of powder diffraction has advanced to a degree that structural information may be readily obtained, even from the first, not yet ideal, samples.

Structure determination from powder diffraction is becoming an incredibly powerful tool, applicable to a wide array of materials. Its use extends from characterizing polymorphic forms of small organic molecules to determining the structure of organo-metallic

network structures such as the magnetic and semiconducting materials discussed in this work. In this work, we have studied the polymorphic forms of 2-chloro-4-nitrobenzoic acid in the search for what was thought to be an elusive form, discovering instead a curious thermal expansion behavior. It has also been used in determining the structure of a polymorph of *p*-methylchalcone and one of *p*′-methylchalcone. Powder diffraction has also proven quite useful in the realm of organo-metallic network structures. We have studied examples such as analogues of II-VI and IV-VI semicondutors and organic-based magnets, in which the magnetic interaction of transition metals is mediated by unpaired *s* or *p* electrons on organic acceptor molecules. The crystal structure of these materials is crucial to form a basis for understanding the interactions which give rise to the overall behavior. Further, the structure determination has proven to be critical for determining the precise composition of the materials which have been produced.

Refinement of a structure is generally the last step in the structure solution process in crystallography. When dealing with powder diffraction data, this usually means Rietveld refinement, in which the entire pattern is fit with each measured data point being treated as an independent measurement and the model being refined to minimize the usual χ^2 metric. However, such a process is predicated on the assumption that the model under consideration is a complete representation of the system from which the data

is derived. A common complication in powder diffraction is the presence of unknown impurities, which result in spurious peaks in the diffraction pattern and cannot be accounted for by a model of only a single structure.

Using the ideas of Bayesian statistics, it is possible to deal with impurity contributions without the need for any information as to what constitutes the impurity. In this approach, the usual χ^2 statistic is modified to associate a smaller penalty with a model which underestimates the data, as the missing intensity may be due to an impurity which is not included in the model under consideration. This has been implemented through an iterative reweighting of the data at each step of the refinement. In the last chapter of this dissertation, we describe the implementation of this technique and its use in solving structures which were originally unobtainable in pure forms.

To my Grandma Mary.

Contents

List of Figures

List of Tables

Acknowledgements

First of all, none of this would have been possible without the constant support of my advisor Peter Stephens. I have always appreciated his guidance, whether in his capacity as an advisor, a collaborator, or as a friend.

I would also like to acknowledge the participation and contributions from my many collaborators. Jae-Hyuk Her and Saul Lapidus, my fellow graduate students, who were always available for useful discussions on hard problems. And our many outside collaborators, for providing those hard problems, and many others besides, in the form of interesting samples to work on. None of this would have been possible without their hard work. I would also like to thank the staff at both the NSLS and the physics and astronomy department at Stony Brook who have kept things running, especially Pat Peiliker for all of her extraordinary help.

On a more personal note, I am extremely grateful for the unfailing support of my family and friends. I would especially like to thank my parents, who have encouraged me every step of the way throughout my many long years of school. I have also been blessed with some truly amazing friends who have been both a constant comfort and a challenge to me in my attempt to be deserving of their friendship. This is especially true of Ariane Kretlow, who has provided

such an incredible example. I also owe a great deal of appreciation to Diane Lee, for giving me so much support and helping to keep me grounded as this work has come to an end.

Chapter 1

Introduction

One of the central tenets of condensed matter physics, or indeed almost any of the investigative sciences, is that: in order to understand how something behaves, we must understand how it is put together. In the case of materials, this is commonly done through the use of X-ray diffraction as a means of determining crystalline structures. Although the phenomena of diffraction was well known, it was the pioneering work of von Laue, which demonstrated both the wave nature of X-rays and the lattice structure of crystals, and of William Henry and William Lawrence Bragg in determining the relation between the X-ray wavelength, distance between planes of atoms, and the angle through which the X-rays are diffracted, which ushered in the age of crystallography as we know it today.

$$\lambda = 2d \sin \theta \tag{1.1}$$

It is this relation, equation 1.1, known as Bragg's law, which most suc-

Figure 1.1: Schematic representation of Bragg's law.

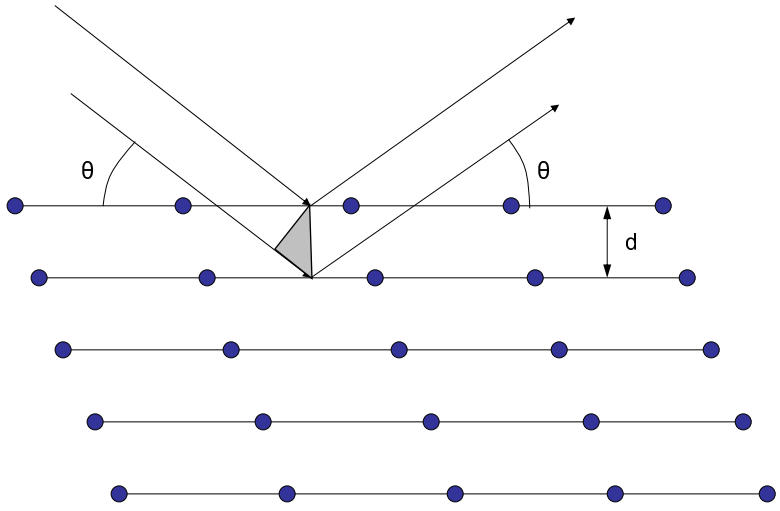

cinctly summarizes X-ray crystallography. Consider planes of atoms separated by some distance d. If a wave of X-rays is incident upon these planes at some angle θ, the wave will be partially reflected and partially transmitted by each plane. The difference in path length will result in a relative phase shift between waves which have been reflected from different planes, creating interference. Bragg's law predicts the points at which such interference will be constructive, giving rise to peaks in observed X-ray intensity. Such a configuration is illustrated in Figure 1.1. Of course, the X-rays, in actuality, scatter from isolated atoms, not planes, and so we must consider the scattering from point-like sources instead, Figure 1.2. What is then observed is the superposition of scattered X-rays from all of the atoms. Since the atoms are arranged in a regular lattice, the superposition is also regular and can be gotten *via* a

Fourier transform, *vida infra*.

Figure 1.2: Schematic representation of the interference from point scatterers.

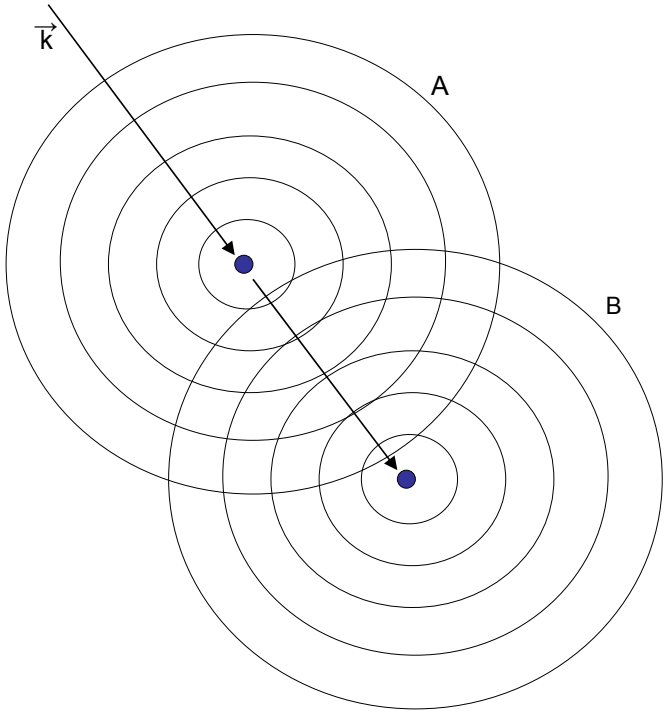

$$A = \mathrm{e}^{2\pi i \vec{k}\cdot\vec{r}_A}$$

$$B = \mathrm{e}^{2\pi i \vec{k}\cdot\vec{r}_B}$$

Summing over all atoms in the sample, what we will observe is simply

$$F = \sum_j \mathrm{e}^{2\pi i \vec{k}\cdot\vec{r}_j} \tag{1.2}$$

where j runs over all atoms. Of course, summing over all atoms in the sample is impossibly cumbersome, and makes no use of the regularity of the crystal lattice. Instead, we would prefer to sum over the contribution from only those atoms within a unit cell. Under the assumption of a regular crystal lattice, if we consider two atoms which interfere constructively, (A and B) then a third atom, C, displaced from B similar to B's displacement from A, it is obvious that B and C must interfere constructively if A and B do, and therefore so must A and C. We therefore let this displacement be one of our lattice vectors, Figure 1.3, and note that any integer combination of such displacements will not affect the means of interference. So, we evidently need to sum only over those atoms in the unit cell, all others becoming redundant, leading to

$$F = \sum_j \mathrm{e}^{2\pi i \vec{k}\cdot\vec{r}_j} \tag{1.3}$$

where j now sums over only those atoms in the unit cell.

Of course, it is the electrons of an atoms which actually cause the scattering, and so naturally different atoms, with different numbers of electrons, will scatter to various extents. We may include this by modifying our formula to

$$F = \sum_j f_j \mathrm{e}^{2\pi i \vec{k}\cdot\vec{r}_j} \tag{1.4}$$

where f_j is the scattering power for atom j. Clearly, now, the scattering is simply the discrete Fourier transform of the crystal structure. At this point, one may include other considerations, such as the thermal motion of the electrons which will serve to "smear out" the idealized point-like atom. This is

Figure 1.3: Schematic representation of the lattice translations between point scatterers.

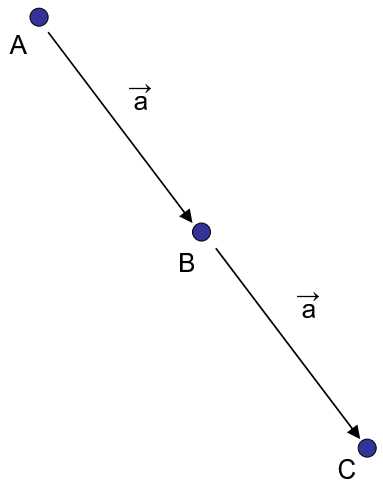

ordinarily included through a Debye-Waller factor which models this smearing as a Gaussian distribution of the electrons about their idealized point. Although such considerations play an important role in practice, we will neglect them here for the sake of clarity.

F is, of course, dependent upon where we are looking, and in the case of a single crystal, this results in well determined peaks called Bragg spots. These may be identified by the integer combination of lattice vectors (termed Miller indices) which give rise to them. If we were able to then measure F for these Bragg spots, a simple inverse Fourier transform would recover the starting

structure. However, in reality, what we are capable of measuring is not F, but only $|F^2|$, resulting in a loss of phase information. The recovery of this phase information is the classical problem of crystallography. In the case of powder samples, all angular information as to the sample orientation is lost, from which a loss of angular information in the diffraction pattern naturally follows. In essence, this means that a powder diffraction pattern is the integration over angle of the single crystal pattern. It is this collapse of three dimensions of information down to one, compounded with the loss of phase information, which poses the fundamental challenge in powder diffraction. The so called "phase problem" has been solved in a number of ways, but for the purposes of this thesis, we will focus on only three, these being direct methods, simulated annealing, and charge flipping.

1.1 Direct Methods

One of the earliest methods of phase retrieval was developed by Karle and Hauptman and termed by them direct methods, as the phases are determined directly from the experimentally observed amplitudes through mathematical relationships. While the scattering of X-rays is related to the electron density of a crystal structure, and vice versa, by the Fourier transform, in general the Fourier coefficients are complex numbers. However, in a diffraction experiment, only the magnitudes of these complex coefficients are obtained from the measured intensities. Thus we are faced with the problem of how to reconstruct a charge density directly from measured intensities. It is well known [1] that the Fourier coefficients of a positive definite function will obey certain

relations. Karle and Hauptman [2], working from the assumption that the charge density map must everywhere be positive, were able to derive relations among the structure factors of the form

$$\begin{vmatrix} F_{000} & F_{-k1} & F_{-k2} & \cdots & F_{-h} \\ F_{k1} & F_{000} & F_{k1-k2} & \cdots & F_{k1-h} \\ F_{k2} & F_{k2-k1} & F_{000} & \cdots & F_{k2-h} \\ \vdots & \vdots & \vdots & \ddots & \vdots \\ F_{h} & F_{h-k1} & F_{h-k2} & \cdots & F_{000} \end{vmatrix} \geq 0. \tag{1.5}$$

Here all the structure factors forming the first row are of arbitrary index except for F_{000}, which is the total scattering power in the unit cell. As examples, we will briefly investigate the results of the two simplest cases. For $n = 1$, we have simply

$$F_{000} \geq 0, \tag{1.6}$$

which is the trivial result that the total scattering power must be positive. For $n = 2$ we have

$$\begin{vmatrix} F_{000} & F_{-h} \\ F_{h} & F_{000} \end{vmatrix} \geq 0 \Rightarrow F_{000} \geq F_h, \tag{1.7}$$

where we have used the property of Friedel pairs that $F_h = -F_{-h}$. Again, a trivial result that all structure factors will be smaller in magnitude than the total scattering power. With the $n = 3$ case, however, we obtain a very useful

result:

$$\begin{vmatrix} F_{000} & F_{-k} & F_{-h} \\ F_k & F_{000} & F_{k-h} \\ F_h & F_{h-k} & F_{000} \end{vmatrix} \geq 0, \tag{1.8}$$

which we will rewrite as

$$\left| F_h - \frac{F_k F_{h-k}}{F_{000}} \right| \leq \frac{\begin{vmatrix} F_{000} & F_{-k} \\ F_k & F_{000} \end{vmatrix}^{1/2} \begin{vmatrix} F_{000} & F_{-h+k} \\ F_{h-k} & F_{000} \end{vmatrix}^{1/2}}{F_{000}}. \tag{1.9}$$

In the case that all structure factors are especially large, the right side of equation 1.9 becomes small, leaving the relations for complex structure factors, and more specifically for the phases

$$F_h \sim F_k F_{h-k} / F_{000} \tag{1.10}$$

$$\phi_h \sim \phi_k + \phi_{h-k}. \tag{1.11}$$

Evidently, it is possible to find the most likely phase for a structure factor given the phases of two others, as long as the three reflections are all strong.

Attempts to determine phases from measured structure factors from the above relation, called the triplet relation, or from similar ones derived from higher order relations, run into an immediate problem, evident from a closer inspection of the mathematical form of the structure factor:

$$F_h = \sum_j f_j \mathrm{e}^{2\pi i \vec{k} \cdot \vec{r}_j}. \tag{1.12}$$

The problem is that the atomic scattering factors, f_j, are not constant. Instead, they depend on the momentum transfer, $Q \equiv \frac{4\pi \sin\theta}{\lambda}$. This makes it difficult to compare structure factors from different areas of the diffraction pattern, as the atomic scattering factors will be different. It is possible to remove this complication, however, by normalizing the structure factors to account for the changing atomic scattering factors. Qualitatively, this amounts to removing the spatial distribution of the atoms, making them point objects with a uniform scattering power. This is useful not only in that it makes structure factors comparable between different areas of the diffraction pattern, but also in serving to artificially sharpen the resultant structure map, making identification of atomic positions easier.

1.1.1 Normalized Structure Factors and Structure Factor Probability Distributions

If our structure contains an inversion center, then it is said to be centrosymmetric. This will immediately limit all structure factors to be real, and thus the phases will be limited to values of 0 or π only. We may therefore write the structure factor as

$$F_h = \sum_{j=1}^{N/2} 2f_j \cos 2\pi \vec{h} \cdot \vec{r_j} \tag{1.13}$$

where we sum over only the independent atoms, such that F_h may be considered the sum of half as many random variables as there are atoms in the unit cell, the random variables being defined as $x_j = 2f_j \cos 2\pi \vec{h} \cdot \vec{r_j}$. If we assume the distribution of atomic coordinates to be random [3], then all values of $\vec{r_j}$ are equally likely, and noting that $\langle \cos\theta \rangle = 0$ and $\langle \cos^2\theta \rangle = 1/2$, then we have

the mean value

$$\langle x_j \rangle = 2f_j \langle \cos 2\pi \vec{h} \cdot \vec{r_j} \rangle = 0 \tag{1.14}$$

and variance

$$\alpha_j^2 = \langle x_j^2 \rangle - \langle x_j \rangle^2 = 4f_j^2 \langle \cos^2 2\pi \vec{h} \cdot \vec{r_j} \rangle = 2f_j^2 \tag{1.15}$$

for our random variables. With the central limit theorem, we may note that we have the mean value and variance for F_h, given by

$$\langle F \rangle = \sum_{j=1}^{N/2} \langle x_j \rangle = 0 \tag{1.16}$$

and

$$\sigma^2 = \langle F^2 \rangle = \sum_{j=1}^{N/2} 2f_j^2 = \sum_{j=1}^{N} f_j^2 = \Sigma \tag{1.17}$$

respectively. This leads to the probability distribution of structure factors for centrosymmetric stuctures, given by

$$P_{\bar{1}}(F) = \frac{1}{\sqrt{2\pi\Sigma}} \exp\left(-F^2/2\Sigma\right). \tag{1.18}$$

In the case of non-centrosymmetric structures, the phases are no longer restricted, and it is convenient to write the structure factor as

$$F_h = A_h + iB_h. \tag{1.19}$$

In direct analogy to the derivation above, we obtain

$$P(A) = \frac{1}{\sqrt{\pi\Sigma}} \exp\left(-A^2/\Sigma\right), \qquad P(B) = \frac{1}{\sqrt{\pi\Sigma}} \exp\left(-B^2/\Sigma\right), \tag{1.20}$$

the probability distribution of the real and imaginary parts of the non-centrosymmetric structure factors. We have also now derived the expectation value for the structure factor under the assumption of point-like atoms randomly distributed throughout the unit cell. By normalizing our measured structure factors by the expectation value for randomly distributed point-like atoms, we obtain our normalized structure factors

$$|E_h| = \frac{|F_h|}{\sqrt{\langle |F^2| \rangle}} = \frac{|F_h|}{\sqrt{\epsilon\Sigma}} \tag{1.21}$$

where ϵ is 1 in general, but greater than one to allow for symmetry in certain reflection classes (these can be found in the International Tables for Crystallography [4]). The normalized structure factors can be considered as a measure of the information content of a particular reflection. The more the normalized structure factor deviates from 1, the more information it encodes about how nonrandom the structure is.

1.1.2 Probability Interpretation of Direct Methods

In common usage, the inequalities obtained from direct methods are interpreted as probability relations among phases. The probability associated with

a set of phases for a set of reflections is given by a von Mises distribution

$$P(\Phi_{hk}) = (1/L) \exp{(G_{hk} \cos \Phi_{hk})}, \tag{1.22}$$

where

$$G_{hk} = \begin{cases} (2/\sqrt{n})|E_h E_k E_{h-k}| & \text{for equal atoms} \\ 2\sigma_3 \sigma_2^{-3/2}|E_h E_k E_{h-k}| & \text{for non-equal atoms,} \end{cases} \tag{1.23}$$

with $\sigma_n = \sum_{j=1}^{N} Z_j^n$, Z_j being the atomic number of the jth atom, L being a normalization term dependent upon G_{hk}, and $\Phi_{hk} = \phi_h - \phi_k - \phi_{h-k}$.

If more than one set of phases, ϕ_{k_j}, ϕ_{h-k_j}, defining a single phase, ϕ_h, are known, then the total probability distribution of phase ϕ_h will just be given by the product of all of the, assumed independent, von Mises distributions. This gives rise to the tangent formula

$$\tan \beta_h = \frac{\sum_{j=1}^{r} G_j \sin \omega_j}{\sum_{j=1}^{r} G_j \cos \omega_j} \tag{1.24}$$

with $G_j = G_{hk_j}$ and $\omega_j = \phi_{k_j} + \phi_{h-k_j}$. The tangent formula gives the most probable value for $\phi_h = \beta_h$. The way in which direct methods are commonly implemented is to consider a suitable set of starting phases, and apply the tangent formula successively in an attempt to phase all of the remaining observed reflections. Such an approach relies on having well determined reflection intensities, which poses a difficult problem for powder diffraction due to peak overlap, which makes extracting individual intensities very difficult. Nevertheless, the approach has been successfully applied to many structures solved

from powder diffraction, and is the dominant means of structure solution in single crystal diffraction.

1.2 Simulated Annealing

The first crystal structures were solved through trial and error, in which a systematic search of all physically and chemically feasible structures was conducted. Such an approach requires a great deal of effort as well as physical and chemical intuition, and is only feasible for rather simple structures. However, the tradition of trial and error has seen a renaissance with the advent of the modern computer and various global optimization strategies. In this approach, trial crystal structures are created and evaluated for consistency with the data in an effort to find the best structure. The greatest benefit in this approach is the ability to incorporate chemical information into the model, greatly reducing the number of parameters to be determined. While chemical information can take many forms, one of the more common is that of molecular topology, which would allow one to model the structure as molecules instead of independent atoms, greatly reducing the size of the parameter space to be searched.

To demonstrate the benefit of a reduction in the number of parameters, it is useful to consider the odds of randomly finding the correct structure for a problem of a given size. Consider the simple case of free atoms defined by their fractional coordinates within a unit cell, such that each atom is located by three parameters. If we consider the structure solved when each parameter is within 10% of its correct value, then the odds of finding the correct structure

are 10^p where p is the number of parameters, and $p = 3n$ in the case of n free atoms. Evidently, the elimination of even a single parameter from our model simplifies the problem by an order of magnitude. Although this is a rather crude approximation of the odds, indeed a more thorough consideration is given by Shankland and David in which the probability scales as $(\frac{n}{200})^n$ [5], it serves as a convenient illustration of the benefit of simple models. While for simple structures such probabilities do not preclude a simple grid search in order to sample all of parameter space, structures of any complexity will preclude such a search in anything approaching reasonable times. Instead, global optimization algorithms are used which do not necessarily search all of parameter space, but instead can be considered to search the plausible regions with a predisposition for moving toward better ones.

Of the many global optimization algorithms which have been developed, by far the one most widely used in structure determination from powder diffraction is that of simulated annealing. The name derives from the analogous physical process in which solids are formed by cooling from a melt. At high temperature, the atoms will be in a disordered state and moving chaotically. As the system is cooled, provided it is done slowly, the system is annealed so that the chaotic motion is gradually reduced and the system is allowed to explore energy space and adopt the most energetically favorable configuration. If the system is cooled too rapidly, it will be quenched, freezing in the randomness and corresponding to a higher energy, metastable state.

To apply this concept to structure solution, we will consider χ^2 as the energy of our system, so that the lowest energy state will correspond to the structure which gives the best fit to our data. We begin with a random start-

ing structure, and perform a random perturbation to this structure. If the perturbed structure gives a better fit (lower χ^2) than the starting structure, then we accept the change unconditionally. If the perturbed structure gives a worse fit, then it is accepted with a probability given by

$$P = \exp\left(\chi^2_{\text{old}} - \chi^2_{\text{new}}\right)/T. \tag{1.25}$$

This is the Metropolis condition [6] and ensures that the system is able to climb out of metastable minima while still at finite temperature. This process is iterated allowing an exploration of parameter space while the system is slowly cooled.

The main benefits to this approach are the ability to move away from metastable minima, thanks to the acceptance of less favorable solutions with finite probability and the ease with which the algorithm can be implemented and used. The algorithm relies on only a single parameter, which is the cooling schedule. One must be careful to cool the system slowly enough that it finds the global minima, but still fast enough to solve the problem in a reasonable time. It is common to repeat a simulated annealing process multiple times, or to run several in parallel, to ensure that the true minima has been found, and not merely a local one.

Unfortunately, there is no way of determining the ideal cooling schedule for a given problem, and this algorithm is poorly suited to parallelization. However, with a simple modification, both of these issues are readily overcome. The modification, termed parallel tempering, requires that a number of simulated annealing tracks be run in parallel, but with different and constant

temperatures [7]. This removes the issue of a cooling schedule. Instead, every now and then, the tracks will exchange temperatures so that the one with the best solution receives the lowest temperature through to the worst solution and the highest temperature. This ensures that the lowest minima are carefully explored while the shallower ones are strongly perturbed in an attempt to kick them into different, hopefully deeper, minima. Such an approach lacks a natural stopping point, but is perfectly suited to parallelization, taking advantage of the advances in computer processor architecture, and may simply be left to run for as long as one can afford.

1.3 Charge Flipping

Charge flipping is, in the words of its creators, "a deceptively simple structure-determination algorithm that solves the phase problem with much weaker assumptions than classical direct methods." [8]. The assumptions are the very simple ones that the correct structure factors should have moduli in agreement with those measured, and that the real space structure, meaning the electron density of the crystal structure, should be predominately positive. By iterating between real and reciprocal space, and imposing these constraints at each point, the algorithm is able to phase a diffraction pattern.

The implementation of the algorithm is straightforward. First, the structure factor moduli are determined from the measured intensities and combined with a random set of starting phases which satisfy Friedel's law ($\phi(-h) = -\phi(h)$. This is Fourier transformed into a real space charge density, ρ, to give the real space starting point. This charge density is modified according to

the constraint that it should be positive by the charge flipping step, FLIP, of multiplying any density below $-\delta$ by -1. This will weakly impose positivity as it only allows small negative features, which are unavoidable given finite resolution of the data, due to truncation effects of the Fourier transform. This modified charge density, g, is Fourier transformed to give a set of structure factors, G. Unless we have found the correct structure, this set of structure factors will not correspond to the measured ones. So we modify them by keeping the phases but imposing the measured moduli, DATA. These new structure factors, F, are then Fourier transformed to obtain a new charge density, ρ, and the process can be repeated as desired.

$$\begin{array}{ccc} \rho & \xrightarrow{\text{FLIP}} & g \\ \text{FFT}^{-1} \uparrow & & \downarrow \text{FFT} \\ F & \xleftarrow{\text{DATA}} & G \end{array} \tag{1.26}$$

Charge flipping is as close to a truly *ab initio* method of structure solution as possible. We make only the assumption that the electron density is positive (this may be relaxed even further, which makes the algorithm suitable for neutron diffraction [9]), but make no assumption of atomicity, and because we deal with measured structure factors and not normalized ones, there is no need to specify the contents of the unit cell. The implementation is commonly performed in space group $P1$, so that the symmetry is derived from the structure and does not need to be determined *a priori*. Although the method is purported to require data which extends out to a d spacing of ~ 1 Å, making its use in powder diffraction inherently difficult, it appears to work remark-

ably well and has met with a great deal of success despite its relative newness. Charge flipping was applied to the solution of $Zn(SC_6H_4S)(dien)_{1.2}$ in chapter 6 of this thesis.

1.4 Rietveld Refinement

Refinement of a structure is generally the last step of the structure solution process in crystallography. When dealing with powder diffraction data, this inevitably means Rietveld refinement. First hinted at in Rietveld's work on neutron powder diffraction in 1967 [10], and fully developed by him in 1969 [11], the method deviates from the then standard practice of fitting a pattern based simply on integrated intensities (Eq. 1.27) and attempts, instead, to fit the entire pattern point for point (Eq. 1.28).

$$\chi^2 = \sum_j w_j (I_j^{\text{obs}} - I_j^{\text{calc}}) \tag{1.27}$$

$$\chi^2 = \sum_j w_j (y_j^{\text{obs}} - y_j^{\text{calc}}) \tag{1.28}$$

with

$$y_j^{\text{calc}} = s \sum_k m_k L_k |F_k|^2 G(\Delta\theta_{jk}) + y_i^{\text{back}} \tag{1.29}$$

where s is a scale factor, L_k the Lorentz-polarization factor for reflection k, F_k the structure factor, m_k the multiplicity factor, $\Delta\theta_{jk} = 2\theta_i - 2\theta_k$ where $2\theta_k$ is the calculated position of reflection k, $G(\Delta\theta_{jk})$ is the shape function of the reflection, and y_j^{back} is the background contribution. In this way, each measured data point is considered to be an independent measurement in the

refinement process. This is especially important for powder diffraction in which integrated intensities of overlapped reflections cannot be determined, but their contribution to a given data point may be.

1.5 Maximum Entropy

In a Rietveld refinement, the end result is a list of atoms and their coordinates within a unit cell. However, one may be concerned with information which cannot be encoded in such a list of atomic coordinates. In such cases, one would like to consider the continuous charge distribution $\rho(\vec{r})$ as it is averaged over unit cells. This may be obtained through Fourier maps, but these are subject to large truncation errors due to the finite experimental resolution. In the case that the features of interest are small, such errors may be overwhelming, making further analysis useless. A superior approach is the use of maximum entropy maps to reconstruct the underlying charge distribution.

Maximum entropy is a principle based on Bayesian statistics which produces the most non-committal answer to an underdetermined problem. In terms of crystallography, what we are concerned with is the probability of finding an electron at a given point in the unit cell, a probability which will directly correspond to the overall charge density. We may imagine the ubiquitous roomful of monkeys scattering units of charge into unit cells broken up into discrete bins. After the monkeys have scattered all of their charges, we will count the charge in each bin, denoting the amount in the first bin by n_1, the amount in the second bin by n_2, and so on, with the total number of

"charge" defined by

$$N = \sum_{i=1}^{M} n_i, \tag{1.30}$$

with M being the total number of bins. If we allow the monkeys to repeat this exercise many times, we will find that some distributions occur more often than others. The frequency of a given distribution, denoted as $\{n_i\}$, is just

$$F(\{n_i\}) = \frac{\text{Number of ways of obtaining } \{n_i\}}{M^N}. \tag{1.31}$$

This numerator is easily evaluated by considering the number of ways to choose n_1 amounts of charge from a total N, the number of ways to choose n_2 amounts of charge from the remaining $N - n_1$ and so on, giving

$$F(\{n_i\}) = \frac{\frac{N}{n_1! n_2! \ldots n_M!}}{M^N} \times q_1^{n_1} q_2^{n_2} \ldots q_M^{n_M}, \tag{1.32}$$

where $q_i^{n_i}$ is the prior probability of bin i to contain n_i units of charge. By taking the logarithm and using the Stirling approximation, this can be simplified to

$$\log[F] = \sum_{i=1}^{M} n_i \log[q_i] - \sum_{i=1}^{M} n_i \log[n_i]. \tag{1.33}$$

This looks very much like an entropy, and indeed, we will rewrite it in terms of a charge density, such that $\rho_i = n_i/N$, and define it as such

$$S = -\sum_{i=1}^{M} \rho_i \log[\rho_i/q_i]. \tag{1.34}$$

The density which corresponds to the highest entropy will be that which can be obtained in the highest number of ways, making it the most likely final

state. In the case that all prior probabilities for each bin are equal, and we have no further information, this will result in a maximum entropy answer with an even distribution of charge. However, if we impose the constraints of our measured data, then we limit the set of permissible answers to those which agree with the data. In this case, the maximum entropy answer will be the charge distribution that can be produced in the greatest number of ways, out of those which agree with the constraints of the data. In this way, maximum entropy can be used to produce the most likely charge map of the unit cell which is in agreement with the experimentally measured diffraction data.

The technique of maximum entropy is commonly used to image disordered features in the crystal structure, such as disordered solvents [12] or metal atoms within fullerene structures [13], which cannot be well modeled by nicely positioned atoms. It has also been used in attempts to image the charge associated with bonding [14, 15], which again is much more diffuse than that obtained from single atoms.

While there are a number of other techniques used to extract structural information from diffraction data, those summarized above are the ones which have been used in the work presented in this dissertation, and so we will limit our discussion to these. For a broader discussion of the techniques used in crystallography, the reader is referred to works such as Giacovazzo [16], or, for more specific application to powder diffraction [5] and [17].

Part I

Simulated Annealing and Rietveld Refinement, Standard Examples

Chapter 2

Polymorphism

Polymorphism refers to the tendency of some compounds to exhibit more than one crystal structure. While this phenomenon is widespread throughout all facets of chemistry, first being recognized in ammonium and potassium salts, the recent awareness and importance is nowhere more evident than in the field of pharmaceutical materials. Although they are composed of the same molecules, polymorphs have different structures, making each a unique material with its own chemical and physical properties. For pharmaceuticals, this means that the polymorphic form will determine the solid state properties of a drug, such as stability, solubility, and even ease of processing, all of which are incredibly important to the overall efficacy and marketability of a drug. Compounding the practical interest in pharmaceutical polymorphism is the fact that many drug patents are dependent upon crystal structure, making the motivation to understand the phenomena economic as well as scientific. For further information, we will refer the reader to the review by Bernstein [18].

2.1 2-chloro-4-nitrobenzoic Acid

In 1952 Ebert and Gottlieb showed that infrared spectrometry could be a useful tool for the study of polymorphism in organic compounds [19]. One of the examples of its use was 2-chloro-4-nitrobenzoic acid (2c4n) (Fig. 2.1) which is known today as a novel potential therapy for immunodeficiency diseases, including HIV infection [20, 21]. This substance was obtained by them in two polymorphic forms: modification I was crystallized from benzene while modification II was produced via slow cooling from the melt. The two forms exhibited appreciable differences in their infrared spectra.

Figure 2.1: The 2c4n molecule.

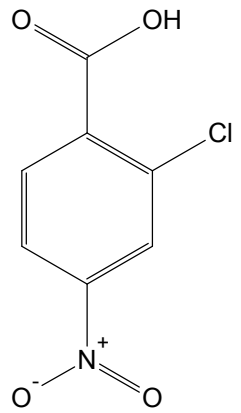

Subsequently the system was studied by Kuhnert-Brandstätter and Riedmann who used hot-stage microscopy, DSC and solid FT-IR to identify and characterize two polymorphic forms [22]. The compound crystallized concomitantly as a mixture of crystals of two polymorphs, modifications I and

II. Modification II transformed to modification I between 60°C and 90°C. No structure determinations were carried out.

In a reinvestigation of this system, our collaborators Joel Bernstein and Inna Barzky prepared and determined the structures of the two polymorphic forms through single crystal diffraction [23] (Fig.2.2). However, their preliminary results suggested the possibility of a third polymorphic form resulting from the heating of modification II and existing only at elevated temperatures from $\sim 65 - 85$°C.

2.1.1 Crystal Preparation

Barzky and Bernstein obtained a powder of 2-chloro-4-nitrobenzoic acid of pale yellow color from Aldrich (lot number: S14087-034), and characterized it by FT-IR spectroscopy as modification I (Fig. 2.4(a)) [19, 22]. The substance was recrystallized from a variety of solvents at room temperature. All crystallization conditions except water as a solvent resulted in the formation of modification II (Fig. 2.4(b)). Aqueous solutions resulted in the crystallization of a mixture of the two polymorphic forms [24]. Fig. 2.4(c) shows thin needles of modification II and smaller crystals which belong to modification I organized in a cluster.

For additional crystallizations the material was purchased again from Aldrich but this time with a different lot number (S42781-337). At first sight the commercial compound appeared the same pale yellow powder; however when examined by PXRD it turned out to be a mixture of the two modifications, in which modification II is the dominant one. Experimental diffrac-

Figure 2.2: The crystal structures of 2-chloro-4-nitrobenzoic acid, modification I (a) and modification II (b)

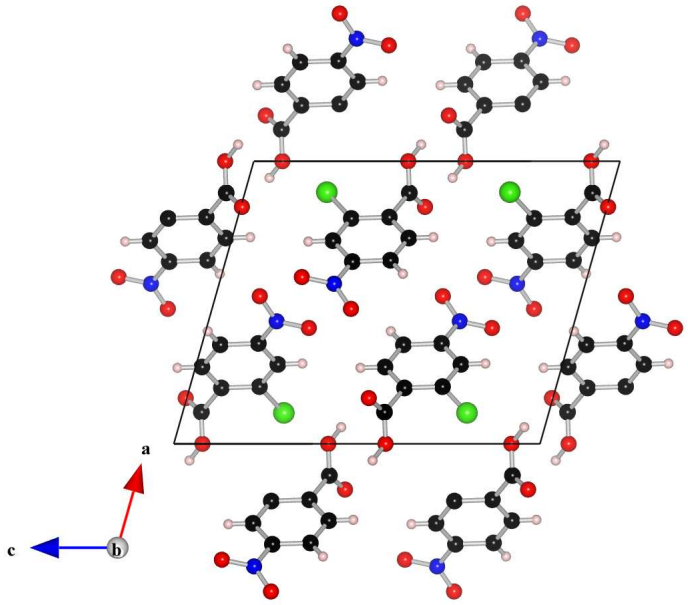

(a)

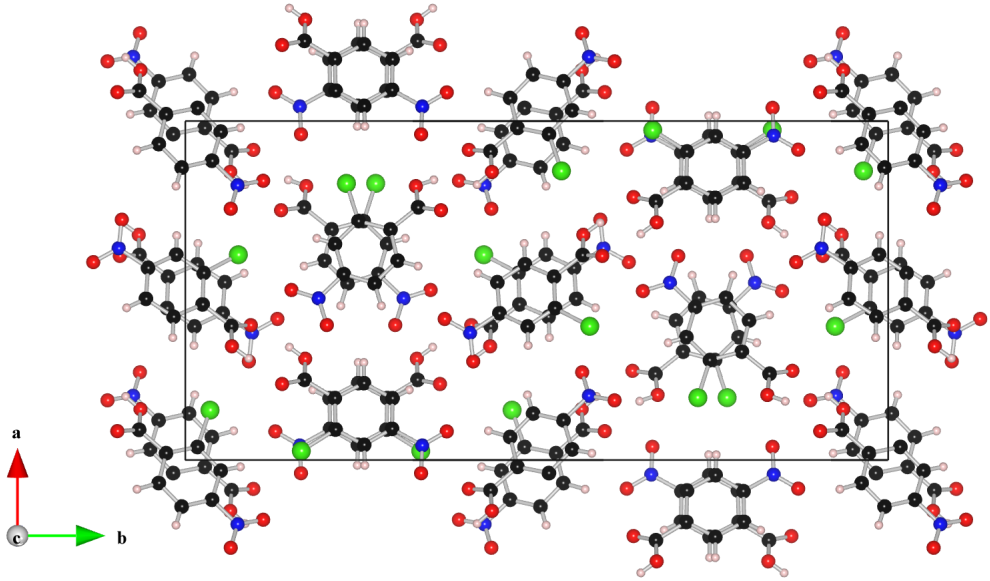

(b)

tograms of the two commercial powders and calculated patterns from single crystal structures are shown in Fig. 2.3. All sample preparation was done by Inna Barzky at Ben-Gurion University of the Negev.

Figure 2.3: Experimental diffractograms of Aldrich-1 (S14087-034) and Aldrich-2 (S42781-337) and the calculated powder diffraction patterns of modifications I and II. Data collected with Cu-Kα radiation on the laboratory source. Figure taken from [23].

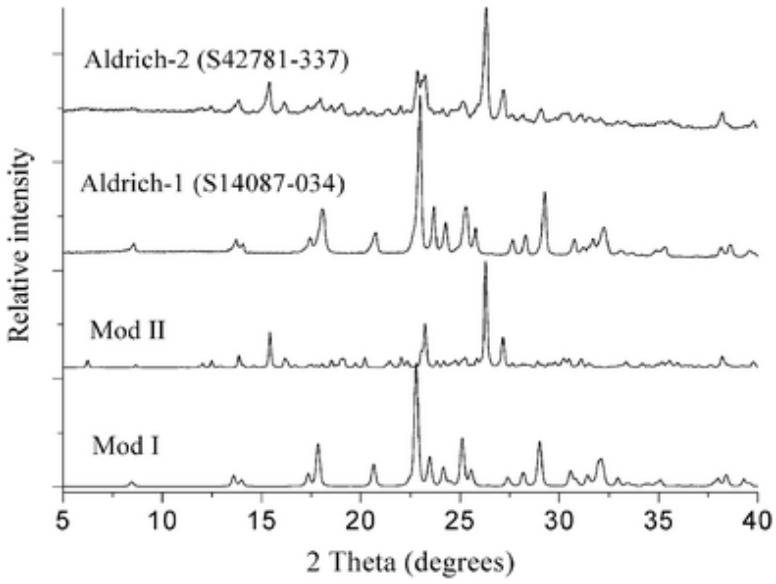

2.1.2 X-ray Powder Diffraction Experiments

The X-ray powder diffraction of modification II was examined on a laboratory diffractometer at Beer Sheva as a function of temperature in a sealed capillary (Fig. 2.5). The diffraction was measured every $10 - 15$°C in the temperature range $25 - 60$°C, with no evidence for transformation to modification I. At

Figure 2.4: Photographs of 2-chloro-4-nitrobenzoic acid polymorphs: (a) modification I, (b) modification II and (c) modifications I and II crystallized concomitantly. Figure taken from [23]

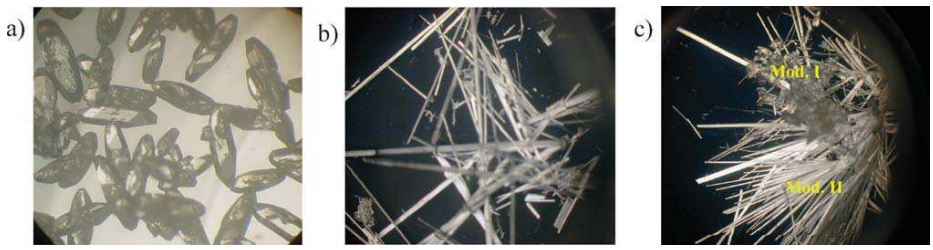

75°C it was possible to recognize the initiation of a phase transition. At 90°C the transformation from modification II is completed; however the diffraction pattern shows significant differences from the room-temperature pattern of modification I. Subsequent cooling of the sample to room temperature gives the powder pattern of modification I consistent with that calculated from the single-crystal structure.

Due to the dramatic motion of the peaks through the range 70°C to 100°C, the thermal behavior of the powder diffraction pattern of the two modifications was examined with high-resolution synchrotron X-ray powder diffraction to determine if there is an additional phase between modification I and II. A powder sample of modification II was sealed inside a thin-walled glass capillary of 1.5 mm nominal diameter. X-rays of wavelength 0.6986 Å were selected with a Si(111) channel cut monochromator. After the sample, the diffracted beam was analyzed with a Ge(111) crystal and detected by a NaI scintillation counter. Wavelength and diffractometer zero were calibrated using a sample of NIST Standard Reference Material 1976 (a sintered plate of Al_2O_3). The sample was loaded in a locally made heating stage and the temperature monitored

by a thermocouple placed near the sample. We observed a significant temperature difference between sample and thermocouple, and therefore the melting point of a sample of ibuprofen was used to calibrate the temperature over the same range. The correction applied was $T_{\text{sample}} = 22 + 0.893(T_{\text{thermocouple}} - 22)$; all values are in degrees Celsius. All fits to the data were performed using the program *TOPAS-Academic* [25].

Diffraction data over the angular range of $6 - 7.5°$ 2θ were taken at several temperatures as shown in Fig. 2.6; peaks at 6.95, 7.30 and 7.35° 2θ indicate that the sample is pure modification II. Significant changes in the diffraction pattern were first noted when the sample reached 83°C, and so the temperature was held at that value. After the transformation was complete, a full dataset covering the range of $1 - 30°$ 2θ was taken. Rietveld refinement of the structure of modification I to the data taken at 83°C was found to give a satisfactory fit, as shown in Fig. 2.7. The sample was subsequently cooled back to room temperature, and a dataset covering the range of $6 - 12°$ 2θ was taken. These room temperature data were also found to be consistent with the structure of modification I.

The sample, having been transformed from modification II to modification I by heating, was again studied with in situ measurements performed during the heating process. Powder diffraction patterns were collected over 2θ values of $2 - 12°$ during two heating cycles at temperatures from 25°C to 154°C, as shown in Figure 2.8. The lattice parameters at each temperature were determined with a Pawley fit using the lattice of modification I, and are shown in Figure 2.9. Between room temperature and the melting point, the *b*-axis grows and the perpendicular *a*-axis shrinks significantly, but the volume changes by

a much smaller fraction. Full high-resolution powder diffraction patterns (extending from $1 - 30^\circ$ 2θ) of modification I were measured at temperatures of 25°C, 83°C, 88°C, 104°C and 129°C; all refinements are consistent with the structure of modification I (Fig. 2.10, Table 2.1). Having melted the sample, the heater was turned off and the sample quenched to room temperature over an interval of approximately 30 seconds. Subsequent measurement of the cooled sample showed that it consisted of modification II, although the granularity of the diffraction pattern made a refinement impossible.

Table 2.1: Experiment and refinement details for 2-chloro-4-nitrobenzoic acid

Temperature	22°C	83°C	88°C	104°C	129°C
space group	$P2_1/c$	$P2_1/c$	$P2_1/c$	$P2_1/c$	$P2_1/c$
a(Å)	10.7930(2)	10.5323(3)	10.5449(3)	10.3670(3)	10.2990(2)
b(Å)	5.8474(2)	6.0752(3)	6.0721(2)	6.2073(3)	6.2928(1)
c(Å)	13.4587(2)	13.5080(3)	13.5142(3)	13.5437(3)	13.6124(2)
β(°)	105.803(1)	107.565(2)	107.495(2)	109.058(4)	110.010(1)
volume(Å^3)	817.28(3)	824.02(5)	825.29(4)	823.78(5)	828.96(3)
Z	4	4	4	4	4
ρ (Mg/m^3)	1.6382(1)	1.6248(1)	1.6223(1)	1.6252(1)	1.6151(1)
R_{wp}(%)	8.840	11.760	10.606	10.587	10.568
χ^2	12.631	7.295	3.940	2.053	20.986
Parameters	38	41	41	42	41
λ (Å)	0.69865	0.69865	0.69865	0.69865	0.69865

Figure 2.5: Variable-temperature laboratory XRPD. Only modification II is present between 32°C and 60°C. The transition to modification I begins at $\sim$ 80°C and is completed at $\sim$ 90°C. The uppermost and lowermost diffractograms belong to the powder diffractions of the two modifications calculated from the single-crystal structure determinations. The confusion about a possible third form is due to the disimilarity between the diffractograms at 100°C and modification I at RT, which are actually the same structure. Figure taken from [23].

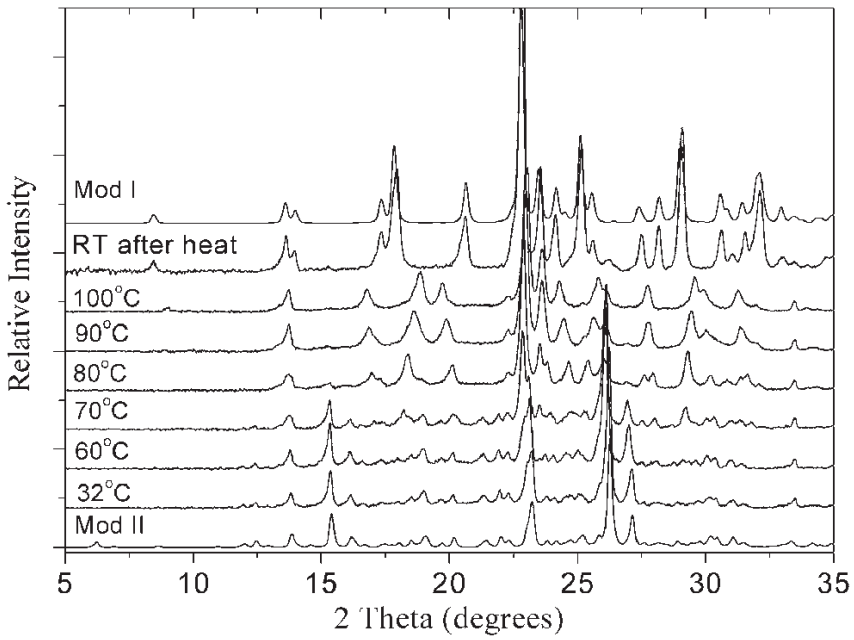

Figure 2.6: Synchrotron powder diffraction patterns taken during the heating of modification II. The transformation at 83°C can be seen in the three patterns at that temperature which are roughly 4 min apart in time. The top pattern was taken at room temperature after the transformation was complete. Figure recreated from [23].

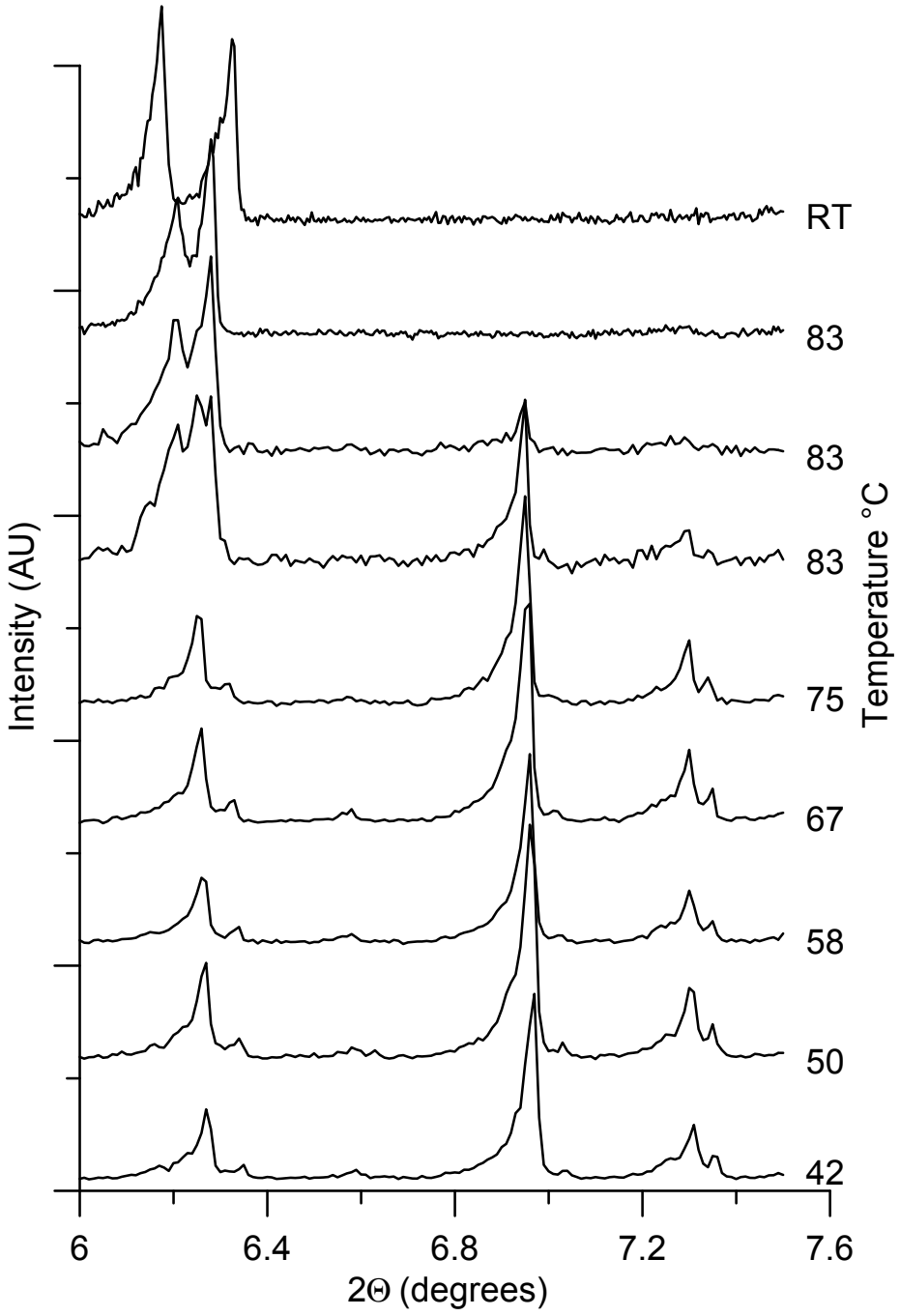

Figure 2.7: Rietveld fit of the structure of modification I to the synchrotron PXRD data taken at 83°C, immediately after transformation from modification II. Blue circles are the data, the solid red line is the calculated pattern. The curve below shows the difference between the two and the tick marks indicate allowed peak positions. Figure recreated from [23].

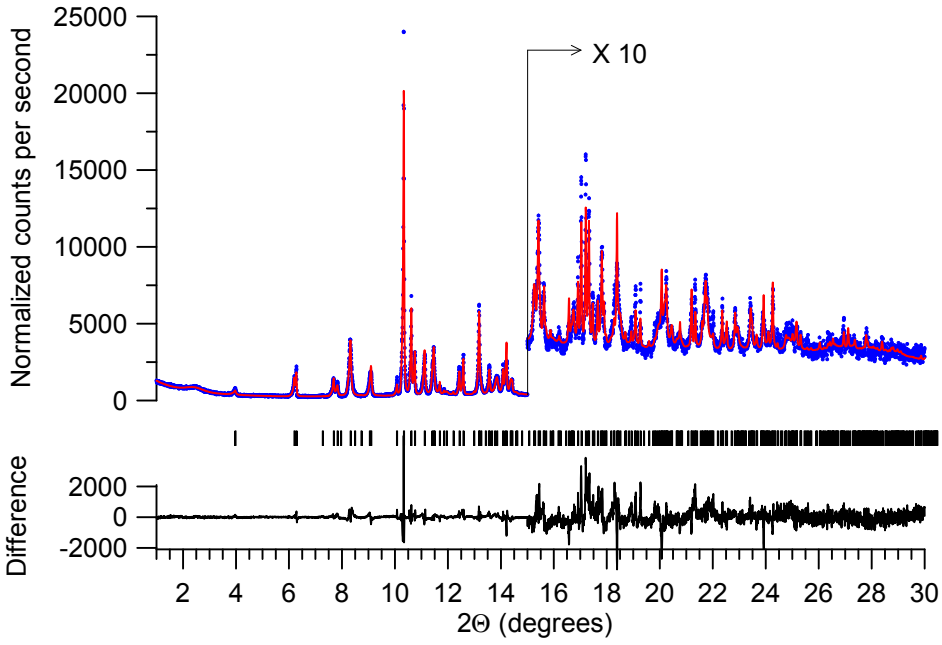

Figure 2.8: Synchrotron powder diffraction patterns taken during the heating of modification I. The continuous evolution of the lattice parameters can be seen, although no changes suggestive of a phase transformation are observed. The sample quality can be seen to deteriorate as the melting temperature is approached. The sample has melted at 154°C, and recrystallizes as modification II after being quenched from the melt. Figure recreated from [23].

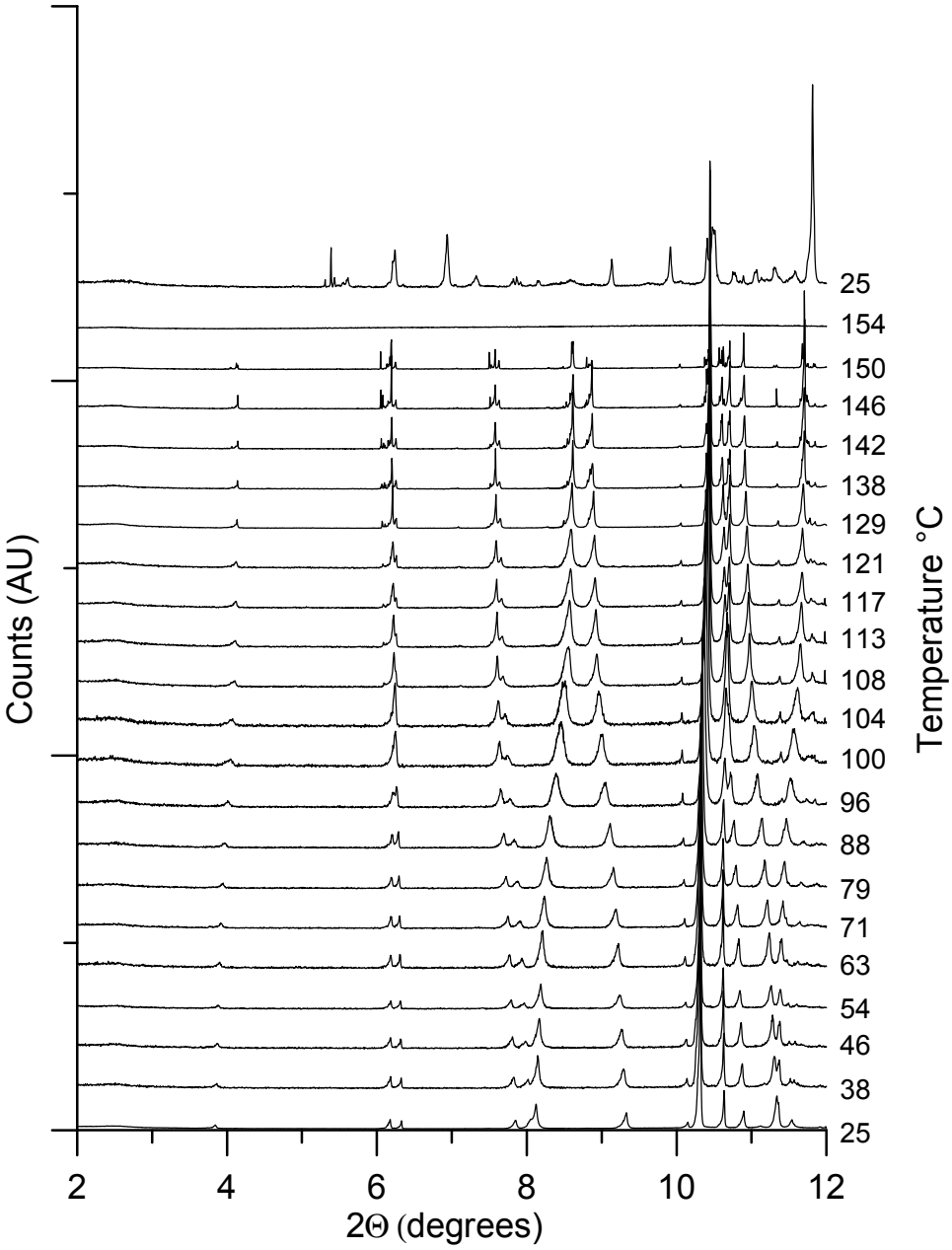

Figure 2.9: Lattice parameters and cell volume of modification I normalized to the values at room temperature. Note the change in slope in the vicinity of 90°C. Figure recreated from [23].

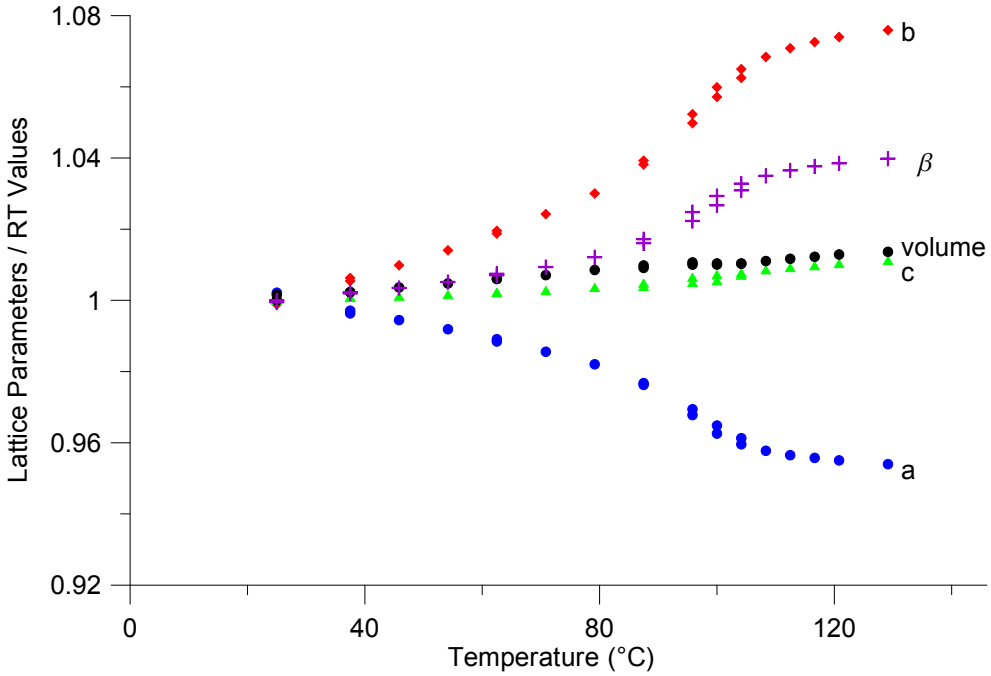

Figure 2.10: Overlay of the structure of modification I at room temperature (black) and at 129°C (green).

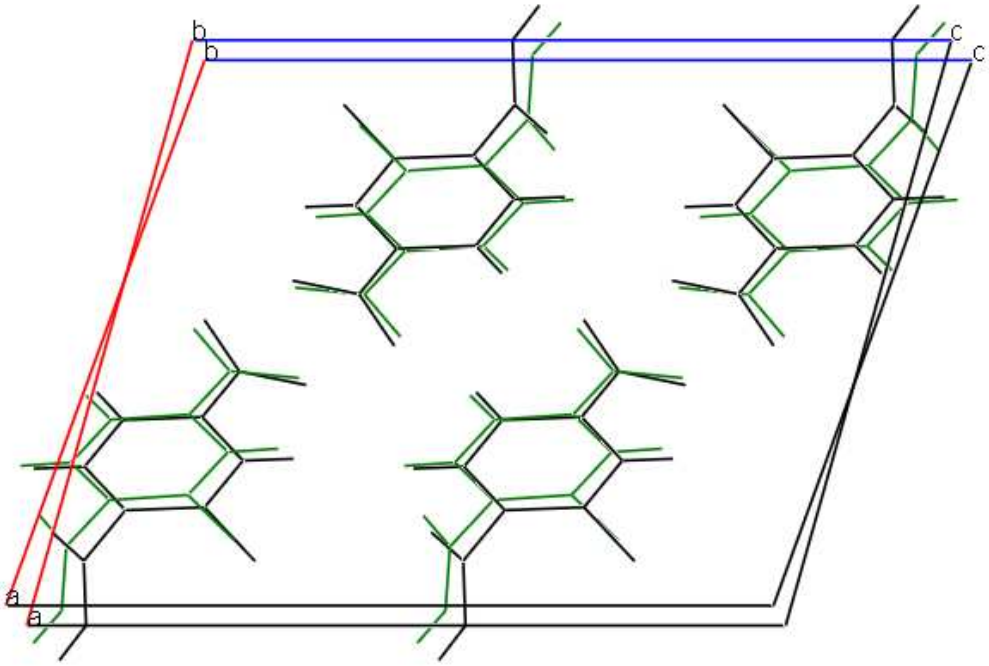

2.2 p'-Methylchalcone

p'-Methylchalcone (p-MC) (Fig. 2.11) has been reported to be an extremely polymorphic compound. First studied by Weygand, this molecule was found to exist in 13 distinct polymorphic forms, determined mainly from thermomicroscopy [26, 27, 28, 29]. Melting points were determined for seven of the crystalline forms, modification I: 74.5°C, II: 56.5°C, III: 55.5°C, IV: 54.5°C, V: 48°C, VI: 46.5°C, and VII: 44.5°C. Recently, Toda *et al.* determined the crystal structure of the stable modification I [30]. Barzky *et al.* were able to obtain crystal structures of metastable modifications II, III, and IV as well as determining the conditions under which these metastable modifications may be formed [31].

Figure 2.11: The p'-methylchalcone molecule.

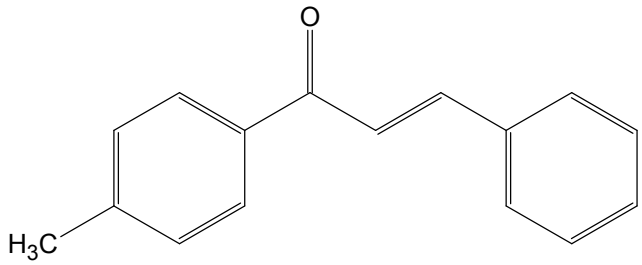

2.2.1 Crystal Preparation

All sample preparation and single crystal measurements were performed by Bernstein and Barzky at Ben-Gurion University of the Negev. p'-

Methylchalcone was synthesized by condensation of 4′-methylacetophenone 96% (Fluka) and benzaldehyde 99% (Aldrich) in alcoholic sodium hydroxide. Crystallization occurred upon completion of condensation, resulting in a yield of the highest melting modification I. Subsequent attempts to obtain crystals of any of the thermodynamically unstable forms from solution by recrystallization experiments from the stable form proved essentially impossible, since the preferred nucleation of the stable form prevents the nucleation of any other. It was concluded that further attempts at preparation of the thermodynamically unstable forms would need to be carried out in virgin glassware and under seed-free conditions (*i. e.* in a laboratory in which that stable form had not been present). Attempts to carry out the reaction and crystallization at three different temperatures (20°C, 4°C, and -13°C) in three different solvents (methanol, ethanol, and 2-propanol) resulted in single crystals of three thermodynamically unstable forms (II, III, and IV) as well as the stable (I) modification. Crystal structures of modifications III, and IV were obtained using single crystal methods, and that of modification I was confirmed. While single crystals did form of modification II, they were of insufficient quality to allow for structure solution.

2.2.2 Structure Determination of Modification II

High resolution X-ray powder data were collected on beamline X16C of the National Synchrotron Light Source at Brookhaven National Laboratory. X-rays of wavelength 0.697884 Å were selected with a Si(111) monochromator and analyzed using a Ge(111) crystal. The sample was measured in capillary

geometry over a range of $1 - 28.98°$ 2θ.

The diffraction data was indexed using *TOPAS-Academic* as space group $P2_1/c$ with lattice parameters $a = 11.287(2)$ Å, $b = 11.010(1)$ Å, $c = 11.199(1)$ Å, and $\beta = 116.57(8)°$. The volume of the unit cell suggests 4 molecules, and the lack of symmetry of the molecule indicates that only a single independent molecule would be present on a general position. The structure was solved through simulated annealing and Rietveld refined using *TOPAS-Academic* (Figs. 2.12 and 2.13). It was found necessary to include a preferred orientation correction, along the (111) direction [32], as well as to model the strain broadening anisotropically [33] in order to achieve a suitable final refinement. However, neither correction is inconceiveable given the needle like habit of the crystals which compose the sample.

Figure 2.12: Refined structure of modification II of p'-MC. Carbon atoms are shown in black with oxygen atoms in red. Hydrogens have been omitted for clarity.

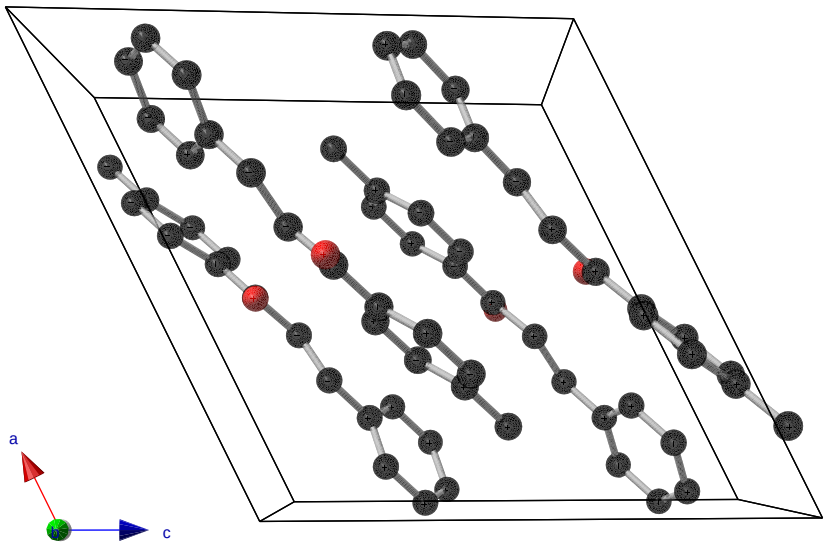

Figure 2.13: Rietveld refinement of p'-MC. Blue dots are the measured data, the red line is the calculated fit from the refined structure, and the black line below is the difference between the two. Allowed peak positions are indicated by the tick marks.

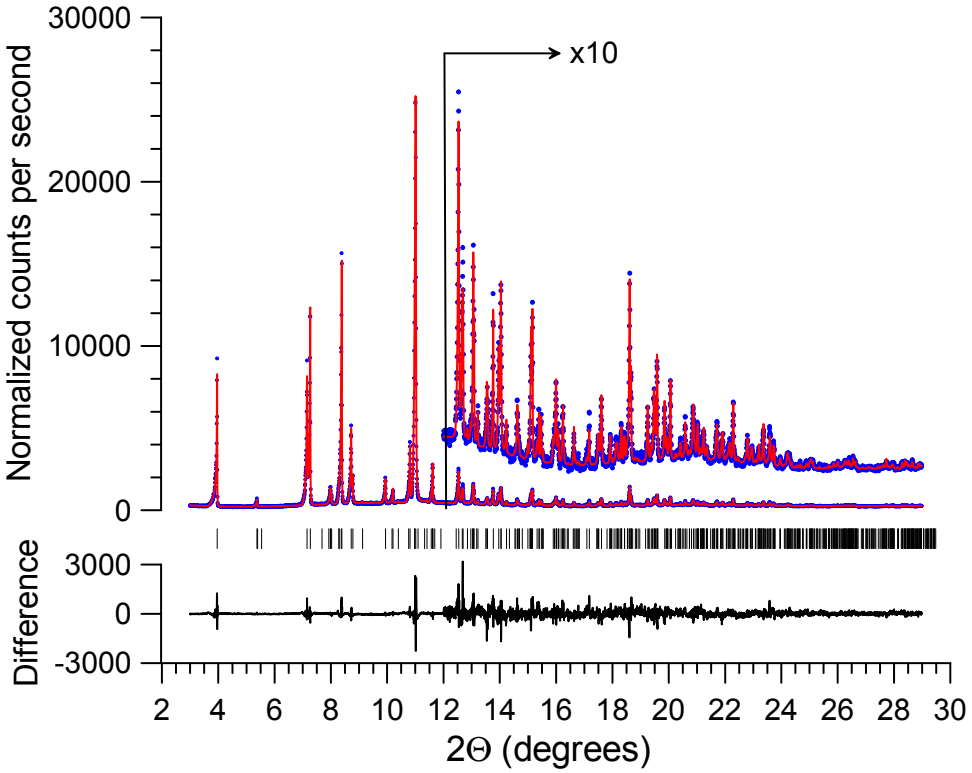

Chapter 3

Organo-metallics

Historically, materials have been divided into two classifications, organic and inorganic. Recently, however, the many benefits to hybrid materials have been recognized, and a large field of study has grown up around materials composed of traditionally organic molecules in combination with inorganic elements, generally metallic in nature. The main benefits to such a hybrid approach is the potential to combine the otherwise exclusive properties of the two classifications. For example, combining the technologically desirable properties of metals, *e. g.*, conductivity or magnetism, with those of organic materials, *e. g.*, flexibility and ease of synthesis. Further, by using organic molecules to mediate the interaction of inorganic elements, it may be possible to target a desired set of properties or to develop materials with previously unknown behavior.

In the search for new semiconducting materials, molecule-based extended solids are an intriguing class of compounds, which, with properly chosen components, could be expected to be semiconducting. The molecular components

would allow for fine tuning of physical properties, as is typical in organic molecular and polymeric semiconductors, while the extended network of covalent bonds throughout the structure could be expected to result in higher electron and hole mobilities as in traditional semiconductors, $\sim 10^3$ times higher than that found in purely organic examples. A logical starting place for such materials are analogues to known inorganic semiconductors. For example, if 1,4-benzenedithiol is considered the analogue of H_2S, and -SC_6H_4S- the analogue of S^{2-}, then the material [$Pb(SC_6H_4S)$] would be analogous to PbS, a small bandgap semiconductor (E_g = 0.37 eV) [34]. Previous studies of the reaction products of various metal salts with 1,4-benzenedithiol or 1,2,4,5-benzenetetrathiol were found to be semiconducting, but the resulting materials were generally not crystalline, and so no structural information was available [35, 36].

Our collaborators have recently found that the reaction of metal acetates with arenepolythiols in ethylenediamine (en) at elevated temperatures often leads to crystalline materials with extended two- or three-dimensional bonding. This has led to the study, and targeted synthesis, of some analogues to traditional metal chalcogenide semiconductors. While detailed here for completeness, all synthesis, conductivity and absorption measurements were performed by Dayna Turner and Thomas Vaid at the University of Washington, St. Louis [37, 38].

3.1 Group II-VI Analogues

3.1.1 $[M(en)_3][M(EC_6H_4E)_2]$ Crystal Preparation

All network-forming reactions were carried out under N_2 in degassed ethylenediamine or degassed acetonitrile; the products are air-stable and the workup and subsequent handling was done without protection from air.

The reaction of $Cd(OAc)_2$ and one equivalent of 1,4-benzenedithiol in ethylenediamine at reflux for 16 h yielded a white, microcrystalline powder with the formula $[Cd(en)_3][Cd(SC_6H_4S)_2]$. In a similar preparation, the reaction of $Zn(OAc)_2$ and one equivalent of 1,4-benzenedithiol in en at reflux for 16 h gave a white, microcrystalline powder with the formula $[Zn(en)_3][Zn(SC_6H_4S)_2]$. A third compound, pale yellow $[Cd(en)_3][Cd(SeC_6H_4Se)_2]$, was synthesized by the reaction of $Cd(OAc)_2$ and one equivalent of 1,4-$AcSeC_6H_4SeAc_5$ (a protected form of 1,4-benzenediselenol) in en at reflux for 16 h.

It was expected that a reaction like the ones above that incorporated a second metal-containing reagent in which the metal, M, is a hard Lewis acid would result in a product with the $[Cd(en)_3]^{2+}$ cation replaced by $[M(en)_3]^{2+}$, while the anionic $[Cd(SC_6H_4S)_2]_2$ framework would be maintained. $[Mg(en)_3][Cd(SC_6H_4S)_2]$ was targeted through the reaction of one equivalent of $Cd(OAc)_2$, one equivalent of $Mg(OTf)_2$ (OTf = triflate), and two equivalents of 1,4-benzenedithiol in en at reflux, yielding a white reaction product later determined through structure refinement to be $[Mg_{0.82}Cd_{0.18}(en)_3][Cd_{0.98}Mg_{0.02}(SC_6H_4S)_2]$.

3.1.2 $[M(en)_3][M(EC_6H_4E)_2]$ Crystal Structure Solution

All powder diffraction patterns were collected at beamline X16C at the National Synchrotron Light Source at Brookhaven National Laboratory. All indexing, structure solution, and refinement was performed using *TOPAS-Academic*.

$[Cd(en)_3][Cd(SC_6H_4S)_2]$

Powder diffraction data was collected from a sample loaded into a flat plate with a wavelength of 0.69675(3) Å. The pattern was indexed as space group $C2/c$, with lattice parameters of $a = 12.0139$ Å $b = 14.8308$ Å $c = 14.5741$ Å $\beta = 90.217°$. Elemental analysis suggested the presence of 1.5 molecules of ethylenediamine per polymer unit ($Cd[SC_6H_4S]$). The structure was solved using simulated annealing, modeled as free Cd atoms, and Z-matrices for the S-Ph-S units and ethylenediamine molecules. It was determined that there are two independent Cd atoms, both lying on the 2-fold axis, as well as two independent S-Ph-S units, both lying on inversion centers. One ethylenediamine molecule is in a general position, while another is centered on the 2-fold axis.

The resulting structure consists of $[Cd(en)_3]^{2+}$ cations within a two-dimensional anionic square grid of formula $[Cd(SC_6H_4S)_2]_2$. A fragment of one two-dimensional layer is shown in Figure 3.1; other layers are stacked such that the $[Cd(en)_3]^{2+}$ cations reside above and below the Cd atoms of the anionic network of adjacent layers. Each $[Cd(en)_3]^{2+}$ (Fig. 3.2) cation is chiral, and $[Cd(en)_3][Cd(SC_6H_4S)_2]$ contains a 1 : 1 ratio of the enantiomers; the two enantiomers alternate in a checkerboard pattern within each layer. The sample

geometries above and below 22° 2θ were different, and so those regions were treated as two separate datasets in the Rietveld refinement (Fig. 3.3).

Figure 3.1: Structure of one layer of $[Cd(en)_3][Cd(SC_6H_4S)_2]$. Cd atoms are purple, S atoms yellow; N atoms blue, and C atoms black. The view is along the *b*-axis with the unit cell outlined.

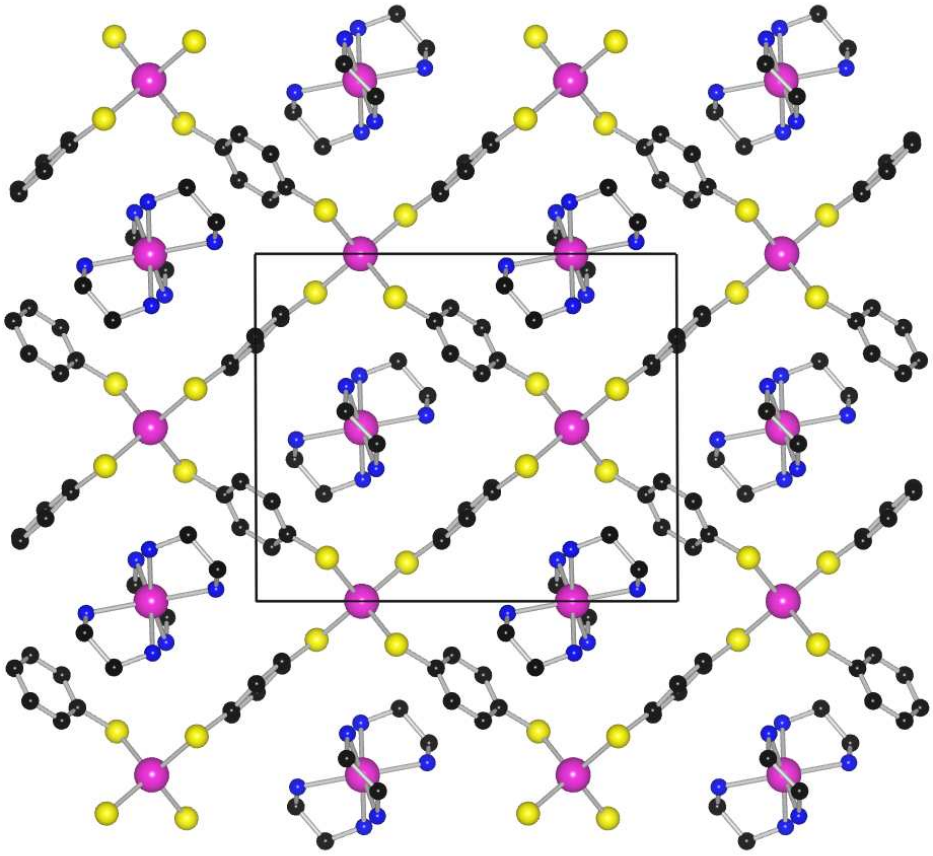

Figure 3.2: A $Cd(en)_3$ ion.

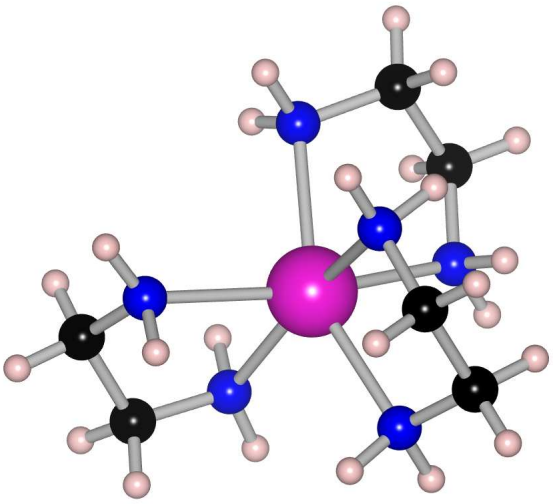

Figure 3.3: Rietveld refinement of $[Cd(en)_3][Cd(SC_6H_4S)_2]$. Blue dots are the measured data, the red line is the calculated fit from the refined structure, and the black line below is the difference between the two. Allowed peak positions are indicated by the tick marks.

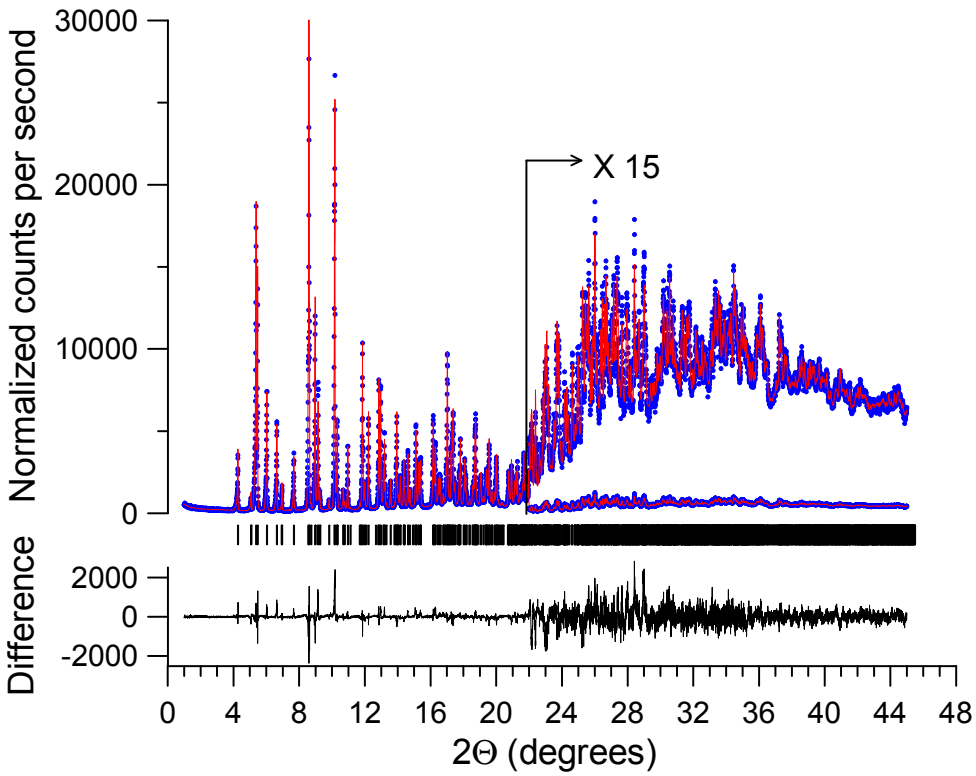

$[Cd(en)_3][Cd(SeC_6H_4Se)_2]$

Powder diffraction data for $[Cd(en)_3][Cd(SeC_6H_4Se)_2]$ was collected with a wavelength of 0.69694(3) Å, from a flat plate sample. The structure was solved under the assumption that it would be isostructural to that of $[Cd(en)_3][Cd(SC_6H_4S)_2]$. Due to the sample geometry, a correction for the changing illuminated volume was also included.

Figure 3.4: Rietveld refinement of $[Cd(en)_3][Cd(SeC_6H_4Se)_2]$. Blue dots are the measured data, the red line is the calculated fit from the refined structure, and the black line below is the difference between the two. Allowed peak positions are indicated by the tick marks.

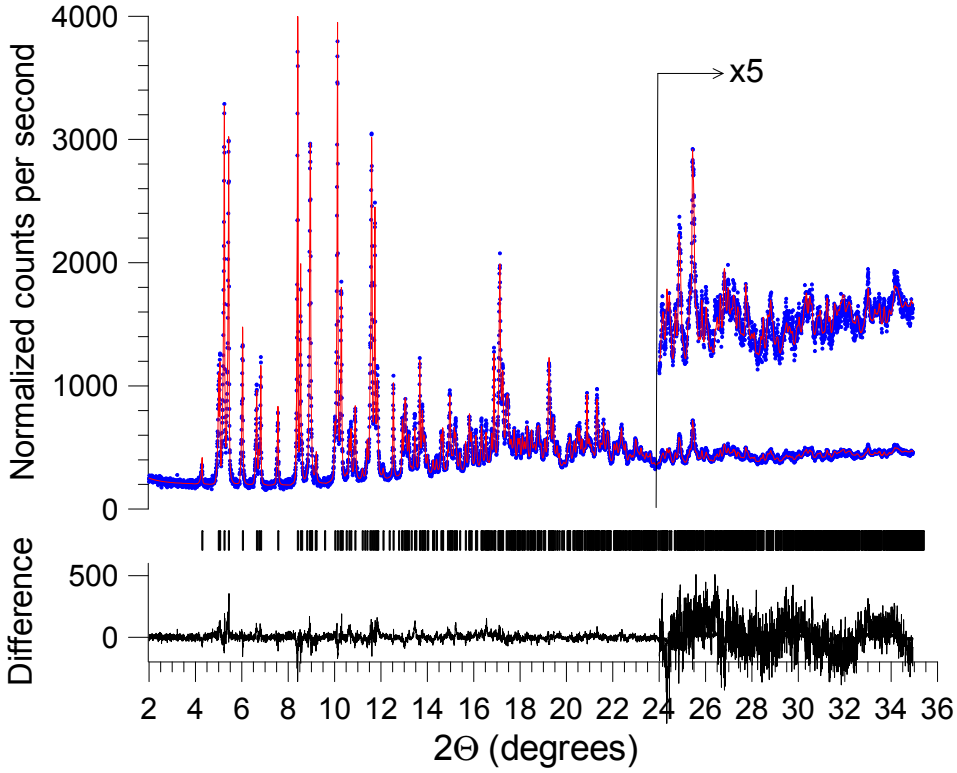

$[\mathbf{Zn(en)_3}][\mathbf{Zn(SC_6H_4S)_2}]$

Powder diffraction data was collected with a wavelength of 0.69695(3) Å, from a sample of $[Zn(en)_3][Zn(SC_6H_4S)_2]$ loaded into a flat plate. The structure was solved under the assumption that it would be isostructural to that of $[Cd(en)_3][Cd(SC_6H_4S)_2]$. Due to the sample geometry, a correction for the changing illuminated volume was also included.

Figure 3.5: Rietveld refinement of $[Zn(en)_3][Zn(SC_6H_4S)_2]$. Blue dots are the measured data, the red line is the calculated fit from the refined structure, and the black line below is the difference between the two. Allowed peak positions are indicated by the tick marks.

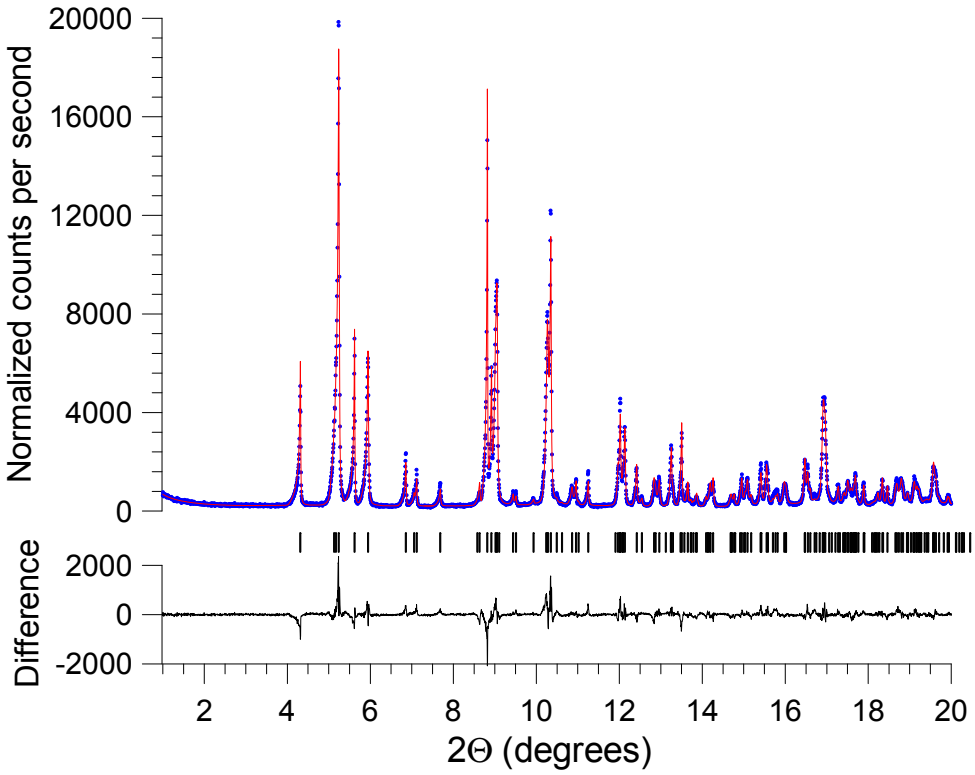

$[\mathbf{Mg_{0.82}Cd_{0.18}(en)_3}][\mathbf{Cd_{0.98}Mg_{0.02}(SC_6H_4S)_2}]$

Diffraction data for $[Mg_{0.82}Cd_{0.18}(en)_3][Cd_{0.98}Mg_{0.02}(SC_6H_4S)_2]$ was collected with a wavelength of 0.69853(3) Å, from a sample loaded into a 0.7 mm glass capillary. The structure was presumed to be isostructural to that of $[Cd(en)_3][Cd(SC_6H_4S)_2]$ with the Mg being primarily bonded with the ethylenediamine. In the structural refinement, the composition of the two metal-atom sites were allowed to vary independently while maintaining full occupancy, *i. e.*, as $Mg_{1-y}Cd_y$ and $Mg_{1-z}Cd_z$, where $0 \leq y \leq 1$ and $0 \leq z \leq 1$. Refinement of the diffraction data indicated a formula of $[Mg_{0.82}Cd_{0.18}(en)_3][Cd_{0.98}Mg_{0.02}(SC_6H_4S)_2]$. As expected, the hard acid Mg^{2+} segregated mainly to the site where it is coordinated by the hard base en, while the soft acid Cd^{2+} segregated almost completely to the site where it is coordinated by the soft base -SC_6H_4S-.

Figure 3.6: Rietveld refinement of $[Mg_{0.82}Cd_{0.18}(en)_3][Cd_{0.98}Mg_{0.02}(SC_6H_4S)_2]$. Blue dots are the measured data, the red line is the calculated fit from the refined structure, and the black line below is the difference between the two. Allowed peak positions are indicated by the tick marks.

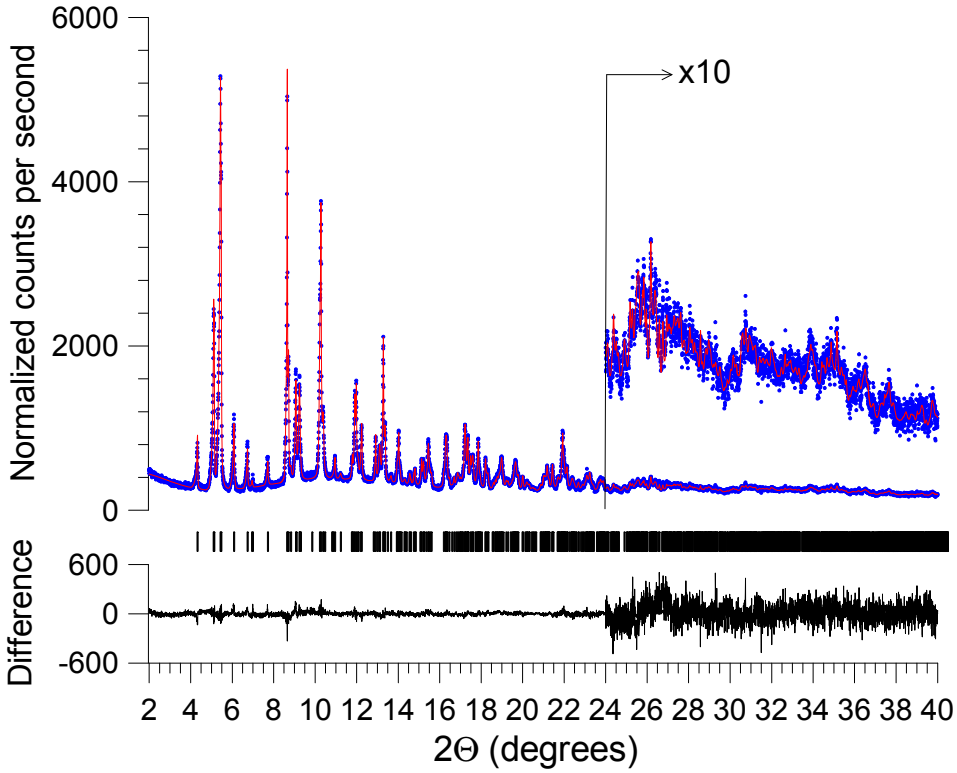

3.1.3 $[NR_4]_2[Cd_2(EC_6H_4E)_3]$ Crystal Preparation

Because the covalent $[Cd(SC_6H_4S)_2]^{2-}$ network of $[Cd(en)_3][Cd(SC_6H_4S)_2]$ is only 2-dimensional and has relatively large galleries where the cations reside, exchanging the $Cd(en)_3^{2+}$ cations of the already-synthesized $[Cd(en)_3][Cd(SC_6H_4S)_2]$ seemed feasible. Two NMe_4^+ cations occupy a volume roughly equivalent to a $[Cd(en)_3]^{2+}$ dication. However, when solid $[Cd(en)_3][Cd(SC_6H_4S)_2]$ was exposed to a solution of $[NMe_4][OTf]$ in acetonitrile at reflux for 24 h, no change in the $[Cd(en)_3][Cd(SC_6H_4S)_2]$ was evident by powder X-ray diffraction or other analytical methods. If, on the other hand, $[Cd(en)_3][Cd(SC_6H_4S)_2]$ was treated with 10 equivalents of $[NMe_4][Cl]$ in acetonitrile at reflux for 24 h, a transformation to a new, pale yellow compound with stoichiometry $[NMe_4]_2[Cd_2(SC_6H_4S)_3]$ occurred. The stoichiometry of the product was determined by CHN elemental analysis and the 1H NMR spectrum of a D_2O solution of the product that had been dissolved in concentrated HNO_3 [38].

A similar reaction of $[Cd(en)_3][Cd(SC_6H_4S)_2]$ with 20 equivalents of $[NEt_4][Cl]$ in acetonitrile at reflux yielded yellow $[NEt_4]_2[Cd_2(SC_6H_4S)_3]$. The structure of $[NEt_4]_2[Cd_2(SC_6H_4S)_3]$ was solved by synchrotron powder X-ray diffraction and is analogous to that of $[NMe_4]_2[Cd_2(SC_6H_4S)_3]$. Finally, treatment of $[Cd(en)_3][Cd(SeC_6H_4Se)_2]$ with 10 equivalents of $[NMe_4][Cl]$ in acetonitrile at reflux gave orange-yellow $[NMe_4]_2[Cd_2(SeC_6H_4Se)_3]$.

3.1.4 $[NR_4]_2[Cd_2(EC_6H_4E)_3]$ Structure Determination

$[NMe_4]_2[Cd_2(SC_6H_4S)_3]$

Two preparations of the material $[NMe_4]_2[Cd_2(SC_6H_4S)_3]$ were investigated by synchrotron X-ray powder diffraction in order to determine the crystallographic structure of the material. The structure was solved through the use of three separate datasets. The first was taken on a flat plate sample of dimension 10 mm x 0.5 mm x 0.5 mm with the use of a Ge(111) analyzer crystal and detected by a NaI scintillation counter. Over the course of data collection, θ was rocked by 1° at each point to improve powder averaging. Due to a limited supply of sample material, and subsequently small sample dimensions, two illuminated volume corrections were necessary, one to account for the changing illuminated length of the sample as θ was moved, and the other for the changing effective depth of the sample. The latter correction was necessary due to the incomplete absorption of the illuminating beam by the small sample depth. The possibility for preferred orientation, a common issue with related samples, could also not be ruled out for this dataset. The use of a capillary sample was precluded by the weak diffraction of the sample, and thus the prohibitively long count times required to obtain reasonable statistics with this point detector. Despite the issues with this dataset, it was successfully used to index the material as triclinic with lattice parameters of $a = 11.4967$ Å, $b = 10.6696$ Å, $c = 8.6955$ Å, $\alpha = 58.502°$, $\beta = 106.512°$, and $\gamma = 111.007°$.

The volume of the unit cell and the suggested chemical formula indicated that there would be only a single formula unit in the unit cell. A structure where the $Cd_2(SC_6H_4S)_3$ forms an anionic network, and the two NMe_4 are the

interstitial countercations was proposed. The proposed structure was modeled by treating the Cd_2S_6, C_6H_4, and NMe_4 units as Z-matrices with dummy atoms located at the center of the Cd_2S_6 and C_6H_4 units. The inversion symmetry of the Cd_2S_6 and C_6H_4 units suggested space group $P\bar{1}$ with the Cd_2S_6 anion located at the origin and the C_6H_4 rings on the other special positions. The NMe_4 cation, not having inversion symmetry, was necessarily positioned on a general site, thus producing two symmetry equivalent molecules. Subsequent refinement of this structure to the flat plate dataset was difficult, primarily due to the numerous corrections required by the sample geometry and the possibility of preferred orientation. Nevertheless, it was possible to find the correct position of the NMe_4 molecule.

To allow for reliable refinement of the proposed structure, two further datasets were collected. The first was taken using the same sample used for the flat plate data, this time loaded into a thin walled glass capillary of nominal diameter 0.5 mm. The capillary was spun during data collection to improve powder averaging, and the data was collected using a position sensitive detector (PSD) consisting of 640 pixels contained on a single Si strip. The use of the PSD vastly improved the time needed to collect a dataset, making the very long counting times necessary at each point, for this weakly diffracting sample, achievable. The final dataset was collected from a different preparation of the material, which was found to diffract more strongly, but contained an unidentified impurity. This sample was loaded into a nominal 0.7 mm diameter capillary and measured with the use of the analyzer crystal and the NaI detector.

In the case where a diffraction pattern contains an unknown impurity,

ordinary Rietveld refinement is not a viable option. However, refinement may still be carried out by using the robust refinement algorithm as developed by David [39]. This was implemented in the program *TOPAS-Academic* by continuous adjustment of the weight of each data point at each iteration of the refinement procedure. This effectively changed the function being minimized from the usual χ^2 to the robust version as defined by David. Details of the implementation are given in Chapter 7.

The data collected using the PSD was smoothed into equally spaced steps of 2θ and analyzed using *TOPAS-Academic*. The small capillary was used to give sharper peaks, the sample size being the primary contribution to the peak width, and, despite the lower resolution of the PSD compared to that of the analyzer crystal, the PSD and flat plate datasets are quite comparable in quality. However, the PSD dataset is free from the added complications of illuminated volume and, presumably, preferred orientation. The PSD dataset was refined according to the usual Rietveld method. The peak shape obtained from this detector is nearly a projection of the sample shape onto the flat detector face. Accordingly, the peaks were modeled as Gaussians convoluted with a half circle of width determined by the capillary diameter. The nature of the PSD also allows for a much higher, and more complicated background than that obtained with an analyzer crystal, although it is still well fit by an, albeit higher order, Chebychev polynomial.

Having refined the structure using the robust method and the PSD data, it was possible to then refine the original flat plate data by fixing the thermal parameter, which is highly correlated to the illuminated volume corrections, and refine the absorption and preferred orientation corrections. The inclu-

sion of preferred orientation gave negligible improvement to the fit, and so was excluded from the final model. The final model was refined against all three datasets simultaneously, with the only difference being unique thermal parameters and peak shape functions for each dataset. Although refinement against each single dataset gave nearly identical solutions (Fig. 3.7), it was determined that the best means of refinement was to utilize all available data, meaning the three diffraction patterns simultaneously (Figs. 3.8, 3.9, 3.10).

Figure 3.7: Overlay of the three refined structures of $[NMe_4]_2[Cd_2(SC_6H_4S)_3]$ from data taken on the PSD, in flat plate geometry, and in capillary geometry. There is not appreciable difference between the three, and the final structure refinement was a simultaneous refinement of all three data sets (not shown).

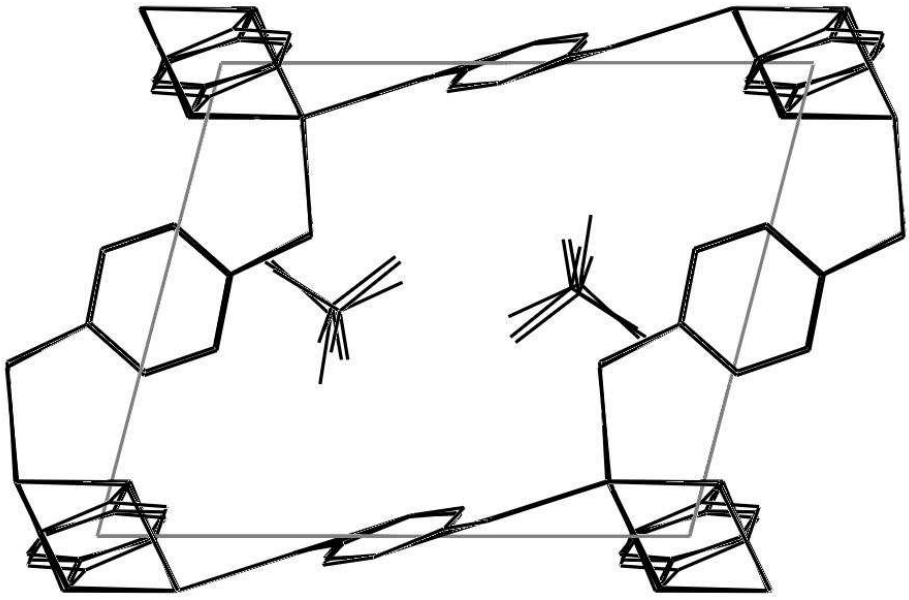

Figure 3.8: Rietveld refinement of $[NMe_4]_2[Cd_2(SC_6H_4S)_3]$ data taken on the PSD. Blue dots are the measured data, the red line is the calculated fit from the refined structure, and the black line below is the difference between the two. Allowed peak positions are indicated by the tick marks.

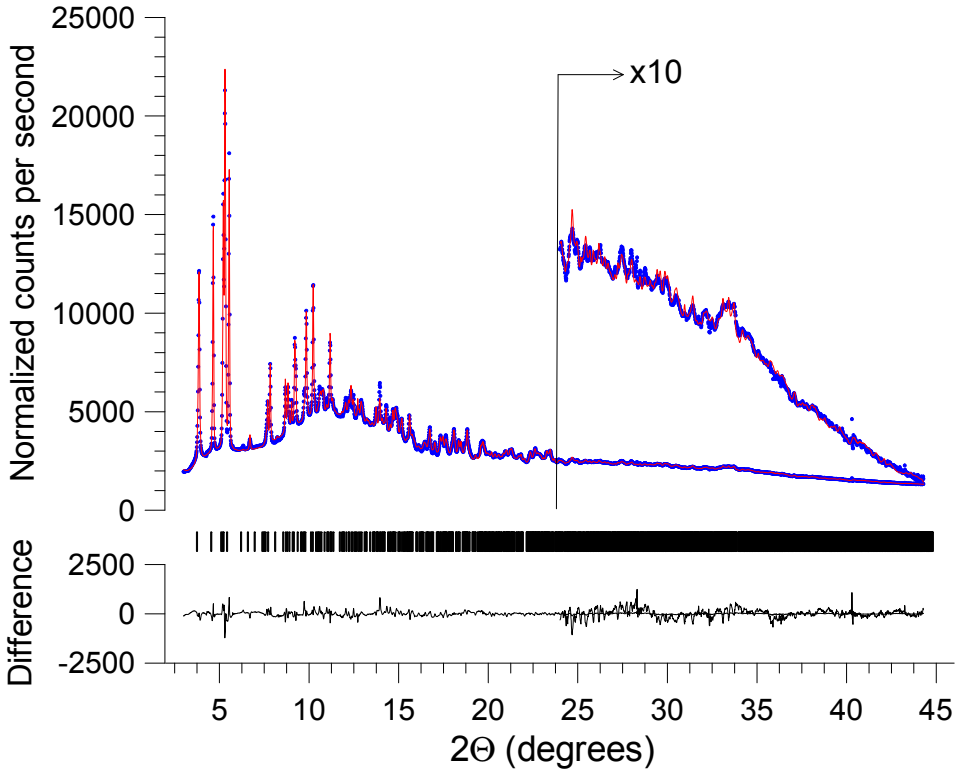

Figure 3.9: Rietveld refinement of $[NMe_4]_2[Cd_2(SC_6H_4S)_3]$ data taken in flat plate geometry. Blue dots are the measured data, the red line is the calculated fit from the refined structure, and the black line below is the difference between the two. Allowed peak positions are indicated by the tick marks.

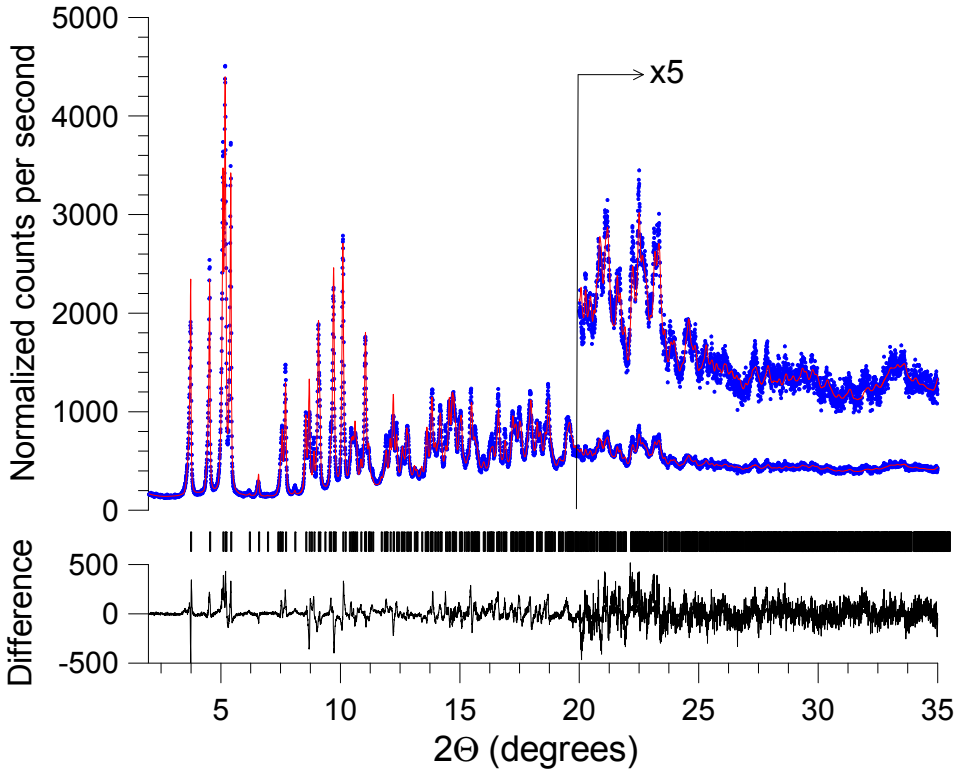

Figure 3.10: Robust Rietveld refinement of $[NMe_4]_2[Cd_2(SC_6H_4S)_3]$ data taken in capillary geometry. Blue dots are the measured data, the red line is the calculated fit from the refined structure, and the black line below is the difference between the two. Allowed peak positions are indicated by the tick marks.

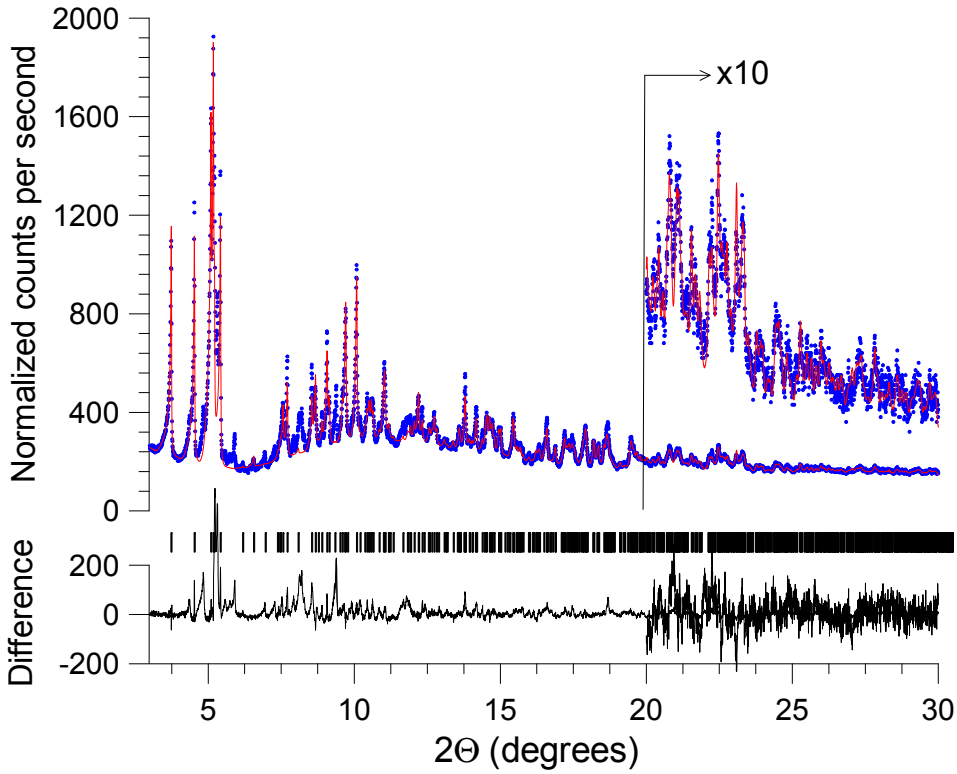

$[NEt_4]_2[Cd_2(SC_6H_4S)_3]$ and $[NMe_4]_2[Cd_2(SeC_6H_4Se)_3]$

Samples of $[NEt_4]_2[Cd_2(SC_6H_4S)_3]$ and $[NMe_4]_2[Cd_2(SeC_6H_4Se)_3]$ were measured in capillary geometry. The structure of $[NEt_4]_2[Cd_2(SC_6H_4S)_3]$ was found to be analagous to that of $[NMe_4]_2[Cd_2(SC_6H_4S)_3]$ (Fig. 3.11). The sample of $[NMe_4]_2[Cd_2(SeC_6H_4Se)_3]$ was found to contain a large amount of an unidentified impurity. However, because the sample was believed to be isostructural to the sulfur analogue, a model was created and refined using the robust procedure described. The robustly refined structure was chemically feasible (Fig. 3.14) and the fit to the data was not unreasonable under the assumption of a large impurity contribution, giving a strong indication that the structure under consideration was correct (Fig. 3.12). This was later confirmed by the availability of a pure sample (Fig. 3.13).

Figure 3.11: Rietveld refinement of $[NEt_4]_2[Cd_2(SC_6H_4S)_3]$ data taken in capillary geometry. Blue dots are the measured data, the red line is the calculated fit from the refined structure, and the black line below is the difference between the two. Allowed peak positions are indicated by the tick marks.

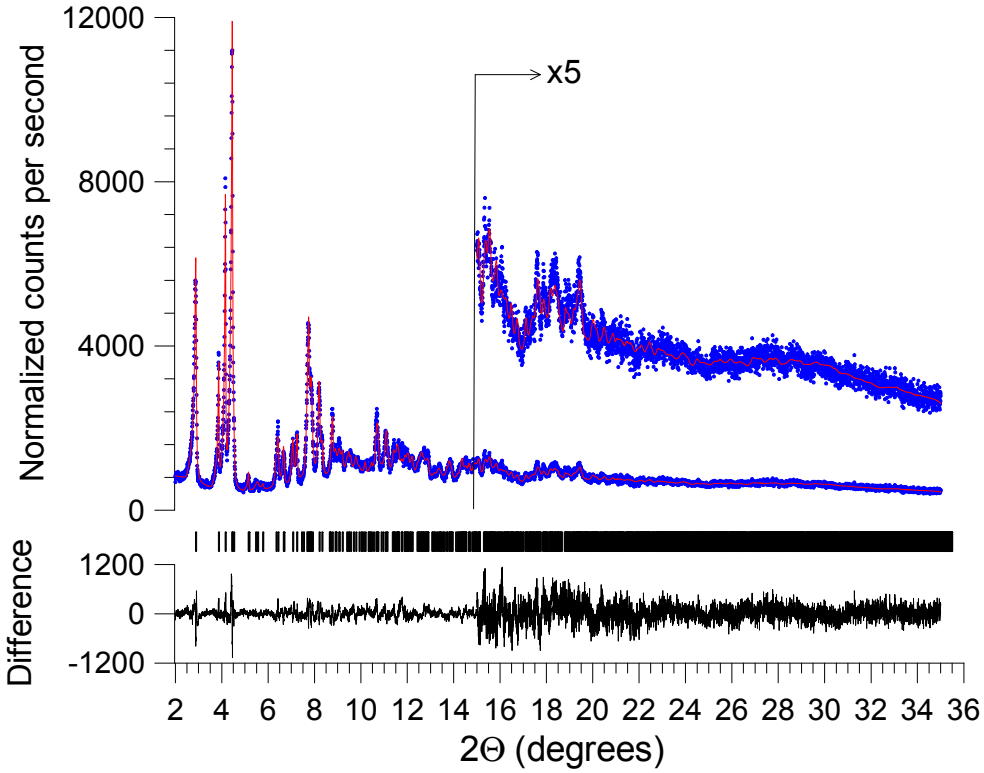

Figure 3.12: Robust Rietveld refinement of $[NMe_4]_2[Cd_2(SeC_6H_4Se)_3]$ data taken in capillary geometry. Blue dots are the measured data, the red line is the calculated fit from the refined structure, and the black line below is the difference between the two. Allowed peak positions are indicated by the tick marks.

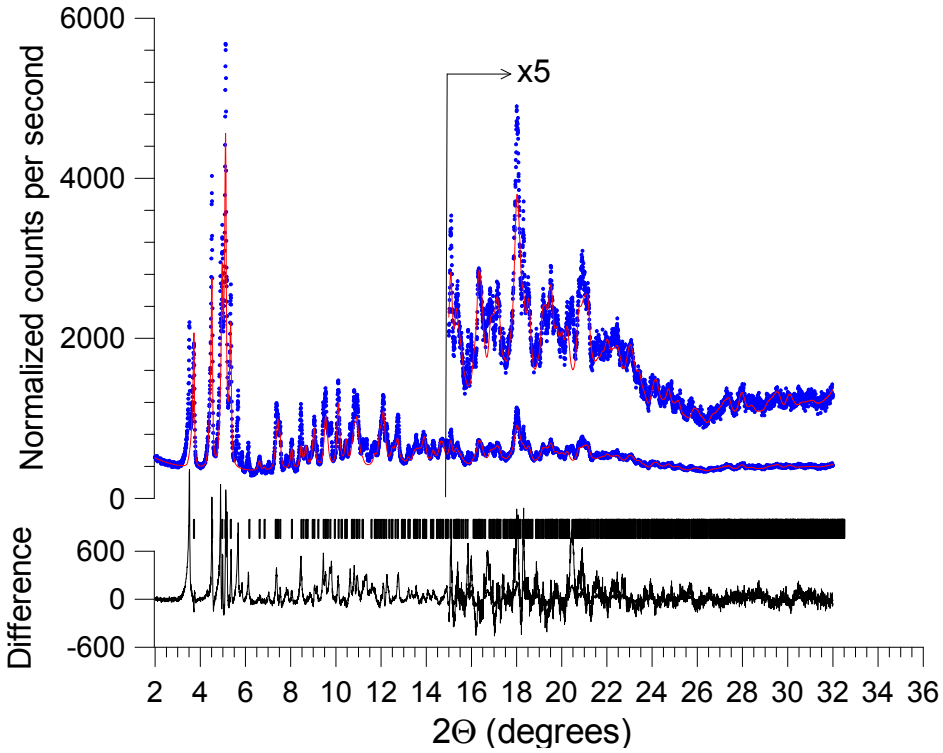

Figure 3.13: Rietveld refinement of $[NMe_4]_2[Cd_2(SeC_6H_4Se)_3]$ data taken in capillary geometry. Blue dots are the measured data, the red line is the calculated fit from the refined structure, and the black line below is the difference between the two. Allowed peak positions are indicated by the tick marks.

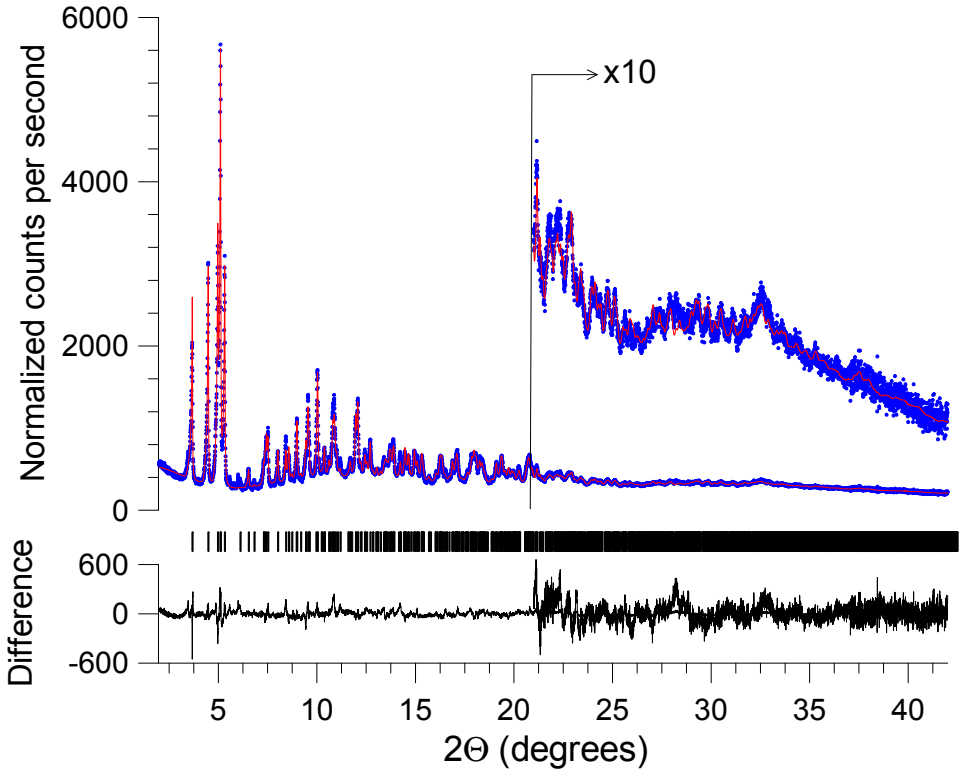

Figure 3.14: The structure of $[NMe_4]_2[Cd_2(SeC_6H_4Se)_3]$ viewed along the *c*-axis. Hydrogen atoms are omitted for clarity.

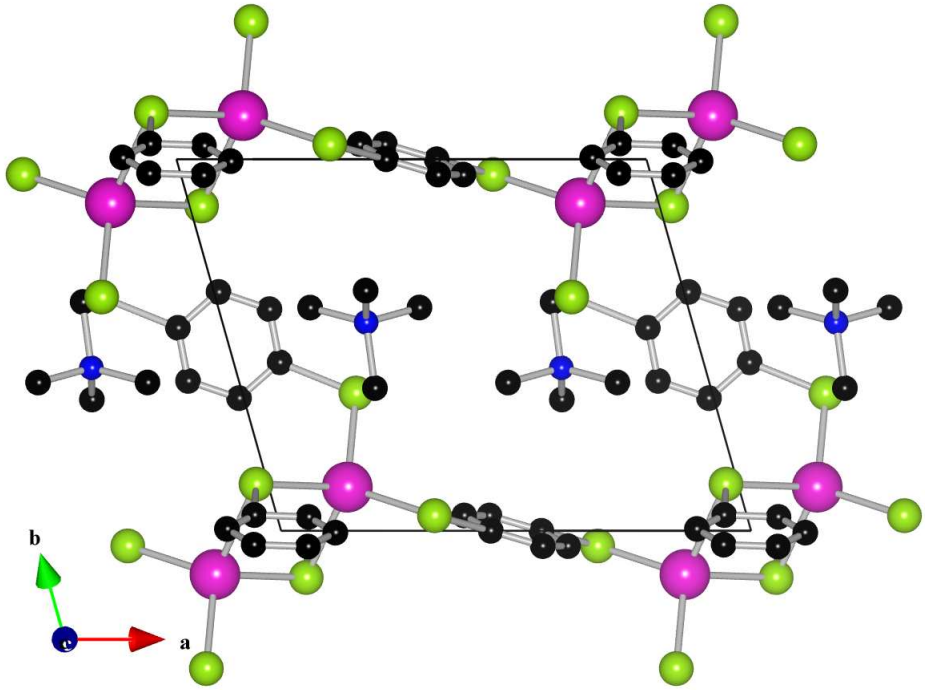

3.1.5 Discussion

The structure of $[NMe_4]_2[Cd_2(SC_6H_4S)_3]$ is significantly different from that of $[Cd(en)_3][Cd(SC_6H_4S)_2]$. It contains Cd_2S_6 units very similar to those previously observed in the $[Cd_2(SPh)_6]^{2-}$ anion [40]. There is a Cd_2S_6 (Fig. 3.15) unit at each corner of the triclinic unit cell, and each is connected to six other Cd_2S_6 units via SC_6H_4S linkages. The two bridging sulfur atoms of the Cd_2S_6 units connect via -C_6H_4- to two other Cd_2S_6 units (at the bridging sulfurs), forming chains along the *c*-axis. Similarly, two of the terminal sulfur atoms connect via SC_6H_4S to two other Cd_2S_6 units along the *a*-axis. Finally the last two terminal sulfur atoms connect to other Cd_2S_6 units in the [01-1] direction. In this way a very distorted cubic network of Cd_2S_6 units linked by -C_6H_4- moieties is formed (Fig. 3.16). The NMe_4^+ cations reside in the open galleries of the $[Cd_2(SC_6H_4S)_3]^{2-}$ network.

Figure 3.15: A unit of Cd_2S_6 which, when connected by phenol rings, forms the basis for the three dimensional network structures of $[NR_4]_2[Cd_2(EC_6H_4E)_3$.

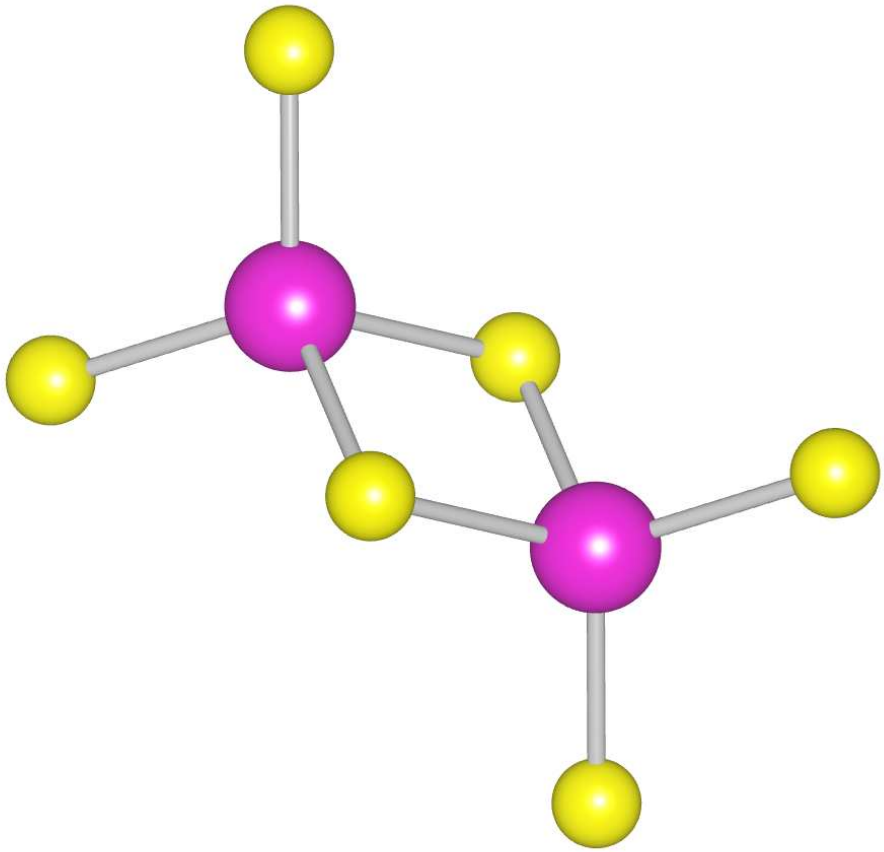

Figure 3.16: The structure of $[NMe_4]_2[Cd_2(SC_6H_4S)_3]$, viewed along the *c*-axis, with the NMe_4^+ ions removed for clarity.

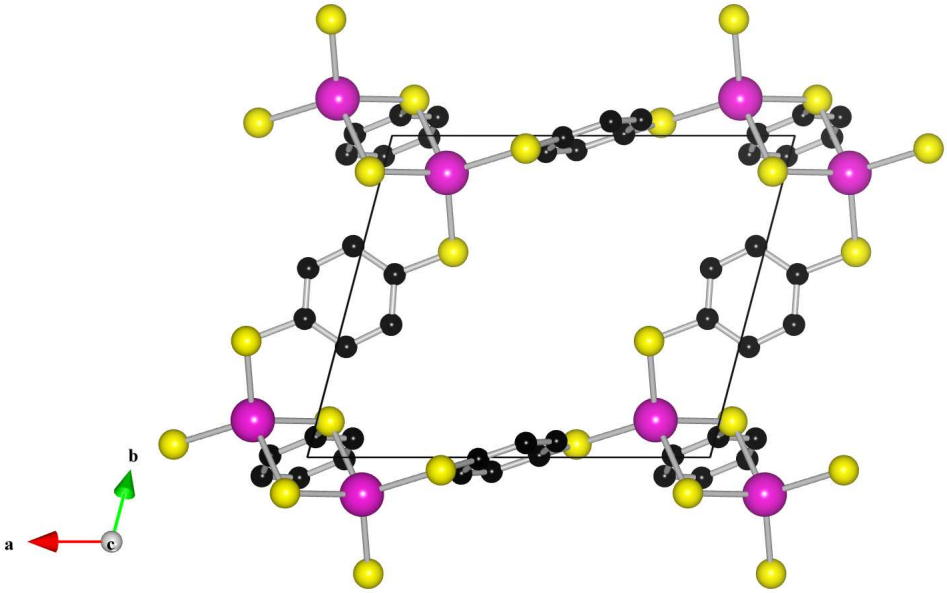

3.2 Group IV-VI Analogues

3.2.1 Crystal Preparation

All network-forming reactions were carried out under N_2 in degassed ethylenediamine; the products are air-stable and the workup and subsequent handling was done without protection from air by Dayna Turner and Tom Vaid.

3.2.2 Structure Solution

All powder diffraction patterns were collected at beamline X16C at the National Synchrotron Light Source at Brookhaven National Laboratory. All indexing, structure solution, and refinement was performed using *TOPAS-Academic*.

$\mathbf{Pb_2(S_2C_6H_2S_2)(en)}$

The sample of $Pb_2(S_2C_6H_2S_2)(en)$ was measured in a flat plate geometry using a single crystal quartz sample holder with dimensions were 27 mm x 8 mm x 0.5 mm. Data was taken while rocking θ by 1° per point over a 2θ range of 1° to 41° in steps of 0.005° with a counting time of 2-6 seconds per point, with longer count times being used at higher angles (Fig. 3.17). A separate sample was loaded into a nominal 0.7 mm glass capillary with roughly 4x the amount, by volume, of Al_2O_3 NIST standard material SRM 674 (Fig. 3.18). This was done to prevent preferred orientation of the capillary sample. The data was indexed as space group $P\bar{1}$ with lattice parameters $a = 6.9383$ Å, $b = 7.1449$ Å, $c = 7.8908$ Å, $\alpha = 85.893°$, $\beta = 66.562°$, and $\gamma = 67.593°$. Both

the ethylenediamine and $S_2C_6H_2S_2$ molecules were modeled as Z-matrices and located on inversion centers with the Pb atom being located on a general position. For the Z-matrices, the aromatic C-C bond, S-C bond, and N-C bond lengths were allowed to refine while the C-C bond in the ethylenediamine molecule was fixed at 1.5 Å. All torsion angles and bond angles were kept fixed. A simultaneous refinement was performed in *TOPAS-Academic* of both data sets with a preferred orientation correction using the March-Dollase model for the flat plate data set [32]. This allowed the data with no preferred orientation to constrain the correction allowed for the flat plate data. The preferred orientation direction was found to be the (111) direction with a March parameter of 0.90. For the final refinement, only the flat plate data was used with the preferred orientation parameter held fixed with the value found from the simultaneous refinement.

Figure 3.17: Rietveld refinement of $Pb_2(S_2C_6H_2S_2)(en)$ data taken in flat plate geometry. Blue dots are the measured data, the red line is the calculated fit from the refined structure, and the black line below is the difference between the two. Allowed peak positions are indicated by the tick marks.

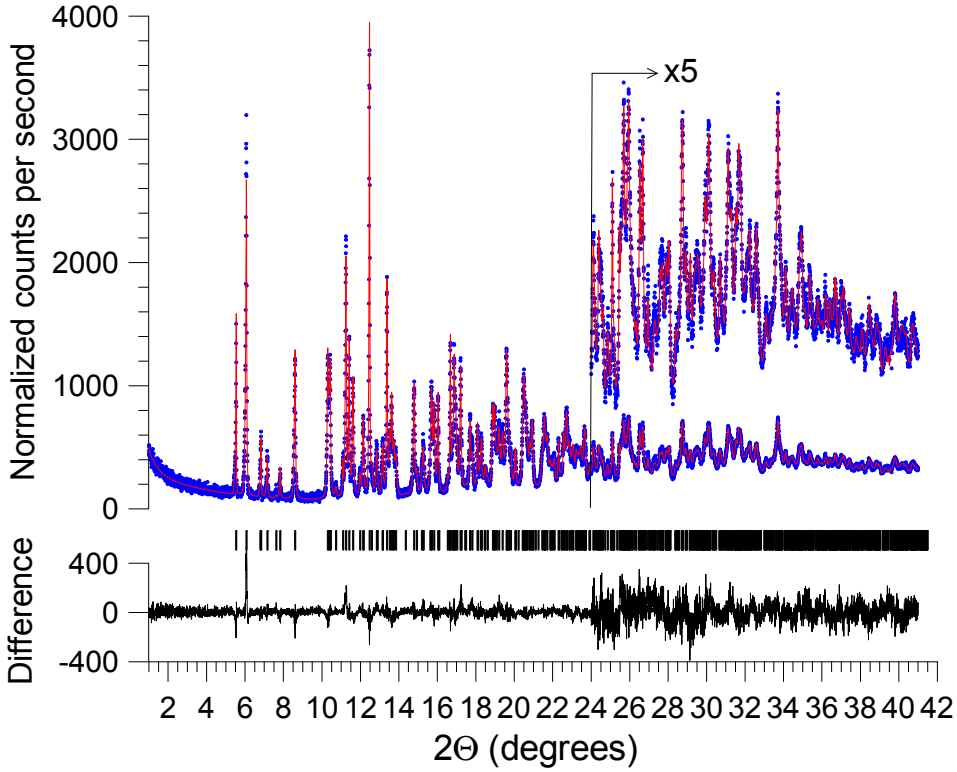

Figure 3.18: Rietveld refinement of $Pb_2(S_2C_6H_2S_2)(en)$ data taken in capillary geometry and mixed with Al_2O_3. Blue dots are the measured data, the red line is the calculated fit from the refined structure, and the black line below is the difference between the two. Allowed peak positions are indicated by the tick marks (upper are Al_2O_3 and lower are $Pb_2(S_2C_6H_2S_2)(en)$).

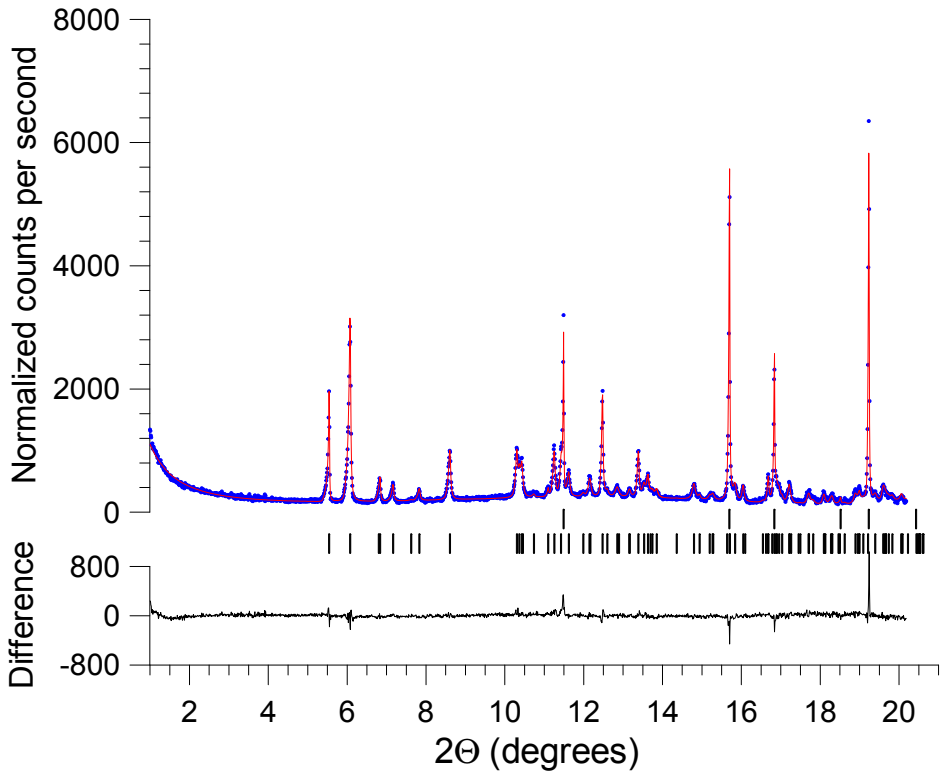

Figure 3.19: Structure of $Pb_2(S_2C_6H_2S_2)(en)$ viewed along the [1-10] direction.

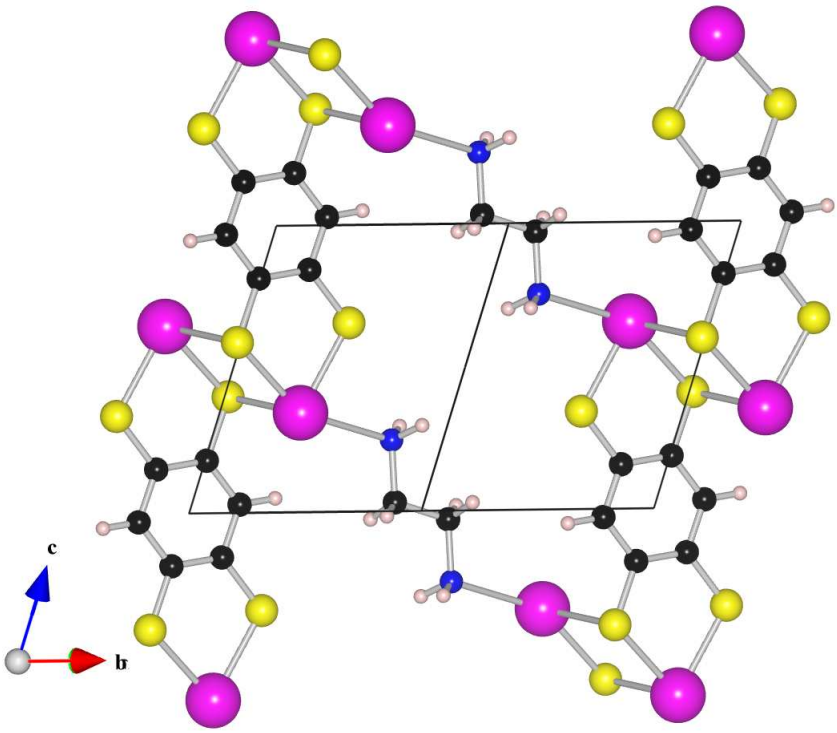

$\mathbf{Pb_3(C_6S_6)}$

A sample of $Pb_3(C_6S_6)$ was mixed with finely ground cork and loaded into a nominal 0.7 mm glass capillary. The cork was used to lower the absorption of the sample and to lessen the chance of preferred orientation. Data was taken over a 2θ range of 1° to 40° in steps of 0.005° while rotating the sample about the capillary axis at a rate of 2 Hz and a counting time of 2 seconds per point (Fig. 3.20). The data was indexed as $P3$ with lattice parameters of $a = 8.964$ Å and $c = 3.9576$ Å. A structure solution was found in $P6/mmm$, a higher symmetry space group with the same extinction class. Although the possibility of a lower symmetry group can not be excluded, it is not required by the powder data. Due to the high symmetry of the final structure, there are only three independent atoms, one of each species. The Pb atom lies on a special symmetry position at the body center, while both the S and C atoms lie on special positions in the $c = 0$ plane.

There are layers of Pb atoms and parallel layers of C_6S_6 units in the $a - b$ crystallographic plane (Fig. 3.2.2). Each S coordinates four Pb atoms, and each Pb is coordinated by eight S atoms. The coordination of Pb is distorted cubic; Pb is at the center of a rectangular prism of eight S atoms with S-S distances of 3.17 Å, 3.47 Å, and 3.96 Å. All Pb-S distances are 3.07 Å.

Figure 3.20: Rietveld refinement of $Pb_3(C_6S_6)$ data taken in capillary geometry. Blue dots are the measured data, the red line is the calculated fit from the refined structure, and the black line below is the difference between the two. Allowed peak positions are indicated by the tick marks.

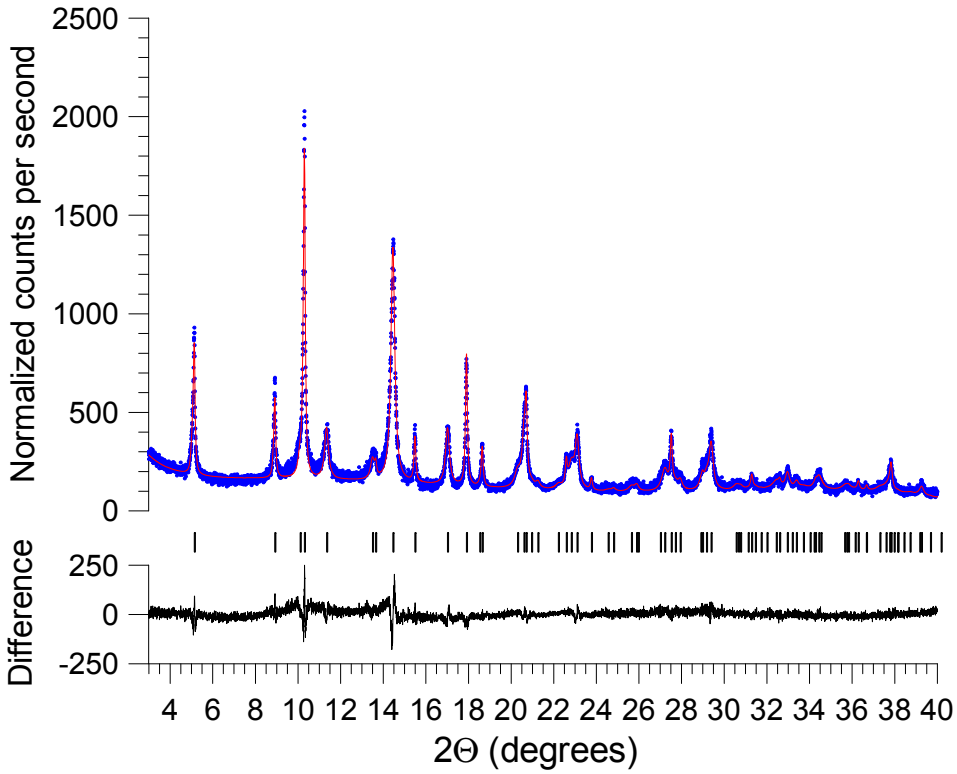

Figure 3.21: View of the structure of $Pb_3(C_6S_6)$ as seen along the c-axis (a) and along the a-axis (b).

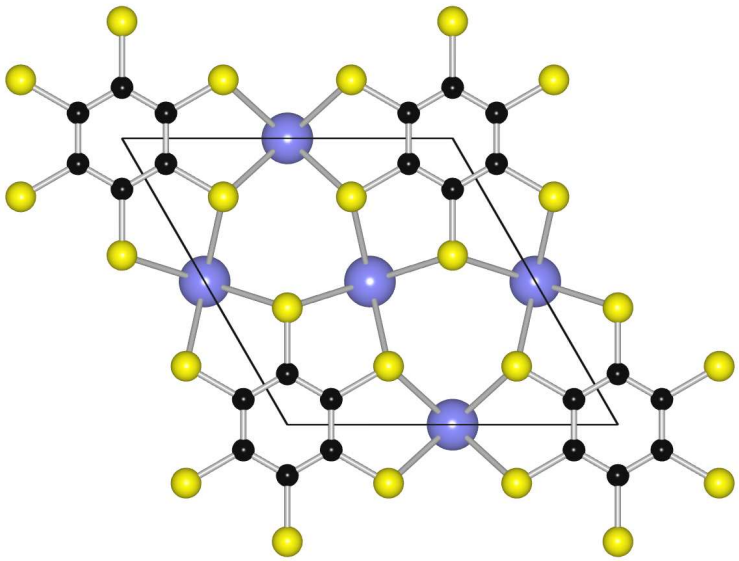

(a)

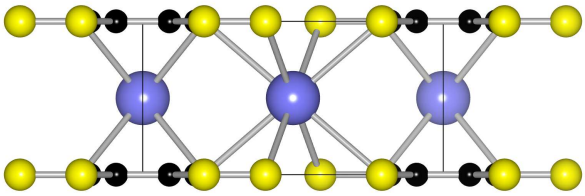

(b)

$Pb_3(SeC_6H_4Se)_3(en)_2$

Capillary data was taken at a wavelength of 0.697 Å. The data was indexed as $P3c1$ with $a = 16.6563$ Å and $c = 18.6857$ Å. Initially, the structure was studied in space group $P\bar{6}c2$ due to the larger multiplicity of the general position, thus requiring fewer independent atoms in the final structure. The Pb atoms were found through direct methods using the program *EXPO* [41], which comprised the starting structure for simulated annealing trials to find the lighter atoms. A structure was found in $P\bar{6}c2$ with one Pb atom on a general position, and three Pb atoms on sites with 3.2 symmetry, and thus multiplicity of two. The phenol ring and Se atoms were placed on the mirror at fractional coordinate $z = 1/4$. This was treated as a Z-matrix consisting of three C atoms and a single Se atom, the rest of the atoms were generated by the mirror. The general position Pb atom was also treated as a Z-matrix together with the en molecule. Subsequent refinement of this structure yielded a sensible structure, but a poor fit to the powder diffraction data (Fig. 3.22).

By breaking the symmetry imposed by the mirror at $z = 1/4$, the space group is reduced to $P3c1$. Other consequences are that the multiplicity of the general position decreases by a factor of two, and the phenol rings are no longer constrained to orient normal to the $a - b$ plane. The point group symmetry of the three special position Pb atoms is also changed. A structure equivalent to that found in $P\bar{6}c2$ was created by extending the phenol-Se Z-matrices to compensate for the lost mirror symmetry, and adding another general position Pb-en Z-matrix at the point originally occupied by the mirror generated one. Subsequent refinement of this structure, with no artificial mirror sym-

metry imposed, yielded a significantly better fit to the data (Fig. 3.23). It should be noted that an impurity was present in the sample, accounting for the extraordinarily sharp peaks which are not fit by the model.

Figure 3.22: Rietveld refinement of $Pb_3(SeC_6C_4Se)_3(en)_2$ data taken in capillary geometry with space group $P\bar{6}c2$. Blue dots are the measured data, the red line is the calculated fit from the refined structure, and the black line below is the difference between the two. Allowed peak positions are indicated by the tick marks.

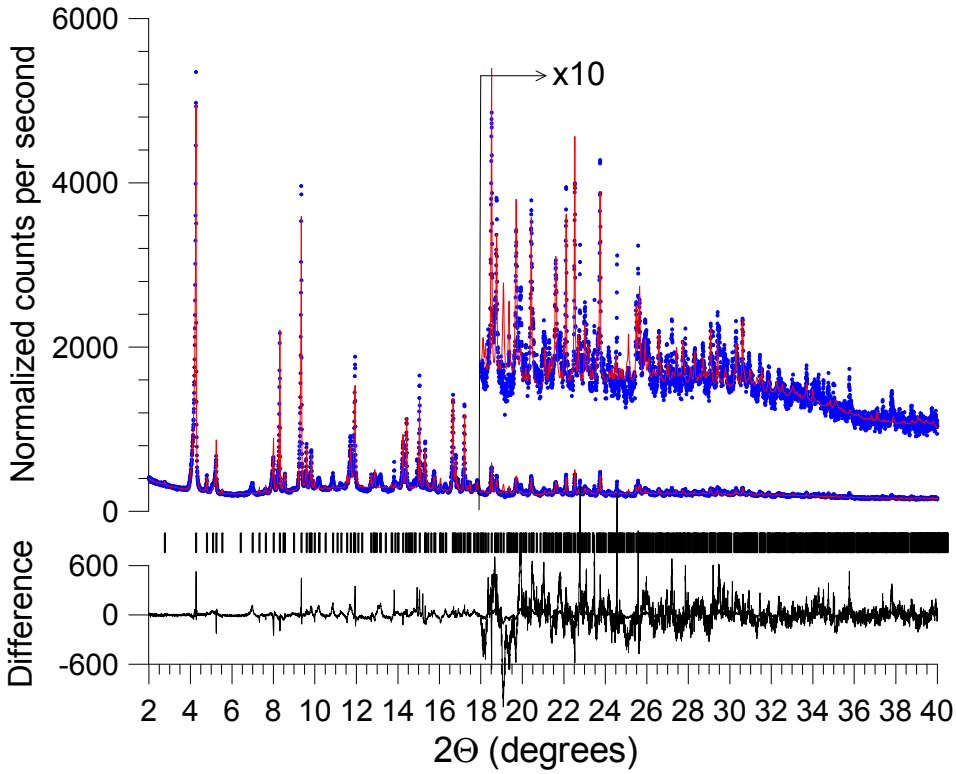

Figure 3.23: Rietveld refinement of $Pb_3(SeC_6C_4Se)_3(en)_2$ data taken in capillary geometry with space group $P3c1$. Blue dots are the measured data, the red line is the calculated fit from the refined structure, and the black line below is the difference between the two. Allowed peak positions are indicated by the tick marks.

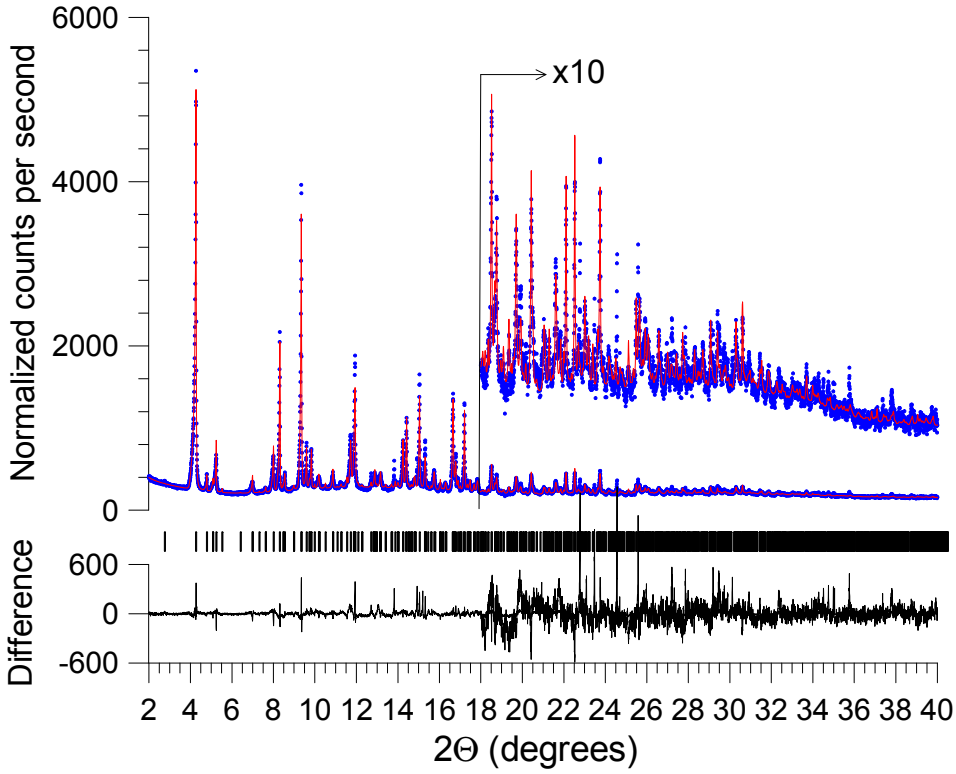

Figure 3.24: The structure of $Pb_3(SeC_6C_4Se)_3(en)_2$ showing (a.) one layer of Pb and Se in the *ab* plane, (b.) the connectivity of these layers by phenol rings, and (c.) the entire structure as viewed along the *c*-axis.

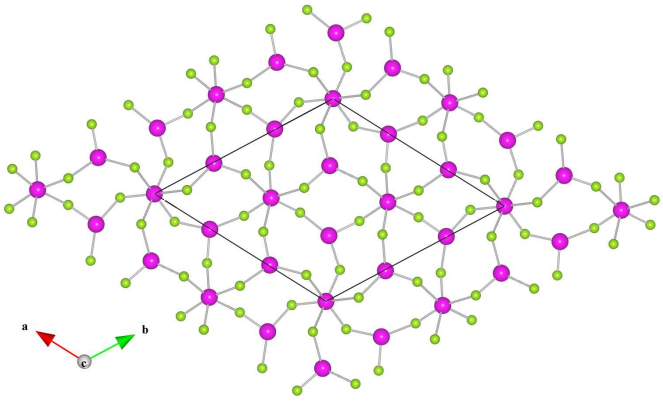

(a)

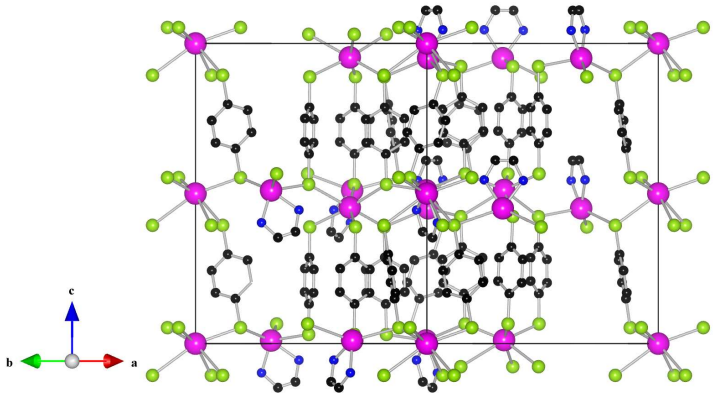

(b)

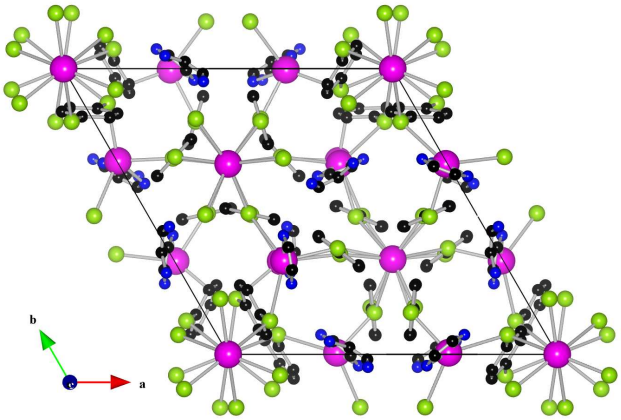

(c)

3.3 $Tl_2(SC_6H_4S)$ and $Tl_2(SeC_6H_4Se)$

3.3.1 Crystal Preparation

Thallium acetate (0.185 g, 0.703 mmol) and 1,4-benzenedithiol (0.050 g, 0.352 mmol) were combined in 8 mL of ethylenediamine. The suspension was heated to reflux for 16 hours and then cooled to room temperature. The orange precipitate was isolated by filtration and washed with methanol and ether, yielding yellow $Tl_2(SC_6H_4S)$.

Thallium acetate (0.1234 g, 0.468 mmol) and 1,4-(diacetylseleno)benzene (0.075 g, 0.234 mmol) were combined in 5 mL of ethylenediamine. The suspension was heated to reflux for 16 hours, then cooled to room temperature. The red precipitate was isolated by filtration and washed with methanol and ether yielding red $Tl_2(SeC_6H_4Se)$.

3.3.2 Structure Solution

All powder diffraction patterns were collected at beamline X16C at the National Synchrotron Light Source at Brookhaven National Laboratory. All indexing, structure solution, and refinement was performed using *TOPAS-Academic*. In order to decrease sample absorption, the samples were mixed with finely ground cork before loading into capillaries. This diluted the samples to prevent absorption corrections as well as ensuring no preferred orientation.

$\mathbf{Tl_2(SC_6C_4S)}$

The aromatic ring was modelled as a Z-matrix. As it lies on an inversion center, only half of the ring was included. The sulfur atoms were included in the Z-matrix and constrained to lie in the plane of the ring and to extend at an angle of 120° from the next nearest carbon atom. The only refinable parameters of the Z-matrix were the aromatic bond length and the C-S distance. The Tl atoms were located on a general position. A single, isotropic thermal parameter was used for all non-hydrogen atoms in each structure. Hydrogen atoms were given a thermal parameter of 1 and tethered to their respective carbon atoms at a distance of 1 Å. No Hydrogen parameters were refined. The refinement is shown in Figure 3.25. There was observed to be a mild amount of anisotropic peak broadening. To account for this, the Stephens model of anisotropic strain broadening was included in the refinement [33].

Figure 3.25: Rietveld refinement of $Tl_2(SC_6C_4S)$ data taken in capillary geometry. Blue dots are the measured data, the red line is the calculated fit from the refined structure, and the black line below is the difference between the two. Allowed peak positions are indicated by the tick marks.

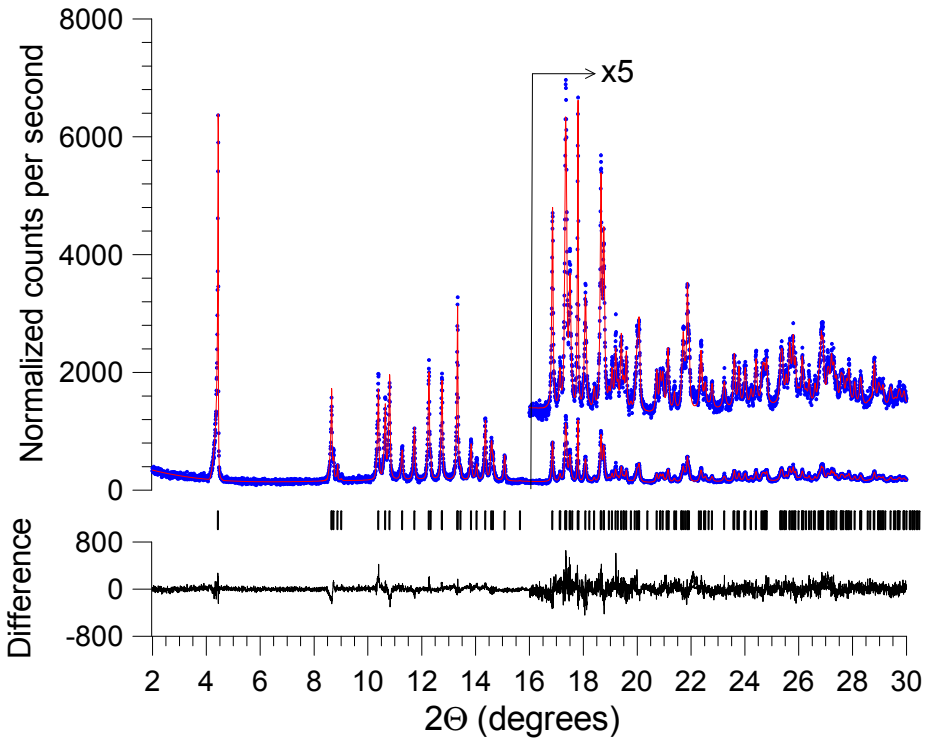

Figure 3.26: The structure of $Tl_2(SC_6C_4S)$

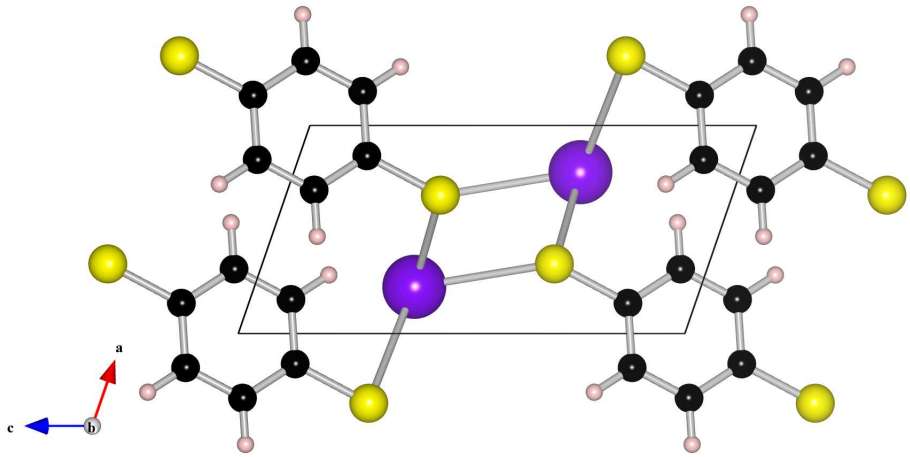

$Tl_2(SeC_6C_4Se)$

The structure was modeled as isostructural to that of the sulfur analogue, with the refinement performed under the same conditions (Fig. 3.27). There was observed to be a mild amount of anisotropic peak broadening. To account for this, the Stephens model of anisotropic strain broadening was included in the refinement [33].

Figure 3.27: Rietveld refinement of $Tl_2(SeC_6C_4Se)$ data taken in capillary geometry. Blue dots are the measured data, the red line is the calculated fit from the refined structure, and the black line below is the difference between the two. Allowed peak positions are indicated by the tick marks.

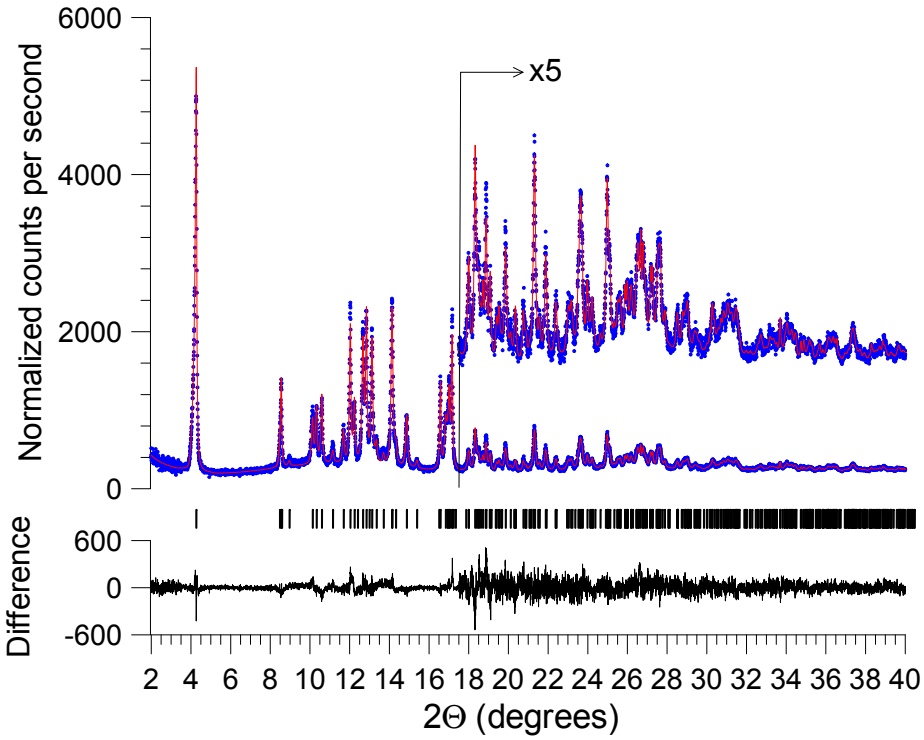

Figure 3.28: The structure of $Tl_2(SeC_6C_4Se)$

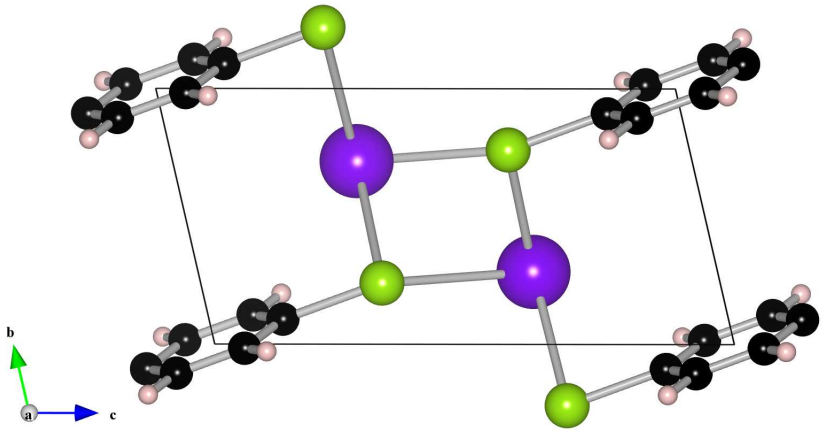

3.4 Discussion

While the majority of these materials were not found to semiconduct, having pressed pellet conductivities on the order of $10^{-12}\Omega^{-1}\text{cm}^{-1}$, three potential candidates were identified. $Pb_3(SeC_6C_4Se)_3(en)_2$, when doped with both Tl and Bi, appears to yield materials with a small but measureable conductivity of $4 \times 10^{-11}\Omega^{-1}\text{cm}^{-1}$. The pressed pellet conductivity of $Tl_2(SeC_6C_4Se)$ is slightly more encouraging with a value of $1.4 \times 10^{-10}\Omega^{-1}\text{cm}^{-1}$ at room temperature. In contrast, $Pb_3(C_6S_6)$ has a conductivity of $2 \times 10^{-6}\Omega^{-1}\text{cm}^{-1}$ at room temperature, which may be raised to $1 \times 10^{-4}\Omega^{-1}\text{cm}^{-1}$ upon doping by Tl. Variable-temperature measurements indicate that $Pb_3(C_6S_6)$ follows an Arrhenius type behavior with an activation energy of 0.37 eV (Figs. 3.30 and 3.29).

Despite the poor conductivity of the majority of these materials, they nevertheless represent a significant contribution to the still very small class of metal-organic-framework materials based on metal-sulfur or metal-selenium bonds rather than the much more common metal-oxygen or metal-nitrogen bonds. It is expected that the softer and more electronegative sulfur and selenium linkages are more likely to lead to semiconducting metal-organic-frameworks in the future.

Figure 3.29: Visible absorption spectrum of Pb3(C6S6). Figure taken from [37].

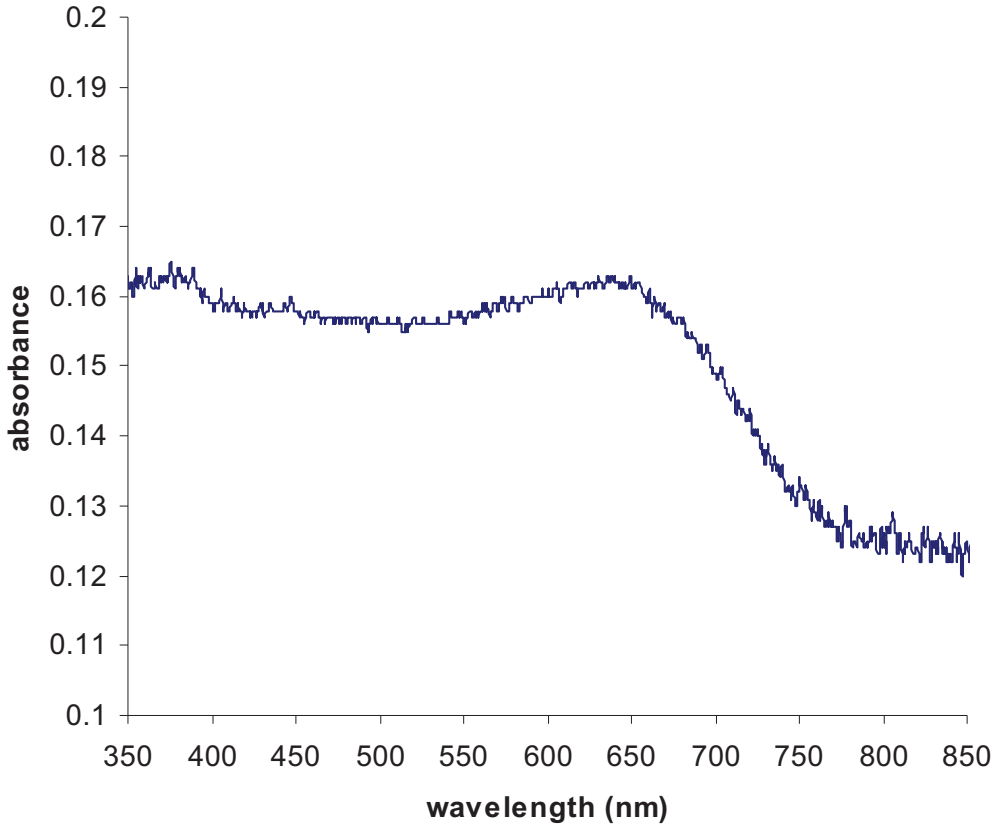

Figure 3.30: Variable-temperature conductivity of $Pb_3(C_6S_6)$. Squares are the cooling cycle and circles are the warming cycle. Figure taken from [37].

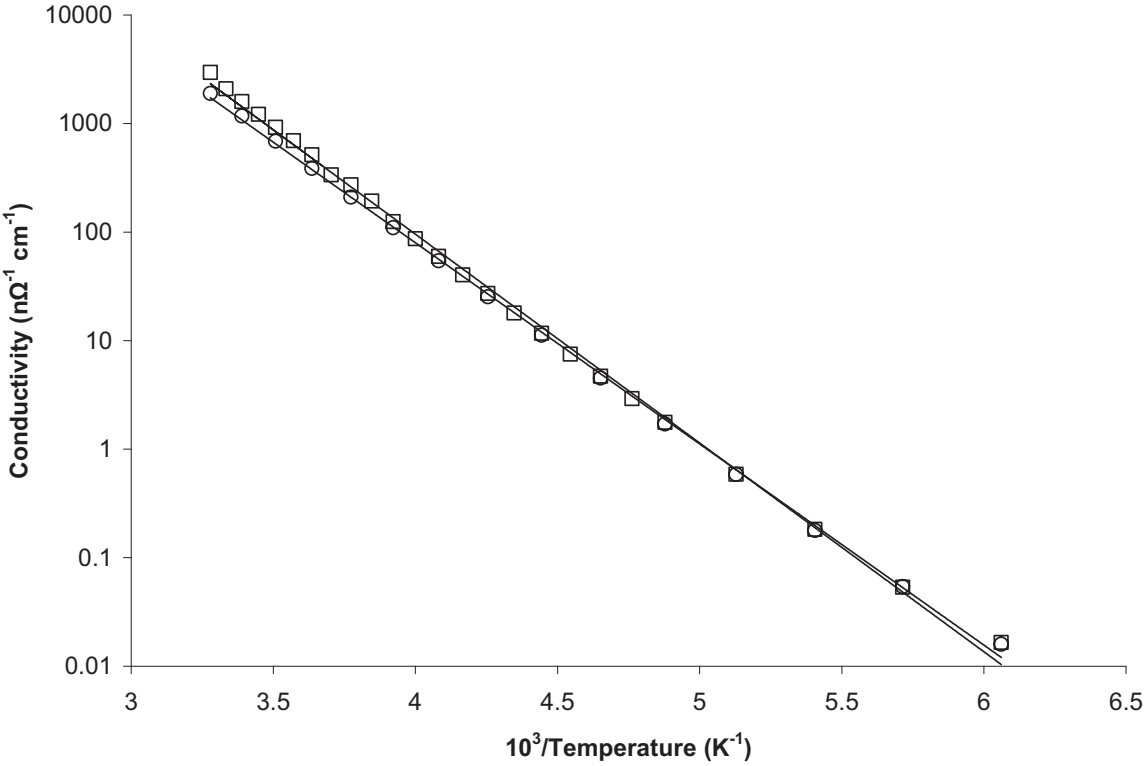

Chapter 4

Molecular Magnets

Magnetic materials have long been important, both technologically and scientifically. Historically, the study of magnets has been limited to inorganic elements, alloys, and transition metal oxides, structurally all rather simple materials prepared from metallurgical methods. However, with the discovery of the first molecule based magnet in 1985 [42], the possibility of preparing magnets using the diverse methods available to organic chemistry, and exhibiting the broad range of tuneable properties characteristic of organic materials was realized. Organic based magnets are materials in which the magnetic interaction of transition metals is mediated by unpaired s or p electrons on organic acceptor molecules. The rich structure of organic chemistry allows one to make many small adjustments to the acceptor molecules, in principle tuning the structure-property relation to create materials exhibiting desired properties. While such tunability exists in principle, the reality is much more complicated, and so there is a large effort underway to understand how small changes to the structure, through the interchange of the metal ions, organic

species, and means of preparation, affect the ultimate magnetic and other properties of these materials.

4.1 Interpenetrating Lattices

One family of molecular magnets is based upon the structure of Prussian blue, $Fe_4^{III}[Fe^{II}(CN)_6]_3 \bullet 14H_2O$. In Prussian blue, there is significant spin delocalization from the Fe^{III} onto the bridging cyanides, leading to strong magnetic coupling through the Fe^{III}—C—N—Fe^{II}—N—C—Fe^{III} linkages, leading to a $T_C = 5.6$K [43, 44]. There has been a great deal of progress in varying the behavior of such materials by substitution of the metal ions, such that the magnetic properties of Prussian blues are understood sufficiently to allow rational design of their composition in search of desired properties.

One such substitution, which also opens up the numerous possibilities of organic chemistry, is to replace the low spin metal ion site with a spin bearing molecule. Diruthenium tetracarboxylate cations, $[Ru_2(O_2CR)_4]^+$ have $S = 3/2$ ground state with each Ru being pentacoordinate with the ability to coordinate an additional ligand necessary for building extended network structures (Fig. 4.1).

$[Ru_2(O_2CMe)_4]^+$ is the basis for forming a cubic 3-D network with metal hexacyanometallate(III), $[M(CN)_6]^{3-}$ (M = Co, Fe, Mn, Cr) species. $[Ru_2(O_2CMe)_4]_3[M^{III}(CN)_6]$ [M = Co, Fe, Cr] have a 3-D body-centered, interpenetrating network structure that magnetically orders at 2.1K and 33K for M = Fe and Cr, respectively [45, 46]. Unexpectedly, anomalous behavior in magnetic hysteresis, saturation magnetization, out-of-phase, $\chi''(T)$, AC

Figure 4.1: $[Ru_2(O_2CH)_4]$ (a) and $[Ru_2(O_2CMe)_4]$ (b) dimers. Purple atoms are Ru, red are O, black are C, and pink are H.

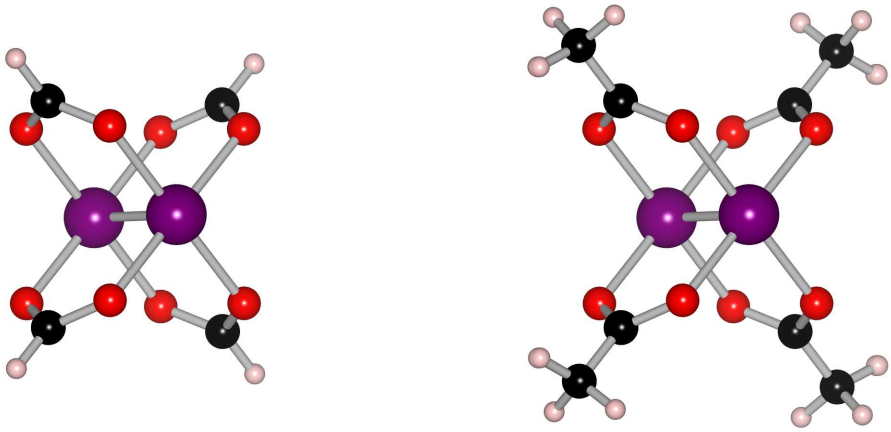

(a) (b)

susceptibility, and zero-field-cooled (ZFC) and field-cooled (FC) temperature-dependent magnetization data is observed for $[Ru_2(O_2CMe)_4]_3[Cr^{III}(CN)_6]$ [46]. Furthermore, under pressure T_C is enhanced with the loss of the anomalous constricted hysteresis [47]. These unexpected behaviors, as well as the magnetic phase diagram, are attributed to the presence of the interpenetrating lattices. To further understand the effect of the interpenetrating lattices, which only rarely lead to different physical properties, beside the obvious increase in density, additional examples of related magnetic materials possessing a second interpenetrating, body centered cubic lattice, $[Ru_2(O_2CH)_4]_3[M^{III}(CN)_6]$ (M = Fe, Co) were synthesized, as the smaller formate ion should accommodate the second interpenetrating lattice.

In a further attempt to understand these magnetostructural phenomena, additional examples of related materials possessing an interpenetrat-

ing, body centered cubic lattice were sought, and pentacyanometalates, $[M(CN)_5NO]^{n-}$, were identified for synthesis and study. Pentacyanometalate species, $[M(CN)_5NO]^{n-}$, have been incorporated in various structural environments. Systems analogous to Prussian Blue, with face centered cubic structure, have been observed [48, 49, 50, 51]. Some compounds containing $[M(CN)_5NO]^{n-}$ exhibit monoclinic unit cells [52, 53, 54]. Triclinic structures have also been observed [55], and even noninteracting materials, those with no binding interactions between ionic species, have been reported [56, 57, 58, 59]. In the non-cubic structural motifs that contain $[Fe(CN)_5NO]^{2-}$, the NO groups do not bridge two metal ions, and are always terminal suggesting that O is poorer Lewis based than N in accord with its greater electronegativity. While the cubic possibilities suggested make $[M(CN)_5NO]^{n-}$ a good candidate for developing the desired interpenetrated structures, as occurs for $[Cr(CN)_6]^{3-}$ [60], the wide array of possible structures indicate that other motifs may just as easily form.

4.1.1 $[Ru_2(O_2CH)_4]_3[M(CN)_6]$ (M = Fe, Co)

Sample Preparation

The synthesis of the targeted $[Ru_2(O_2CH)_4]_3[M^{III}(CN)_6]$ was carried out via the reaction of $[Ru_2(O_2CH)_4]Cl$ and $K_3[M^{III}(CN)_6]$ (M = Fe, Co) in aqueous solution. This route was successful for the quantitative formation of $[Ru_2(O_2CH)_4]_3[Co(CN)_6]$, which was analytically pure. IR absorption data provided strong preliminary evidence that the targeted material had, indeed, been achieved [60].

In contrast, the reaction of $[Ru_2(O_2CH)_4]Cl$ and $K_3[Fe(CN)_6]$ at room temperature resulted in the formation of a dark blue-green material. IR absorption measurements were consistent with those expected for $[Ru_2(O_2CH)_4]_3[Fe(CN)_6]$, although two unexpected absorptions were also present. These would seem to indicate the presence of an unknown decomposition product, which is also reflected in the elemental percentages that cannot be fit to the expected composition or other reasonable stoichiometries. Powder XRD data, however, is only consistent with the presence of a body center cubic (bcc) interpenetrating lattice ($a = 12.7071$ Å) attributed to $[Ru_2(O_2CH)_4]_3[Fe(CN)_6]$ (*vide infra*); hence, the decomposition product(s) is amorphous, in agreement with the broad anomalous IR signal [60].

Structure Determination and Refinement

The unit cells for $[Ru_2(O_2CH)_4]_3[M(CN)_6]$ (M = Fe, Co) were determined from the analysis of the X-ray powder diffraction data to be body centered cubic (bcc) with $a = 12.6621(3)$ Å (M = Co) and 12.7071(3) Å (M = Fe). The structures were modeled after that of $[Ru_2(O_2CMe)_4]_3[Cr(CN)_6]$ ($a = 12.376$ Å), with subsequent Rietveld refinement confirming them to be isostructural. The structure of $[Ru_2(O_2CH)_4]_3[M(CN_6]$ is characterized by a cubic network in which the M site is octahedrally coordinated by cyanides, which in turn bridge to the $Ru_2(O_2CH)_4$ units (Fig. 4.2). The overall structure is body centered cubic due to the inclusion of a second, interpenetrating such lattice.

Although $[Ru_2(O_2CH)_4]_3[M(CN)_6]$ has the same structure as $[Ru_2(O_2CMe)_4]_3[M(CN)_6]$, significantly shorter unit cell parameters of $a = 12.6621$ Å (M = Co) and 12.7071 Å (M = Fe) is observed for

Figure 4.2: Structure of $[Ru_2(O_2CH)_4]_3[M(CN_6]$ with only a single lattice shown (a) and including the second, interpenetrating lattice (b).

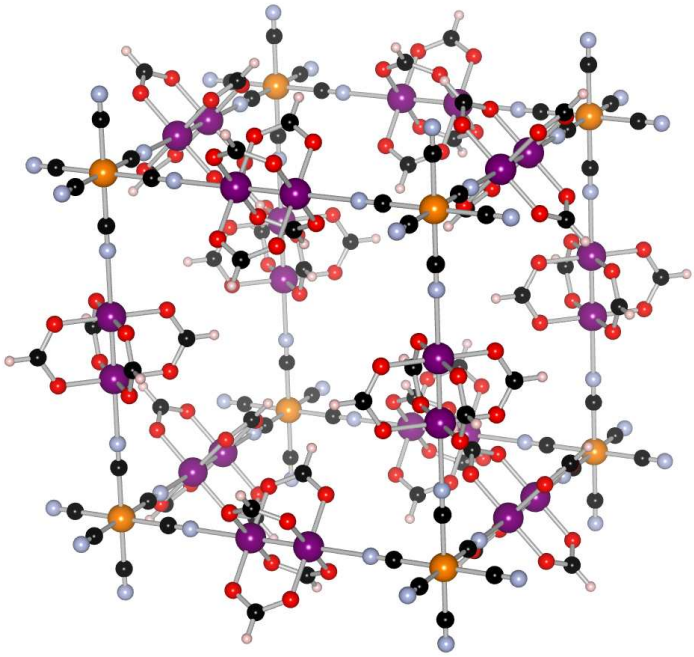

(a)

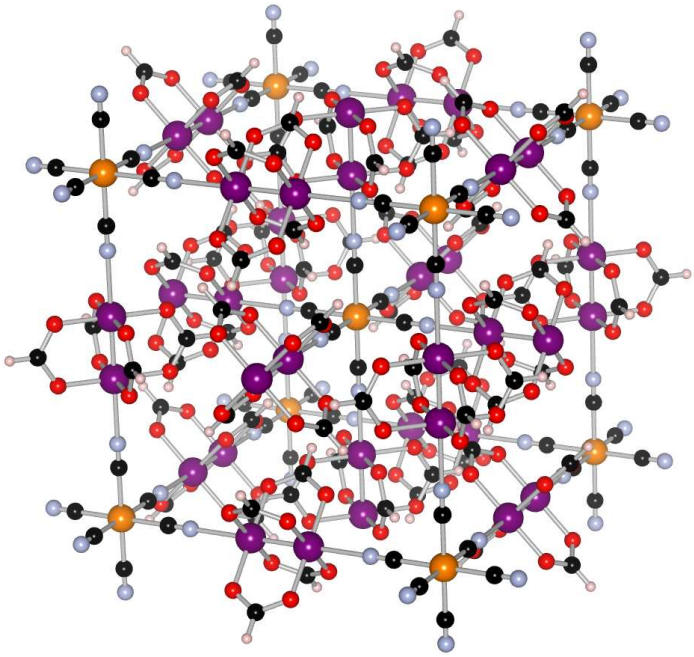

(b)

$[Ru_2(O_2CH)_4]_3[M(CN)_6]$, compared to a = 13.10 Å and 13.30 Å observed for $[Ru_2(O_2CMe)_4]_3[M(CN)_6]$, M = Co, Fe, respectively. Since the Ru-Ru bond distances for the formate and acetate species are both from 2.28 Å to 2.25 Å, the shorter a values suggest shorter M-N distances for the formate and thus stronger coupling than that of the acetate analogue, presumably leading to the higher observed values of T_C.

Figure 4.3: Rietveld refinement of $[Ru_2(O_2CH)_4]_3[Fe(CN)_6]$. Blue dots are the measured data, the red line is the calculated fit from the refined structure, and the black line below is the difference between the two. Allowed peak positions are indicated by the tick marks.

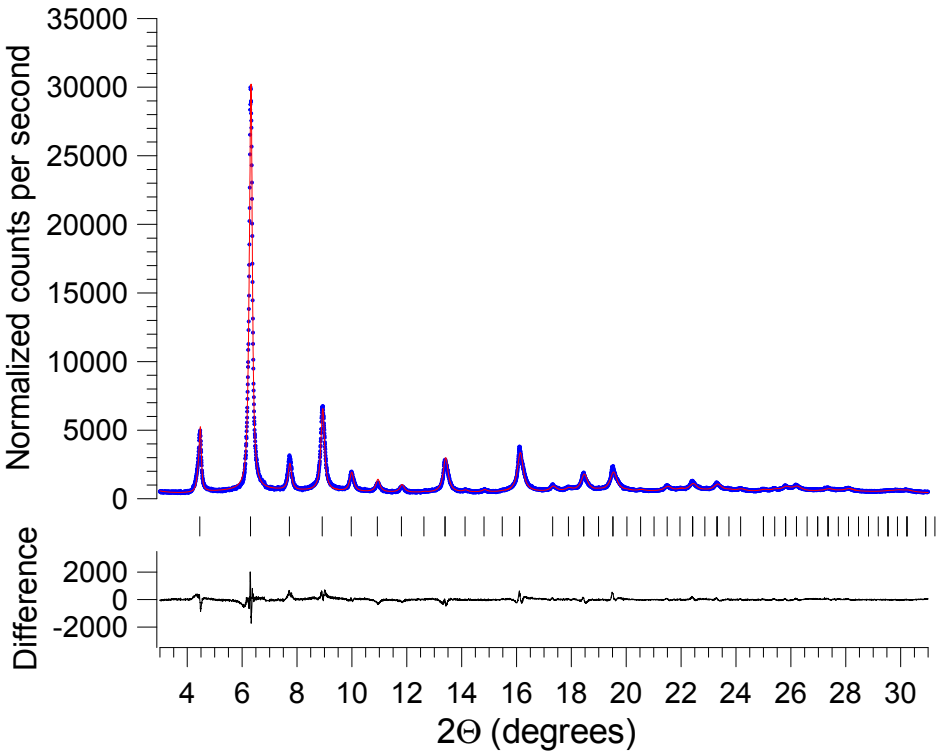

Figure 4.4: Rietveld refinement of $[Ru_2(O_2CH)_4]_3[Co(CN)_6]$. Blue dots are the measured data, the red line is the calculated fit from the refined structure, and the black line below is the difference between the two. Allowed peak positions are indicated by the tick marks.

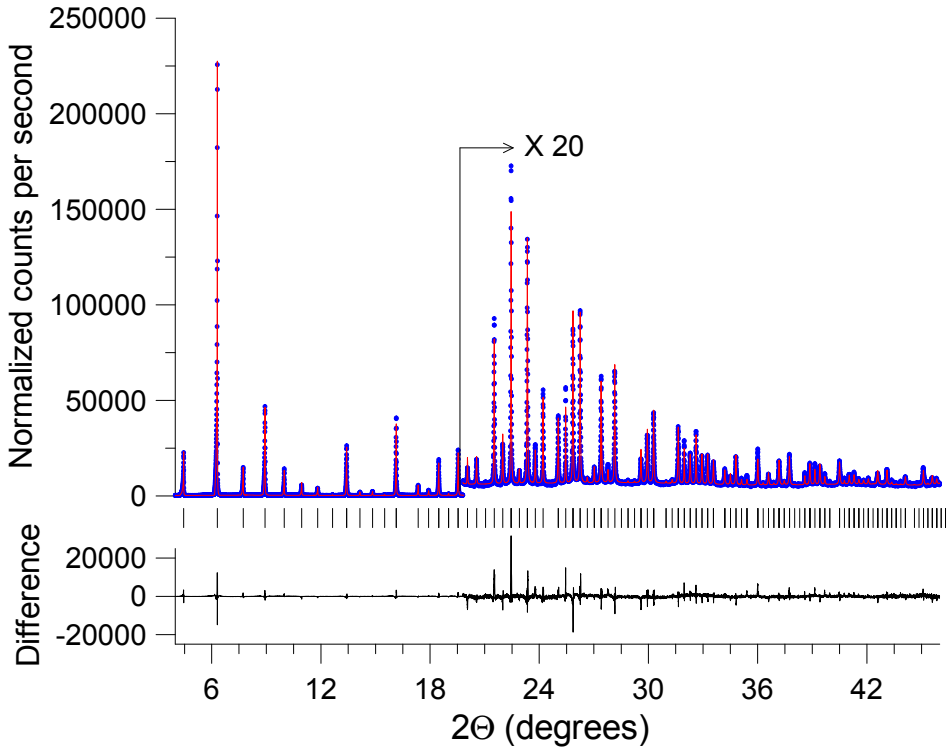

4.1.2 $H_x[Ru_2^{II/III}(O_2CMe)_4]_{3-x}[Cr(CN)_5NO]$

Crystal Preparation

$H_x[Ru_2^{II/III}(O_2CMe)_4]_{3-x}[Cr(CN)_5NO]$ was prepared via the aqueous reaction of $[Ru_2(O_2CMe)_4]Cl$ and $K_3[Cr(CN)_5NO]$. $K_3[Cr(CN)_5NO]$ (28.02 mg, 0.085 mmol) dissolved in $\sim$ 10 mL water was added dropwise to a stirring solution of $[Ru_2(O_2CMe)_4]Cl$ (100.6 mg, 0.212 mmol) in 40 mL water. The color changed from orange to reddish brown after the first few drops added and the mixture turned cloudy after the next several drops added. After $\sim$ 10 min, the solids were collected via centrifugation, washed with H_2O, and dried overnight in a vacuum desiccator with Drierite and P_2O_5. The product turned from rust-colored to brownish black as it dried.

Structure Solution

The powder X-ray diffraction pattern of $H_x[Ru_2^{II/III}(O_2CMe)_4]_{3-x}[Cr(CN)_5NO]$ (Figure 4.5) can be fit to a body centered cubic structure with $a = 13.2509(2)$ Å, a value that is 0.05 Å shorter than reported for $[Ru_2(O_2CMe)_4]_3[Cr(CN)_6]$. Both $H_x[Ru_2^{II/III}(O_2CMe)_4]_{3-x}[Cr(CN)_5NO]$ and the previously reported hexacyano analog have the D_{4h} $[Ru_2(O_2CMe)_4]^+$ paddlewheel cation with its two Ru ions bridged by the oxygens of 4 acetate ligands and a Ru-Ru bond order of 2.5. $H_x[Ru_2^{II/III}(O_2CMe)_4]_{3-x}[Cr(CN)_5NO]$ differs as it has one cyanide per Cr replaced by NO; the cubic symmetry implies that this substitution is random. Each $[Cr(CN)_5NO]^{3-}$ binds to six Ru_2 species in the position axial to the Ru-Ru bond forming a simple cubic network, and there is a second interpenetrating lattice.

Refinement of the structure, however, was fraught with difficulties suggesting that the actual structure is more complicated than the predicted, simple structure. Based on the elemental percentages and fit to the magnetic data, some of the $[Ru_2(O_2CMe)_4]^+$ cations are missing randomly from the structure and evidently replaced by protons, such that the stoichiometry is $H_{0.2}[Ru_2(O_2CMe)_4]_{2.8}[Cr(CN)_5NO]$. Allowing the occupancy of the $[Ru_2(O_2CMe)_4]^+$ to refine freely results in an occupancy of 94%, in good agreement with 93% predicted for this stoichiometry. The presence of water, which varies from sample-to-sample, and is not present for $[Ru_2(O_2CMe)_4]_3[Cr(CN)_6]$ was not found in any significant amount in the sample studied by synchrotron X-ray diffraction. Why this material has a defect structure, and $[Ru_2(O_2CMe)_4]_3[M(CN)_6]$ does not, is not understood at present. Overall, the structure of $H_x[Ru_2^{II/III}(O_2CMe)_4]_{3-x}[Cr(CN)_5NO]$ is nominally the same as for $[Ru_2(O_2CMe)_4]_3[Cr(CN)_6]$, except one cyanide per Cr is randomly replaced by NO, and 6.7% of the $[Ru_2(O_2CMe)_4]^+$ cations are randomly vacant, as illustrated in Figure 4.6.

Figure 4.5: Rietveld refinement of $H_{0.2}[Ru_2(O_2CMe)_4]_{2.8}[Cr(CN)_5NO]$. Blue dots are the measured data, the red line is the calculated fit from the refined structure, and the black line below is the difference between the two. Allowed peak positions are indicated by the tick marks.

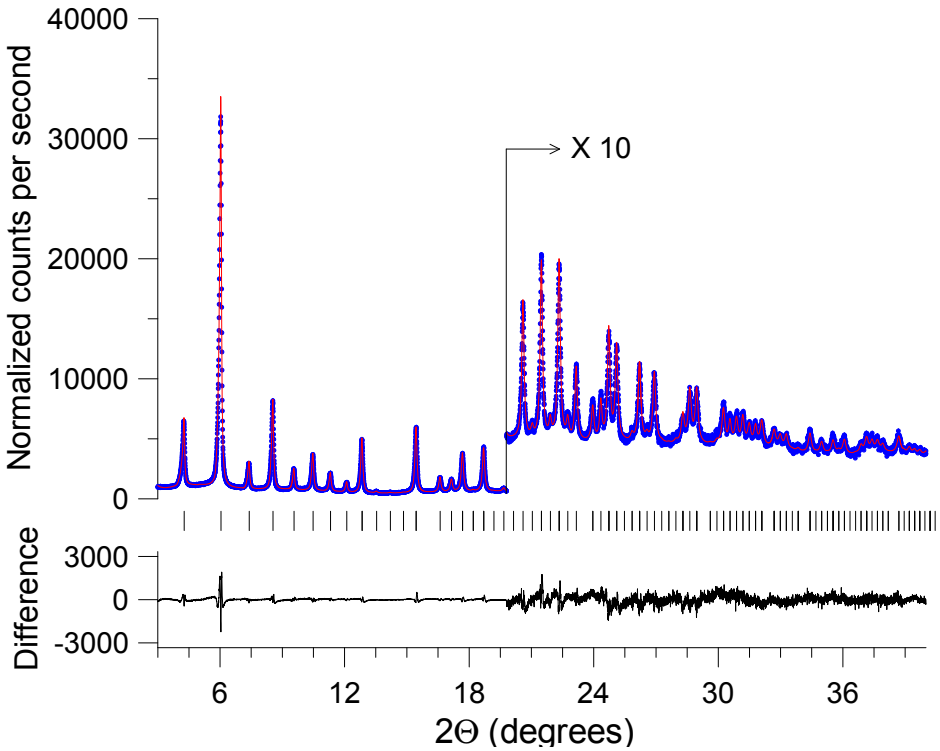

Figure 4.6: Schematic layout of the structure of $H_{0.2}[Ru_2(O_2CMe)_4]_{2.8}[Cr(CN)_5NO]$ showing the partial occupancies.

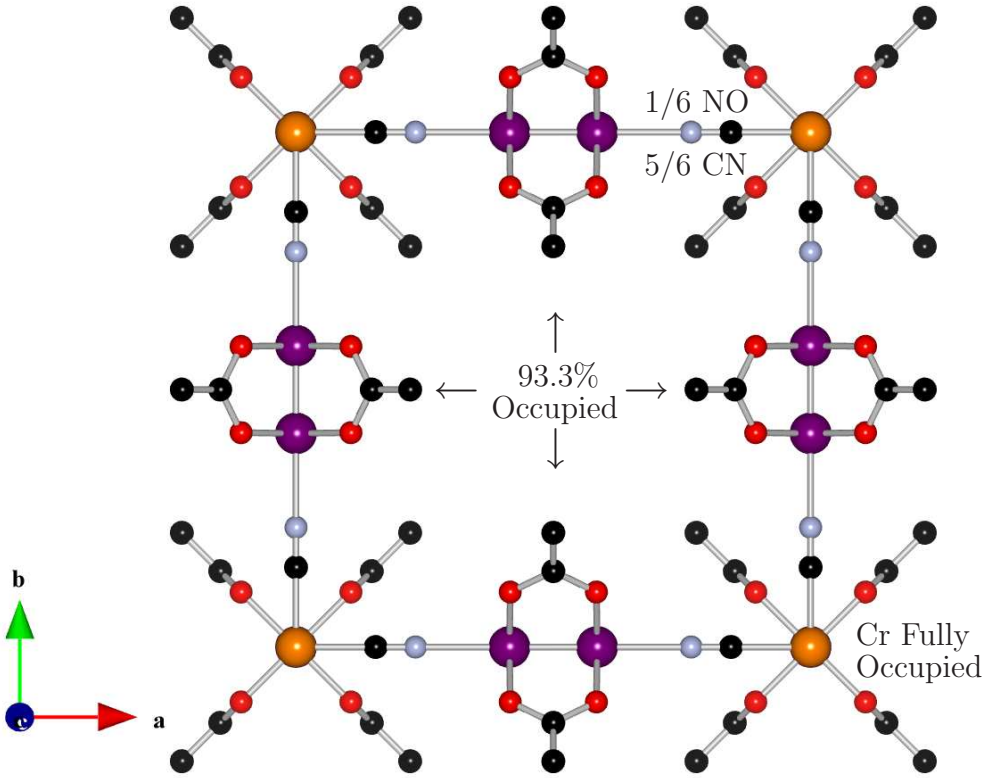

4.1.3 $[Ru_2^{II/III}(O_2CMe)_4]_2[Fe(CN)_5NO]$

Crystal Preparation

$[Ru_2^{II/III}(O_2CMe)_4]_2[Fe(CN)_5NO]$ was prepared via aqueous reaction of $[Ru_2(O_2CMe)_4]Cl$ and $Na_2[Fe(CN)_5NO]$. $Na_2[Fe(CN)_5NO]$ (32.41, 0.116 mmol) dissolved in $\sim$ 12 mL water was added dropwise to a stirring solution of $[Ru_2(O_2CMe)_4]Cl$ (100.4 mg, 0.212 mmol) in $\sim$ 45 mL H_2O. The reaction mixture lightened in color with formation of an orange precipitate occurring upon addition of the first few drops of anion. After 5 min, the product was isolated via vacuum filtration on a glass frit and washed with H_2O. The sample was dried by pulling air over the frit until the solids were free moving powders.

Structure Solution

The unit cell of $[Ru_2^{II/III}(O_2CMe)_4]_2[Fe(CN)_5NO]$ was found to be similar to $H_x[Ru_2^{II/III}(O_2CMe)_4]_{3-x}[Cr(CN)_5NO]$, quasi-bcc with a slight tetragonal distortion, resulting in lattice parameters of $a = 13.0186(1)$ Å and $c = 13.0699(2)$ Å. Surprisingly, the quasi-bcc nature of the diffraction pattern seems to suggest the same basic structure as that found for $H_x[Ru_2^{II/III}(O_2CMe)_4]_{3-x}[Cr(CN)_5NO]$, with the interpenetrating lattices, although such a structure would seem incompatible with the intended 2:1 ratio of $[Ru_2(O_2CMe)_4]$ to $[Fe(CN)_5NO]$ expected for $[Fe(CN)_5NO]^{2-}$. The distortion creates at least two distinct sites for the Ru dimer moiety. The complete removal of any particular $[Ru_2(O_2CMe)_4]^+$ cation from the prototypical structure, in an attempt to regain the correct stoichiometry, would result in an ordered vacancy, which would produce large intensities for the

experimentally unobserved reflections. This would indicate that the vacancies are primarily randomly distributed. Refinement of the X-ray data leads to different $[Ru_2(O_2CMe)_4]^+$ occupancies in the *ab* plane and along the *c*-axis, as shown in Figure 4.7. The refinements lead to a stoichiometry of $[Ru_2(O_2CMe)_4]_{2.2}[Fe(CN)_5NO]$ instead of the charge compensated 2:1 ratio, with some disordered water in the vacancies. We have no direct crystallographic identification of the orientation of the substitution of NO groups for CN, but because of their lower affinity to the Ru dimer, we expect that they are oriented along the *c*-axis, towards the less occupied cation sites.

Figure 4.7: Schematic layout of the structure of $[Ru_2(O_2CMe)_4]_2[Fe(CN)_5NO]$ showing the partial occupancies.

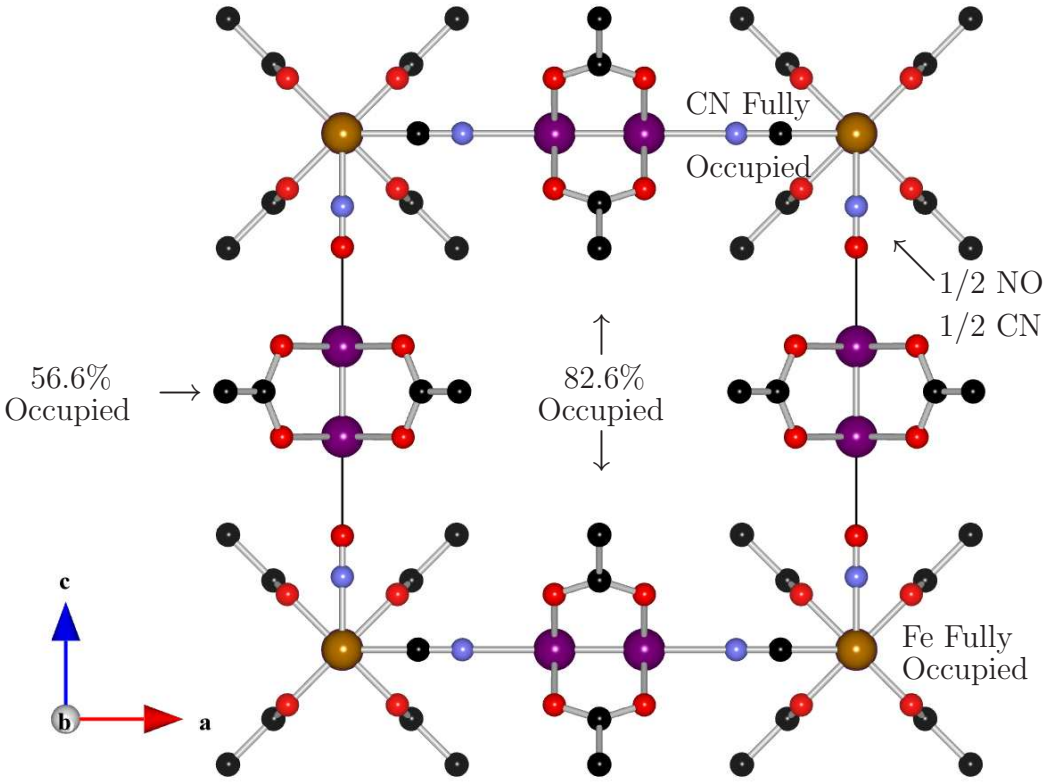

Figure 4.8: Rietveld refinement of $[Ru_2(O_2CMe)_4]_{2.2}[Fe(CN)_5NO]$. Blue dots are the measured data, the red line is the calculated fit from the refined structure, and the black line below is the difference between the two. Allowed peak positions are indicated by the tick marks.

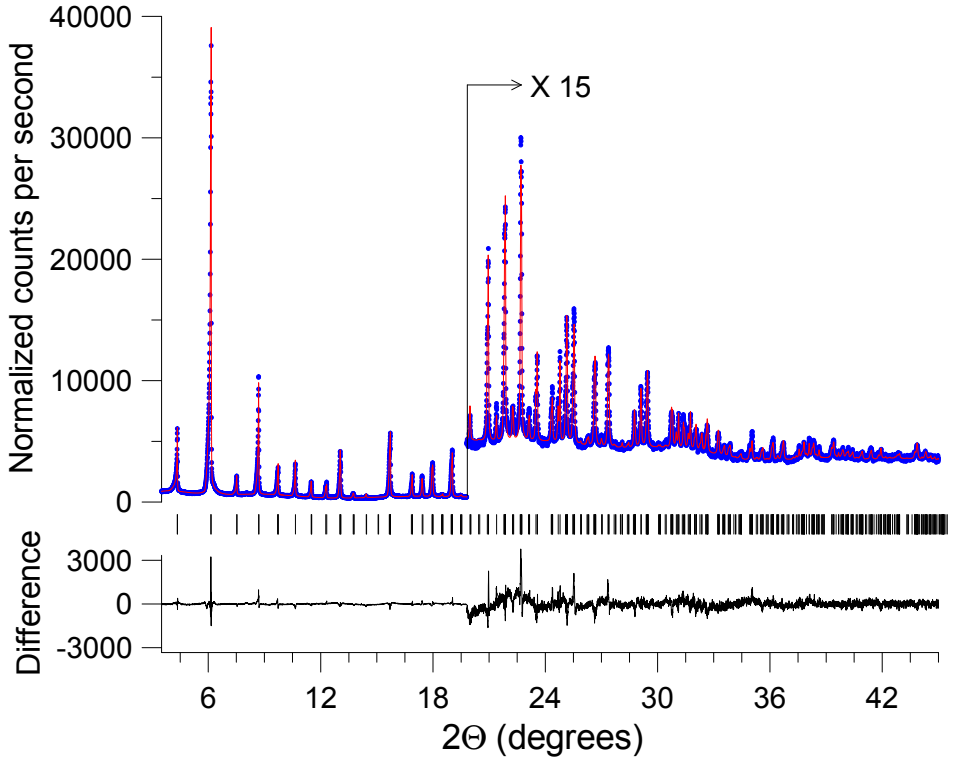

It is entirely unexpected that $[Ru_2^{II/III}(O_2CMe)_4]_2[Fe(CN)_5NO]$ would have a structure so similar to the Cr analog, in view of previously reported materials containing $[Fe(CN)_5NO]^{2-}$ having nonbridging NO groups. Most structures involving $[Fe(CN)_5NO]^{2-}$ have monoclinic unit cells, including $Fe[Fe(CN)_5NO](H_2O)_3$, however, $Ni[Fe(CN)_5NO](H_2O)_{5.3}$ has a face center cubic structure. Crystallographic measurements only reveal the average structure and the present data are not sufficiently sensitive to the difference between CN and NO, so the extent to which NO groups are oriented along the c axis vs. the ab plane is unknown. It is clear that there must be both Fe-CN$\cdots$ON-Fe and Fe-CN-RuRu-ON-Fe linkages in order to support the approximate 2:1 ratio of dimers to vacancies. Although this material has a tetragonal unit cell, the difference between a and c unit cell lengths is quite small ($\sim 0.4\%$), also indicating random NO environments mentioned above, as a perfectly localized material would have a larger difference and a completely randomized material would be cubic. This nearly cubic structure was further established with scanning electron microscopic (SEM) analysis, which revealed the cube shaped particles, Figure 4.9. There must be a very strong preference for the Ru paddlewheel dimers to pack as shown in Figure 4.2 in order for the material to adopt this pseudo-bcc structure with such a large number of vacancies.

Figure 4.9: Image of cube shaped particles of $[Ru_2^{II/III}(O_2CMe)_4]_2[Fe(CN)_5NO]$ collected by scanning electron microscopy. Figure taken from [61].

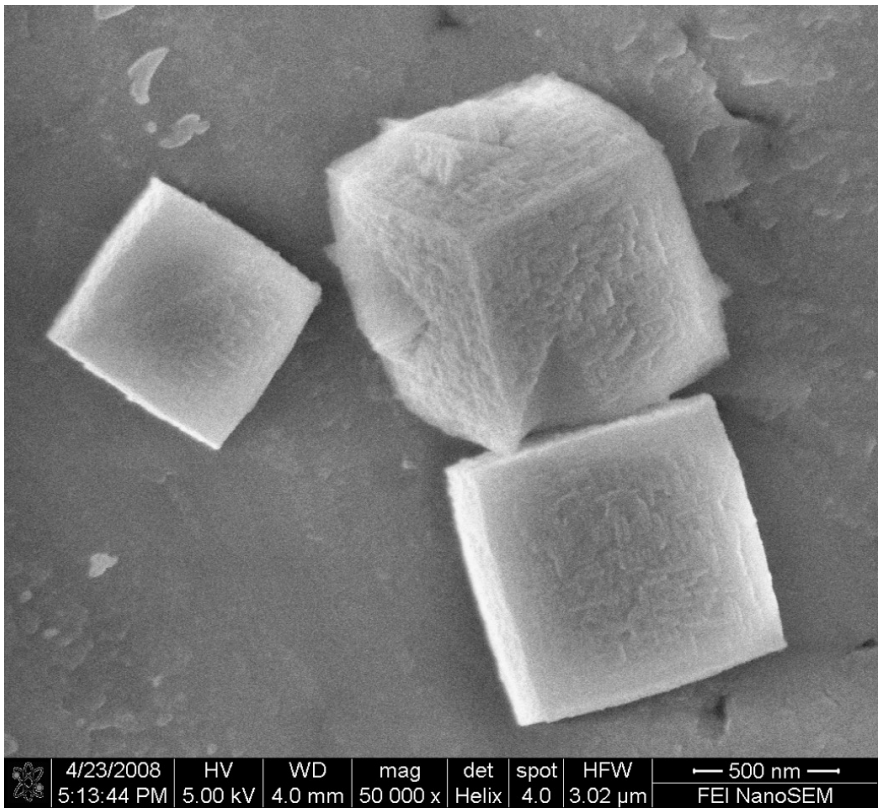

4.2 TCNE Based Examples

The most intriguing examples of organic-based magnets are ferrimagnetic semiconductors such as V[TCNE]$_x$ (TCNE = tetracyanoethylene, $C_2(CN)_4$; $x \sim 2$) which is magnetically ordered above room temperature ($T_C \sim 400$K) [62]. Its valence and conduction bands are spin polarized [63]; together with the powerful synthetic methodologies of organic chemistry [64, 65, 66], this suggests exciting applications, *e. g.*, combining optics and spintronics [67]. Several other room temperature magnets, all containing vanadium, have been synthesized, but curiously, they are all amorphous, making information on their mechanism and a rational development path forward difficult. Attempts to synthesize analogous materials from different transition metals have primarily resulted in 2-D magnetic structures with significantly lower T_C [68, 69]. To date, the only exception to this has been $Mn^{II}(TCNE)_{3/2}(I_3)_{1/2}$, which exhibits 3-D magnetic ordering as well as a greatly increased T_C over the 2-D ordered material $Mn^{II}[TCNE][C_4(CN)_8]_{1/2}$ [70].

Structurally characterized magnets based on transition metals and TCNE fall into several groups [68, 71]. Two families based on buckled layers of μ_4-$[TCNE]^{\bullet-}$ bonded to four Fe^{II} ions have been described. In both cases, there is an antiferromagnetic direct exchange coupling within the layers between the $S = 2$ Fe^{II} and $S = 1/2$ μ_4-$[TCNE]^{\bullet-}$ radical ions, leading to ferrimagnetic order. $Fe[TCNE][C_4(CN)_8]_{1/2}$ ($T_C \sim 100$K) was originally described as $Fe[TCNE]_2$ [72], but the current designation is more useful since adjacent Fe[TCNE] layers are connected by diamagnetic $C_4(CN)_8^{2-}$. $Fe[TCNE][NCMe]_2[FeCl_4]$ has similar Fe[TCNE] layers, but there are no cova-

lent bonds between layers; rather the intervening space is occupied by two trans terminal acetonitrile molecules bonded to the Fe^{II} ions, and by interstitial $FeCl_4^-$ counterions. Both are ferrimagnets, with the spins on the metal ions and the TCNE radical ions oppositely directed in the ordered state. They have comparable saturation moments of $\sim 20,000$ emu/mol, but other differences between their magnetic behavior have been a puzzle. While $Fe[TCNE][NCMe]_2[FeCl_4]$ shows typical properties of ferromagnets, such as hysteresis and a significant out-of-phase AC susceptibility near the transition, $Fe[TCNE][C_4(CN)_8]_{1/2}$ orders without showing either effect. This work offers a framework for understanding these differences, as well as the behavior of other previously studied magnets.

4.2.1 Sample Preparation

The reaction of TCNE and $MnI_2(THF)_3$ led to $Mn^{II}(TCNE)_{3/2}(I_3)_{1/2}$ (also containing approximately 1/2 equivalent of THF), a new structure type and a new family of organic based magnets with M:TCNE in a 2:3 ratio. Sharp 2231- and 2189 cm^{-1} ν_{CN} IR absorptions indicate the presence of μ_4-$[TCNE]^{\bullet-}$ as they are shifted 10 ± 1 cm^{-1} to higher energy than that observed for μ_4-$[TCNE]^{\bullet-}$ present in $Fe[TCNE][NCMe]_2[FeCl_4]$. The reaction of TCNE with $Mn(NCS)_2(OCMe_2)_2$ [73] produced $Mn[TCNE][C_4(CN)_8]_{1/2}\bullet zCH_2Cl_2$, which preliminary X-ray diffraction confirmed is isostructural to the previously known Fe compound [71]. $Mn[TCNE][C_4(CN)_8]_{1/2}$ has broader ν_{CN} absorptions at 2225- and 2173 cm^{-1} that are in accord with 2221- and 2172 cm^{-1} reported for $Fe[TCNE][C_4(CN)_8]_{1/2}$.

4.2.2 Structure Solution

Single crystals did not form of either phase, but crystal structures could be obtained from high resolution powder diffraction patterns collected at beamline X16C at the National Synchrotron Light Source at ambient temperature, Figures 4.10 and 4.11. Prior to structure solution, the reaction product of TCNE and $MnI_2(THF)_3$ was of substantially unknown composition, therefor the structure was attacked by simulated annealing, hypothesizing various amounts of Mn and TCNE present. The buckled layers similar to those in $Fe[TCNE][C_4(CN)_8]_{1/2}$ were quickly recognized, as was the I_3^- counterion, although it was not immediately identified as such. Further simulated annealing trials, with the layers and iodine held fixed and various amounts of TCNE and free atoms allowed to refine, suggested the presence of an additional TCNE molecule bridging the buckled layers. Charge balance considerations of the final structure led to the ultimate identification of the I_3^- counterion (the refinement actually showed less than full occupancy of the outer iodine atoms, so the anion sites are evidently mixed I_3^- ($\sim 95\%$) and I^- ($\sim 5\%$)), confirmed with the observation of the strong Raman absorption at 110 cm^{-1} [74, 75]. Approximately 1/2 equivalent of THF was known to be present by thermogravimetric mass spectrometry at ambient temperature. The crystallographic analysis confirmed approximately that density of highly disordered solvent in the network channels (Fig. 4.12). The structure for $Mn[TCNE][C_4(CN)_8]_{1/2}$ was modelled after that of the Fe analogue [71] and confirmed to be isostructural (Fig. 4.13). The geometry of the μ_4-$[C_4(CN)_8]^{2-}$ is comparable to previously described phases [76, 77]. Following structure determination, both

structures were Rietveld refined [78].

Figure 4.10: Rietveld refinement of Mn[TCNE][$C_4(CN)_8$]$_{1/2}$. Blue dots are the measured data, the red line is the calculated fit from the refined structure, and the black line below is the difference between the two. Allowed peak positions are indicated by the tick marks.

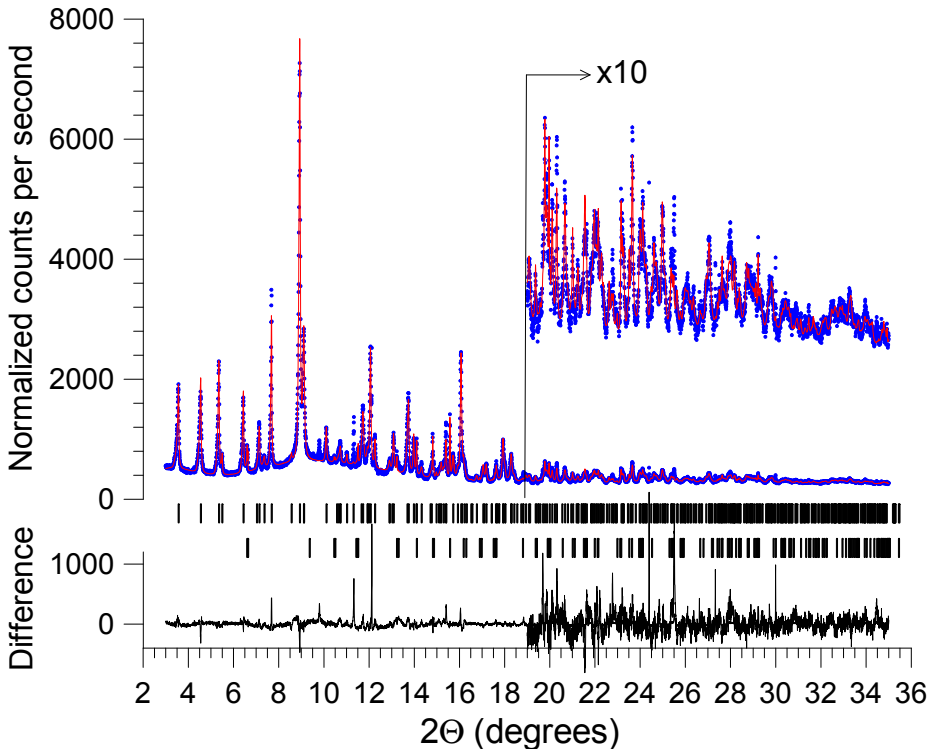

Figure 4.11: Rietveld refinement of $Mn(TCNE)_{3/2}(I_3)_{1/2}$. Blue dots are the measured data, the red line is the calculated fit from the refined structure, and the black line below is the difference between the two. Allowed peak positions are indicated by the tick marks.

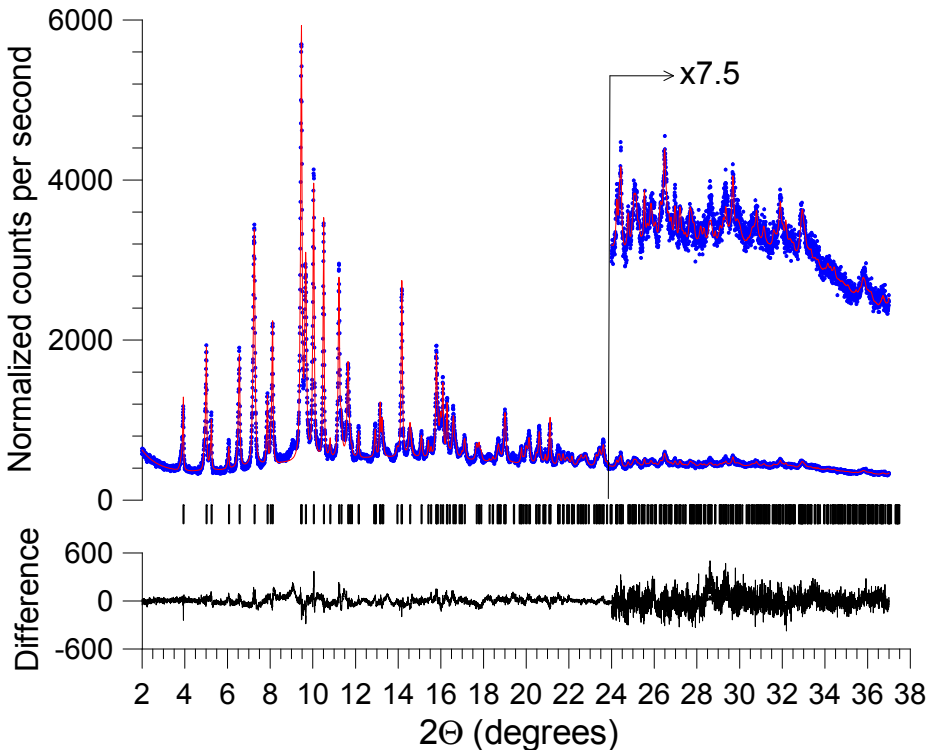

Figure 4.12: The structure of $Mn(TCNE)_{3/2}(I_3)_{1/2}$ including the tri-iodide counterion and the disordered solvent shown as contours of charge density.

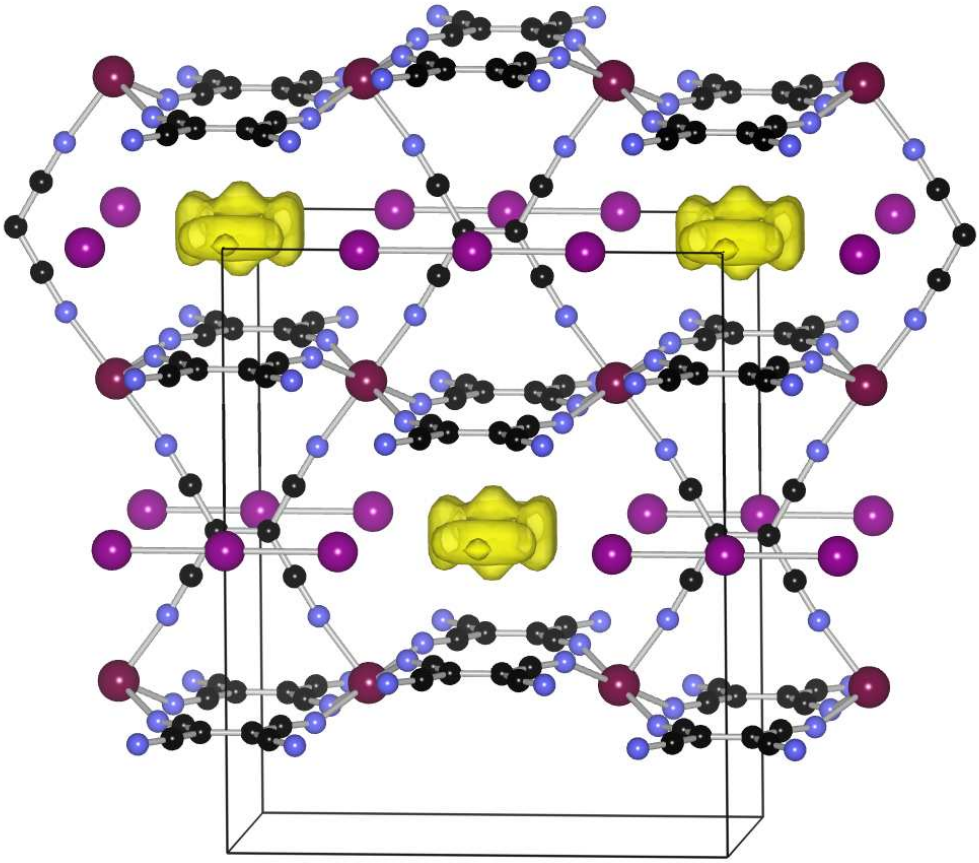

Figure 4.13: The structure of Mn[TCNE][$C_4(CN)_8$]$_{1/2}$ with disordered solvent shown as contours of charge density. The half-colored Carbon atoms indicate half occupancy as the $C_4(CN)_8$ has a configurational disorder.

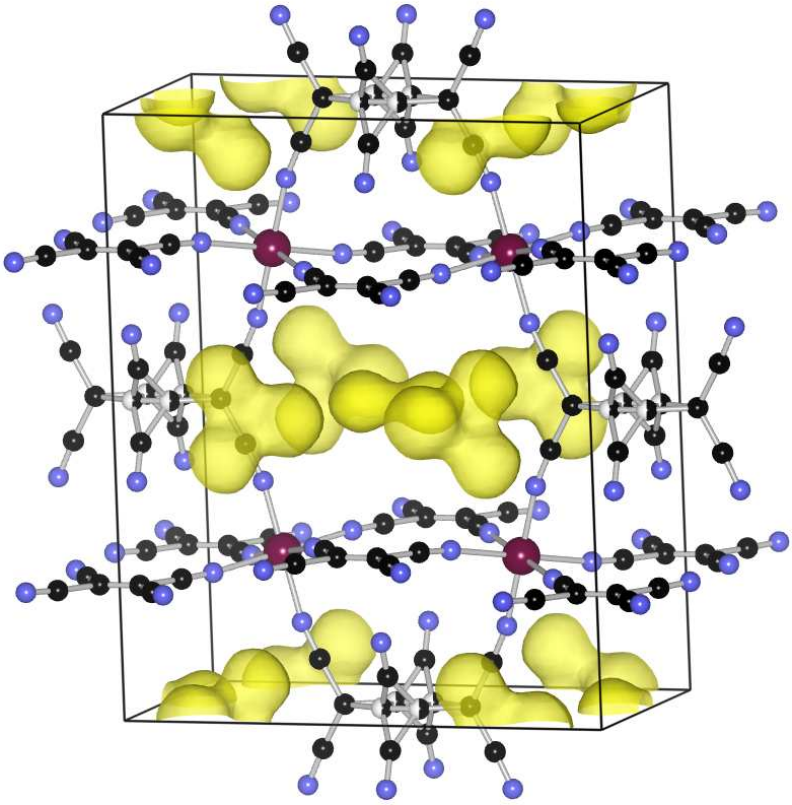

While the structures of $Mn(TCNE)_{3/2}(I_3)_{1/2}$ and $Mn[TCNE][C_4(CN)_8]_{1/2}$ are based on layers of μ_4-$[TCNE]^{\bullet-}$ bound to four Mn^{II} ions, the structure for $Mn(TCNE)_{3/2}(I_3)_{1/2}$ is distinctly different from that reported for other organic-based magnets, and represents a new structural type. The complex motif possesses two different μ_4-$[TCNE]^{\bullet-}$ moieties, both magnetically active. That 3-D network therefor has the composition of $Mn[TCNE]_{3/2}$ with a total charge of $+1/2$, compensated by the $(I_3^-)_{1/2}$. In both structures, MnN_6 octahedra are distorted and canted due to the geometrical considerations of forming an extended layer structure, leading to a wrinkled form of the extended $Mn^{II}[TCNE]^{\bullet-}$ planes, similar to related 2-D Fe:TCNE materials [68, 71]. A comparison of the local geometries of these materials is given in Table 4.1.

4.2.3 Discussion of Magnetic Behavior

The magnetic data for $Mn(TCNE)_{3/2}(I_3)_{1/2}$ exhibits the familiar behavior of a ferro- or ferrimagnet: Curie-Weiss susceptibility above the ordering temperature, bifurcation of the field-cooled and zero-field-cooled magnetization below the ordering temperature, significant out of phase AC susceptibility χ'' peaking at the ordering temperature, and a hysteresis loop with moderately large coercive field of 500 Oe. All measures of the ordering temperature coincide at 171 ± 1K. The saturated moment of $21,800$ emuOe/mol is somewhat in excess of $19,500$ emuOe/mol expected for antiferromagnetically ordered $S = 5/2$ Mn^{II} and 3/2 equivalent of $S = 1/2[TCNE]^{\bullet-}$, shown schematically in Figure 4.14. The difference is most likely due to the anisotropic environment of the Mn^{II} ion, resulting in a g factor slightly greater than 2.

Table 4.1: Comparison of the local bonding geometries of $Mn(TCNE)_{3/2}(I_3)_{1/2}$ (**1**), $Mn[TCNE][C_4(CN)_8]_{1/2}$ (**2**), $Fe(TCNE)[C_4(CN)_8]_{1/2}$ (**3**) [71], and $[Fe(TCNE)(NCMe)_2][FeCl_4]$ (**4**) [68].

	1 - In Plane	**1** - Between Plane	**2**	**3**	**4**
M-N bond (Å)	2.2091(72)	2.177(11)	2.092(11)	2.184	2.145
N-C bond (Å)	1.219(10)	1.219(17)	1.081(10)	1.139	1.087
CC-CC bond (Å)	1.3705(99)	1.371(44)	1.224(21)	1.348	1.288
NC-C bond (Å)	1.371(29)	1.371(17)	1.493(11)	1.423	1.519
N-M-N angles	95.91(38)-84.09(38)	91.73(21)-88.27(21)	91.08(35)-88.92(35)	90.63-89.37	90.48-88.85
C-N-M angle	156.51(62)	174.34(88)	170.70(55)	173.18	175.37
C-C-N angle	165.17(73)	178.58(45)	175.54(62)	169.77	169.83

Figure 4.14: View of the structure of the 3-D covalent network structure of $Mn^{II}(TCNE)_{3/2}(I_3)_{1/2}$ showing the two different $\mu_4-(TCNE)^{\bullet-}$, but excluding the I_3^- anion, and the disordered solvent that reside in channels parallel to the c-axis. Arrows indicate the relative spin directions.

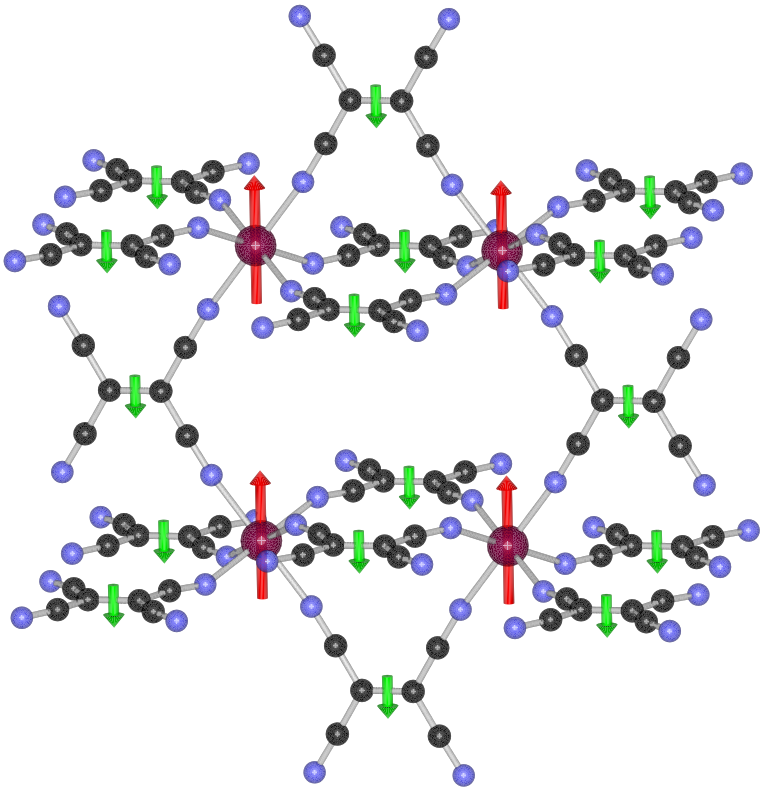

The magnetic behavior for $Mn[TCNE][C_4(CN)_8]_{1/2}$ is different from that of $Mn(TCNE)_{3/2}(I_3)_{1/2}$ in several important respects. The magnetic susceptibility at $T > 120$K extrapolates to a phase transition at $\sim$ 90K, but the susceptibility in the ordered phase shows no divergence and is less than that of $Mn(TCNE)_{3/2}(I_3)_{1/2}$ by a factor of ~ 10. The only signature of a magnetic phase transition is the hump in magnetization and susceptibility in the vicinity of $\sim$ 70K, a shape characteristic of antiferromagnetic ordering. There is no bifurcation of FC vs. ZFC magnetization at any temperature, and again, the magnetization in applied field is much smaller than $Mn(TCNE)_{3/2}(I_3)_{1/2}$ exhibited. There is essentially no detectable signal of χ''. There does exist a very small magnetic hysteresis, evident as a remnant magnetization of ~ 4 emuOe/mol, but it is likely that this is not intrinsic to $Mn[TCNE][C_4(CN)_8]_{1/2}$. This evidently implies that each $Mn^{II}[TCNE]^{\bullet -}$ sheet orders as a ferrimagnet at $\sim$ 70K, but that adjacent sheets have oppositely directed moments (Fig. 4.15). Since the ordered phase has no net magnetization, the susceptibility does not diverge at any temperature. The origin of the antiferromagnetic coupling between adjacent sheets is not obvious, as they are joined by diamagnetic $C_4(CN)_8^{2-}$ molecular ions, meaning that any such coupling must be extremely weak. In an applied field, an isotropic antiferromagnet has transverse susceptibility $\chi = \frac{N_A g^2 \mu_B^2}{4z|J|}$. Working from a value of ~ 1 emu/mol from the magnetization suggests $J/k_B \sim 0.2$K. Such a small energy has a negligible influence on the ordering transition within the sheets at 70K, however, when multiplied by the number of spins within each ordered sheet, it becomes very significant indeed, leading to the overall antiferromagnetic alignment. Thus, the hump observed in the magnetization and susceptibility is the signature of

the 2-D ordering within layers.

The structures determined above form the basis for understanding the observed magnetic data. If we consider the mean field theory of a magnetic system having two or more sublattices [79], the magnetic energy of a spin system is

$$\mathscr{H}_{\text{magnetic}} = \sum_n (-g_n \mu_B \vec{S_n} \cdot \vec{H_0}) - 2 \sum_{n \neq m} J_{nm} \vec{S_n} \cdot \vec{S_m}, \tag{4.1}$$

where the sums run over individual spins. In the mean field approximation, with all spins aligned parallel or antiparallel to one chosen direction, each sublattice is regarded as having an average magnetization $M_i = N_i \mu_i \sigma_i$, where N_i is the number of spins in the i^{th} sublattice, μ_i is the magnetic moment of each ion, and σ_i is the reduced sublattice magnetization ($0 \leq \sigma_i \leq 1$). $\mu_i = g_i S_i \mu_b$, the product of the ion's g factor, spin, and the Bohr magneton, (9.27×10^{-21} erg/G). Then the exchange energy acting on each spin in the i^{th} sublattice is $-2 \sum_j z_{ij} J_{ij} S_i S_j \sigma_i \sigma_j$, where the sum runs over sublattices and z_{ij} is the number of j neighbors to each i spin. The i^{th} spin system is therefore in an effective field

$$H_i = \pm H_0 - 2 \sum_j z_{ij} J_{ij} \sigma_j S_j / \mu_i = \pm H_0 - \sum_j \gamma_{ij} M_j, \tag{4.2}$$

where the coupling constant $\gamma_{ij} = 2 z_{ij} J_{ij} S_i S_j / (\mu_i \mu_j N_i)$. The resulting magnetization of the i^{th} sublattice is

$$M_i = N_i \mu_i B_{S_i} (\mu_i H_i / k_B T), \tag{4.3}$$

Figure 4.15: View of the structure of $Mn(TCNE)[C_4(CN)_8]_{1/2}$ possessing corrugated layers of $\mu_4-(TCNE)^{\bullet-}$ bound to four Mn^{II} sites that are connected by $\mu_4-[C_4(CN)_8]^{2-}$ with disordered solvent which resides in the channels removed for clarity. Arrows indicate the relative spin directions.

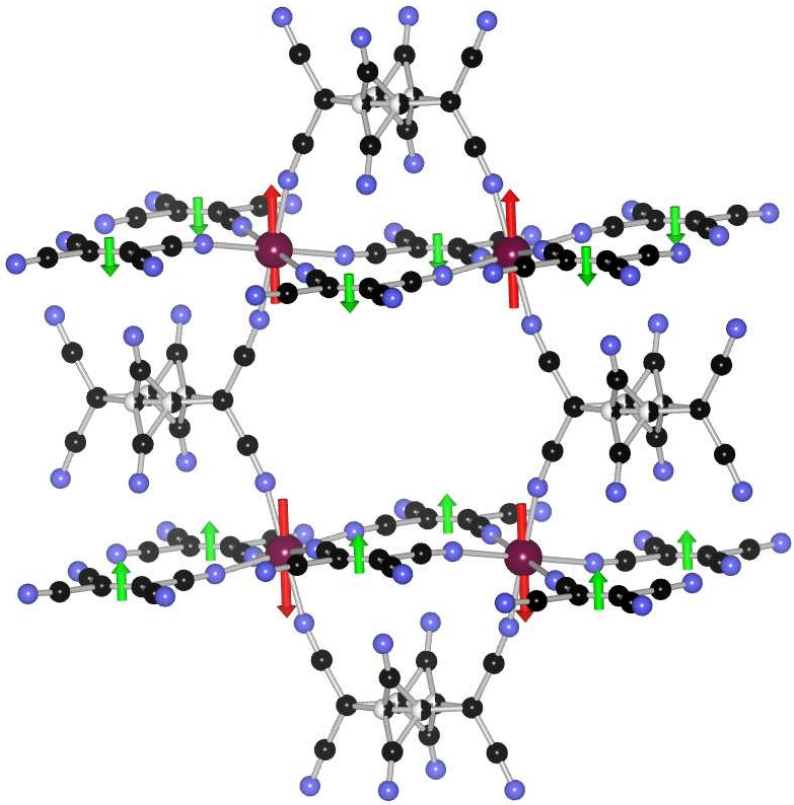

where

$$B_S(z) = \frac{2S+1}{2S}\coth\frac{2S+1}{2S}z - \frac{1}{2S}\coth\frac{z}{2S} \tag{4.4}$$

is the Brillouin function for spin S.

At high temperature or small (total) field, $B_S(x) \approx x(1+1/S)/3$, and the mean field equations can be linearized as

$$M_i \approx \frac{C_i}{T}(\pm H_0 - \sum_j \gamma_{ij} M_j), \tag{4.5}$$

with sublattice Curie constant

$$C_i = \frac{N_i g_i^2 \mu_B^2}{3k_B} S_i(S_i+1). \tag{4.6}$$

Solution of the coupled equations 4.5 gives $M_i = 0$ if $H_i = 0$ for temperatures above a critical temperature T_C, and a spontaneous magnetization below. For the familiar case of a single ferromagnetic lattice, or the Néel ordered state of a simple antiferromagnet with two sublattices,

$$T_C = 2|J|zS(S+1)/3k_B. \tag{4.7}$$

For $Mn(TCNE)_{3/2}(I_3)_{1/2}$, we take the a sublattice to be Mn^{2+} with $S_a = 5/2$ and the b and c sublattices to be in-plane and inter-plane $(TCNE)^{\bullet-}$ respectively, with $S_b = S_c = 1/2$, $z_{ab} = z_{ba} = z_{ca} = 4$, $z_{ac} = 2$, and all other $z_{ij} = 0$. Solution of the equations 4.5 gives

$$T_C = \sqrt{\gamma_{ab}\gamma_{ba}C_aC_b + \gamma_{ac}\gamma_{ca}C_aC_c}$$

$$= \frac{\sqrt{4z_{ab}z_{ba}J_{ab}^2 S_a(S_a+1)S_b(S_b+1) + 4z_{ac}z_{ca}J_{ac}^2 S_a(S_a+1)S_c(S_c+1)}}{3k_B}. \quad (4.8)$$

For Mn[TCNE][$C_4(CN)_8$]$_{1/2}$, we start by considering only the ordering within the 2-D sheets, so there are only two sublattices and one interaction. The a sublattice is $S_a = 5/2$ Mn^{2+}, and the b sublattice is $(TCNE)^{\bullet -}$, with $S_b = 1/2$, $z_{ab} = z_{ba} = 4$. The mean field transition temperature is

$$T_C = \sqrt{\gamma_{ab}\gamma_{ba}C_aC_b} = \frac{\sqrt{4z_{ab}z_{ba}J_{ab}^2 S_a(S_a+1)S_b(S_b+1)}}{3k_B}. \quad (4.9)$$

If there is an additional exchange interaction $J_{aa} < 0$ between neighboring Mn^{II} spins, with $z_{aa} = 2$, the mean field transition temperature is

$$T_C = \sqrt{\gamma_{ab}\gamma_{ba}C_aC_b + \gamma_{aa}^2 C_a^2}$$

$$= \frac{\sqrt{4z_{ab}z_{ba}J_{ab}^2 S_a(S_a+1)S_b(S_b+1) + 4z_{aa}^2 J_{aa}^2 S_a^2(S_a+1)^2}}{3k_B}. \quad (4.10)$$

For a simple, isotropic antiferromagnet, in an applied field, the lowest energy configuration is for the spins to be essentially perpendicular to the applied field direction. The spins will cant slightly in the direction of the applied field, giving the transverse susceptibility of an isotropic antiferromagnetic phase at low temperature from the usual expression [80],

$$\chi_\perp = \frac{N_a g_a^2 \mu_B}{4zJ_{aa}}. \quad (4.11)$$

This is applicable to Mn[TCNE][$C_4(CN)_8$]$_{1/2}$, because both sublattices rotate in response to the applied field.

It must be noted that mean field theory is a rough approximation for real magnetic systems, especially 2-D systems such as $Mn[TCNE][C_4(CN)_8]_{1/2}$. For example: $KNiF_3$ and K_2NiF_4 are good models of 3-D and quasi-2-D Heisenberg antiferromagnets, respectively. The ratio of their transition temperatures, 97K:246K, is much smaller than that expected from the mean field approximation, 4:6, reflective of the overestimation of the transition temperature in the 2-D system [80].

Part II

Alternative Methods for Difficult Problems

Chapter 5

p-Methylchalcone and Lessons on Meta-stable Minima

Chalcones (Fig. 5.1) are abundantly present in nature, occurring in ferns to higher plants, and tend to be highly polymorphic. In 1929, Weygand studied the polymorphic behavior of *p*-methylchalcone (Fig. 5.2) [81]. He reported the existence of three polymorphic modifications, a stable modification (I) with a melting point of 96.5°C, and two metastable modifications with melting points of 91°C and 86°C (II and III respectively). It was found that the two metastable forms readily convert to modification I in environments in which seeds of the stable form are present - behavior typical of disappearing polymorphs. Warshel *et al.* [82] reported crystallographic constants and lattice energy calculations for modification I in 1974, at which point no further studies were performed on this system until Barzky *et al.* in 2008 [83].

Figure 5.1: The chalcone molecule.

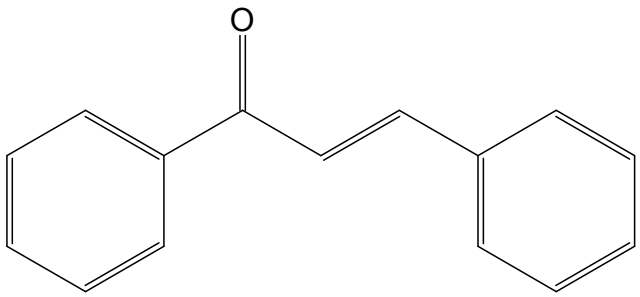

5.1 Crystal Preparation

p-Methylchalcone crystallizes in the reaction vessel upon completion of the condensation reaction of 4-methylbenzaldehyde and acetophenone. Weygand has suggested that the growth of thermodynamically unstable forms from solution crystallization is essentially impossible if the stable form has already been obtained in the same environment. The transformation of the thin needles characteristic of modification II into the chunky prisms of modification I is shown in Figure 5.3. All sample preparation was performed by Inna Barzky at Ben-Gurion University of the Negev.

As the metastable modifications were unobtainable in the presence of modification I, virgin glassware was used to carry out the synthesis. Reactions using various solvents all resulted in modification II. The crystalline habit of each modification was determined by Inna Barzky by melting and recrystallizing under a microscope (Fig. 5.4), allowing the structures later obtained to be associated with the modification identified by their melting point.

Figure 5.2: The *p*-methylchalcone molecule.

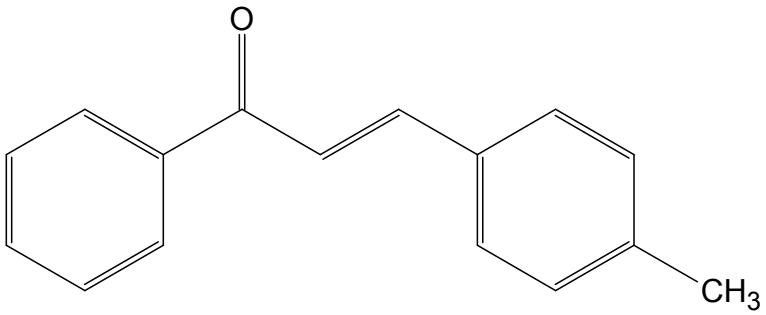

5.2 Data Collection

High resolution synchrotron X-ray powder diffraction patterns were collected on the X16C beamline at the National Synchrotron Light Source, Brookhaven National Laboratory. X-rays of wavelength 0.70030(7) Å were selected with a Si(111) double crystal monochrometer. After the sample, the diffracted beam was analyzed using a Ge(111) crystal and detected by a NaI scintillation counter. Wavelength and diffractometer zero were calibrated using a sample of NIST Standard Reference Material 1976 (a sintered plate of Al_2O_3). The sample was loaded into a thin walled glass capillary of nominal diameter 1.5mm and rotated about the longitudinal axis during data collection. Data were collected from $2\theta = 2^\circ$ to $2\theta = 35^\circ$ in steps of 0.005°. Collection times were increased from 4 seconds per point at low angle to 6 seconds at highest angle.

Figure 5.3: Microscopic observation of modification II fine needles (a), and the chunky prisms of modification I after transformation from modification II (b). Figure taken from [83].

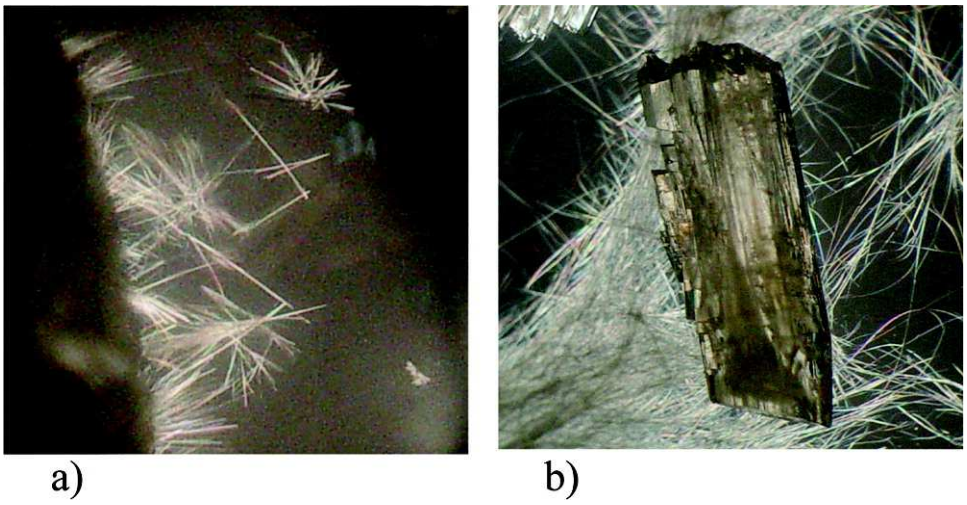

5.3 Space Group Determination

The software suite *TOPAS-Academic* was used to index the powder diffraction pattern. The most likely space group was determined to be $P2_1/c$ with lattice parameters $a = 14.162$ Å, $b = 21.874$ Å, $c = 5.913$ Å, and $\beta = 89.978°$. Because the *p*-methylchalcone molecule has very low symmetry, it is difficult to create a part of the molecule from another via symmetry operations, causing each atom in a molecule to be necessarily independent. Under the assumption that each non-Hydrogen atom in such an organic material will fill roughly 17 Å^3, each independent molecule will have a size of roughly 290 Å^3. Given that the volume of this unit cell is 1832 Å^3, we therefore expect to find 6

Figure 5.4: From left to right: melting of modification I at 97°C, crystallization of modification II from the melt at 60°C, and its subsequent melting beginning at 89°C. Figure taken from [83].

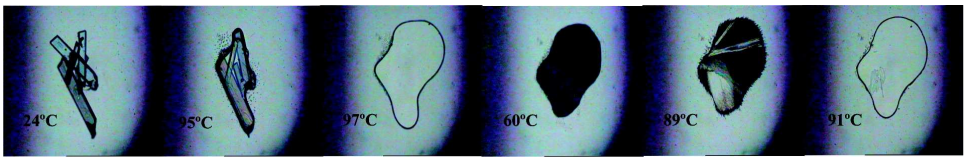

p-methylchalcone molecules in the unit cell. However, the multiplicity of the general position in space group $P2_1/c$ is 4, making 6 molecules impossible. There are two possible remedies for this conundrum, either change to a space group with a lower multiplicity of the general position, or double the unit cell. In this particular case, we are faced with another difficulty. The nearness of the angle β to 90° leaves open both the possibility that the space group is not truly monoclinic, and the possibility that we have chosen the wrong axis as being unique for the monoclinic space group.

A doubled unit cell creates the new problem that the final structure must cause a number of allowed reflections to have negligible intensity, an unlikely though not impossible scenario. A number of events conspire to make the determination of the space group for this material a very difficult matter. The nearness of β to 90° allows for very little discrimination of the unique axis, and indeed between a monoclinic and orthorhombic cell. The size of the molecule and the multiplicity of the various space groups forces the consideration of doubled cells, further expanding the number of possibilities. In order to truly

determine the correct space group, it becomes necessary to attempt a structure solution and refinement, at which point physical and chemical constraints, as well as the quality of fit, will provide the discriminating power necessary for determination of the true space group.

Table 5.1: Summary of Pawley fits for selected space group possibilities.

Space Group	a	b	c	α	β	γ	R_{wp}
$P2$	14.1634	21.8700	5.9120	90	89.939	90	7.451
$P2$	14.1651	5.9118	21.8699	90	89.915	90	7.184
$P2$	14.1630	21.8703	5.9127	90.015	90	90	7.753
$P2$	14.1617	21.8696	5.9121	90	90	89.965	7.59
$P2_1$	14.1634	21.8700	5.9120	90	89.939	90	7.418
$P2_12_12_1$	28.3250	21.8694	5.9120	90	90	90	6.986

5.4 Structure Solution

Due to the inability of Pawley fits to discriminate between a large number of possible space groups, it was necessary to attempt structure solutions in each. The simulated annealing program *DASH* [84] was used to search for structure solutions in each of the possible space groups. Many space groups were immediately eliminated upon inspection due to un-physical structures. *DASH* returned viable structures for space groups $P2_1$ (with lattice parameters $a = 14.17$ Å, $b = 21.88$ Å, $c = 5.91$ Å, and $\beta = 89.979°$ as well as $a = 14.17$ Å, $b = 5.91$ Å, $c = 21.88$ Å, and $\beta = 90.07°$) and $P2_12_12_1$ (with lattice parameters $a = 28.34$ Å, $b = 21.88$ Å, and $c = 5.91$ Å).

Subsequent refinement of structures was performed using *TOPAS-Academic*. The orthorhombic structure in space group $P2_12_12_1$ yielded a sig-

nificantly worse R_{wp} value than for the monoclinic structures. Because of the near symmetry of the molecule, each of the two monoclinic structures required the refinement of 64 configurations of the three independent molecules. Each *p*-methylchalcone molecule may be rotated by 180° about the *x*- and *z*-axes as shown in Figure 5.6, thus changing its orientation. Each molecule may be left unchanged, rotated about the *x*-axis, rotated about the *z*-axis, or rotated about the *x*- and *z*-axes, giving 4 possible orientations for each of the 3 independent molecules, resulting in 64 possible combinations. At low resolution, it will be difficult to distinguish between the different orientations. Refinements were run, starting from each of these 64 possible configurations, in which the coordinates and orientation of each molecule was refined. The carbon-carbon bond distances were refined as a single parameter constrained to be between 1.3 and 1.5 Å. The three torsion angles about the single bonds in the chain which connects the aromatic rings were allowed to refine with no constraint. The bond lengths associated with the carbon-oxygen double bond and the carbon-CH_3 bond were refined for each molecule, constrained to the range of 1.2 Å to 1.4 Å and 1.3 Å to 1.55 Å respectively. The outcome of these refinements was 64 candidate structures for each of the two $P2_1$ lattices (see Fig. 5.7). A histogram showing the R_{wp} values for the lattice with parameters $a = 14.17$ Å, $b = 21.88$ Å, $c = 5.91$ Å, and $\beta = 89.979°$ is shown in Figure 5.6, one of which is significantly preferred. This situation has occurred because the Rietveld refinement is not able to improve the fit incrementally by flipping the molecule over, and the simulated annealing process likewise gets stuck in one of the 64 nearly equal minima. Fortunately, the Rietveld refinements are able to distinguish the best one.

Having identified the correct orientation for the three independent molecules, a more complete refinement of the structure was performed. The carbon-carbon bonds were refined as four parameters, representing single, double, aromatic, and carbon-CH_3 bond lengths. The carbon-oxygen bond length was also refined as a single parameter for all three molecules. The three angles formed in the chain linking the two aromatic rings were refined, although constrained between 110° and 130°. The angle and torsion corresponding to the oxygen position were both freely refined for all molecules. The three torsions about the single bonds in the chain were allowed to refine without constraint. The torsion about the carbon-CH_3 bond was also allowed to refine independently for all molecules, this effectively determines the rotation of the three hydrogen atoms, thus the fit is relatively insensitive to changes in these parameters. The refined lattice constants were found to be $a = 14.1651(4)$ Å, $b = 21.8756(4)$ Å, $c = 5.9130(2)$ Å, and $\beta = 89.979(4)°$. The fit to the data as well as the difference is shown in Figure 5.5. There exist a few extraordinarily sharp peaks corresponding to an impurity, which we were unable to index.

Figure 5.5: Powder diffraction data points and Rietveld refinement. The residuals are shown below.

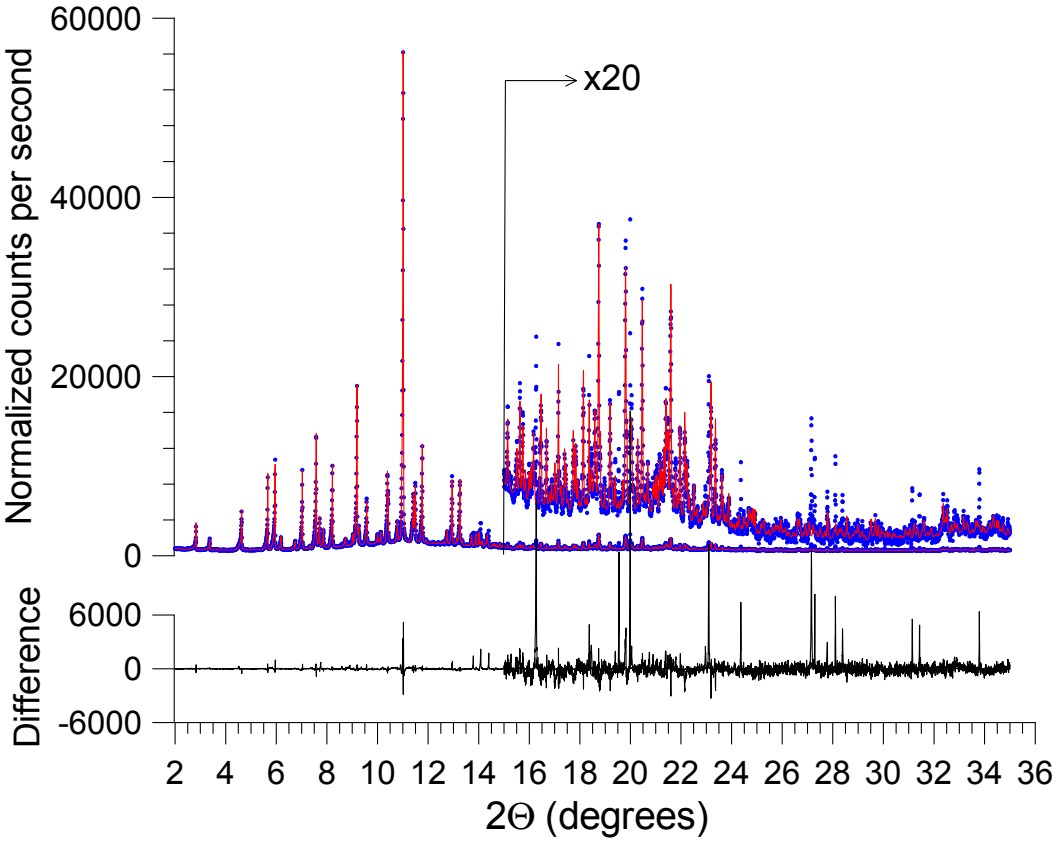

Figure 5.6: Histogram showing the distribution of R_{wp} values for the 64 possible configurations of the *p*-methylchalcone molecules. The molecule is shown with the axes of rotation leading to the possible configurations.

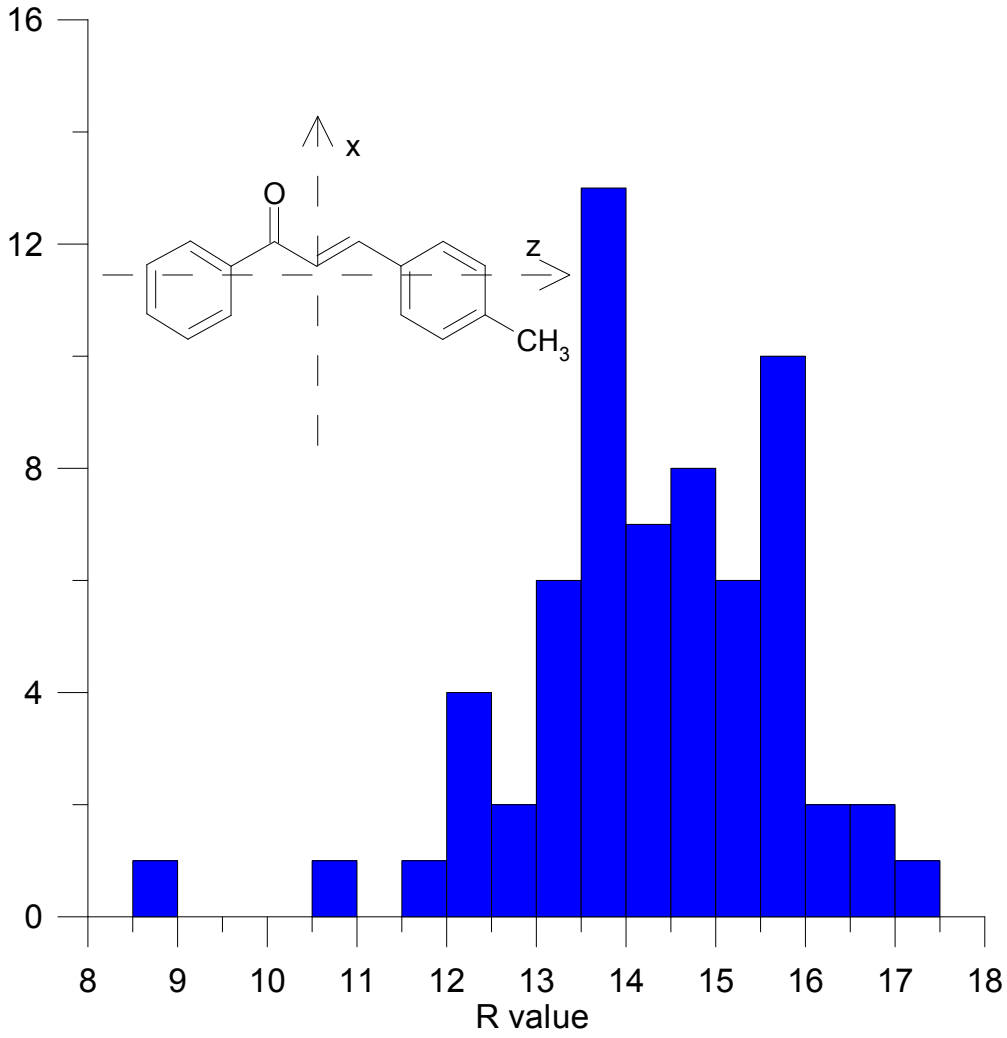

Figure 5.7: (a) Best of the candidate solutions with partial refinement and (b) Reitveld refinement and difference curve. (c) The partially refined solution provided by *DASH* and (d) Rietveld refinement and difference curve showing significantly worse fit.

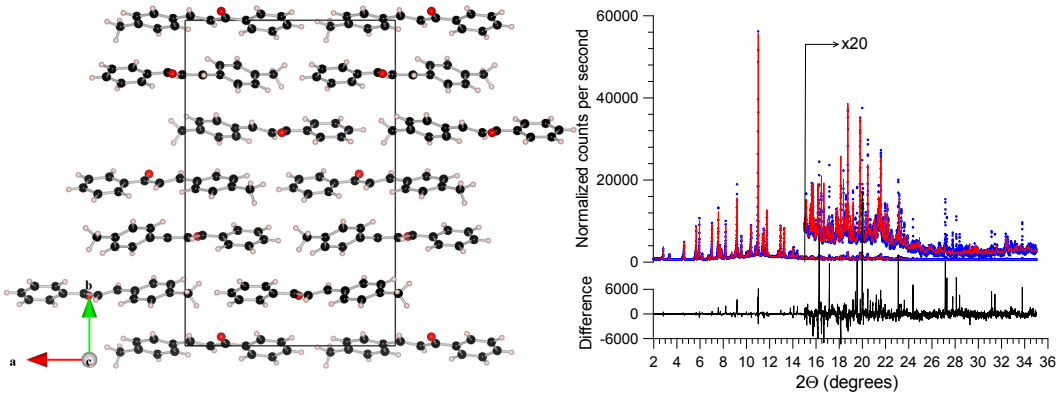

(a) (b)

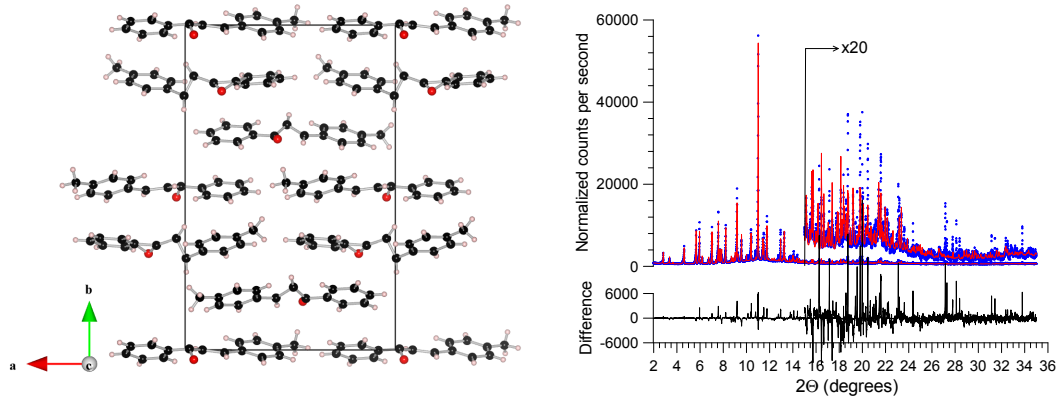

(c) (d)

Table 5.2: Experiment and Refinement Details

crystal system	monoclinic
space group	$P2_1$
a(Å)	14.1651(4)
b(Å)	21.8756(4)
c(Å)	5.9130(2)
β(°)	89.979(4)
volume(Å^3)	1832.26
Z	6
density (Mg/m^3)	1.209
R_{wp}(%)	6.518
χ^2	9.954
No. of parameters	82
Wavelength of incident radiation (Å)	0.70030(7)

Table 5.3: Bond Lengths Å

C-C single bond	1.458(7)
C-C double bond	1.390(15)
C-C aromatic bond	1.418(2)
C-CH_3 bond	1.51(1)
C-O double bond	1.31(1)
C-H bond	1 (fixed)

Table 5.4: Bond Angles and Torsions (°)

	molecule A	molecule B	molecule C
C9-C8-C7	117(2)	110(2)	112(2)
C6-C7-C8	128(1)	122(1)	126(1)
C10-C9-C8	120(1)	123(1)	120(1)
O1-C9-C8	123(2)	124(1)	128(2)
C10-C9-C8-C7	189(2)	195(1)	186(1)
C5-C6-C7-C8	-9(2)	-174(2)	205(2)
C11-C10-C9-C8	355(1)	209(1)	383(1)
O1-C9-C8-C10	189(2)	197(2)	186(2)

Chapter 6

Model Free Analysis

The use of global optimization algorithms has been crucial to the advance of structure determination from powder diffraction, especially in recent years. The ability of such methods to incorporate molecular connectivity allows for a great reduction in the number of parameters, and thus the scale of a given problem. Such methods are especially useful in the analysis of materials containing organic molecules. However, such a reduction in parameters requires knowledge of the chemical connectivity, which may not be available. In such cases, the parameter space may quickly become too large to be reasonably searched. Although there are potentially ways around this, a means of structure solution which is less model dependent is desired. There are currently two methods in use in crystallography which may be considered to be model-free: charge flipping and maximum entropy reconstruction of charge density.

The recent development of the charge flipping algorithm has exciting implications for crystallography. Although the details of its use pose significant problems for powder data, namely the effective loss of high resolution data due

to peak overlap, it has been successful in the solution of a number of structures from powder diffraction. The method is appealing in that it is nearly as model free as one could imagine, operating in space group $P1$ and with no assumptions as to the contents of the unit cell, other than positivity. Given that the method returns a real space charge density, the scale of the problem is more sensitive to the fineness with which the unit cell is sampled than to the complexity of the structure under investigation.

The method of maximum entropy to construct or to sharpen charge density maps has been well studied. It is similar to charge flipping in that it is nearly model free, resulting in a real space charge density. Normally, a constraint on the total amount of charge is imposed, implying an assumption about the unit cell contents, but this may be slackened to simply keep the total charge fixed, but not necessarily at a given value. However, the maximum entropy method does not readily converge from a completely uninformative (flat) prior density. It is often necessary to provide a reasonable starting density, which is then improved upon by the maximum entropy method until agreement with the data is achieved. In this work, it is shown that the result of charge flipping may act as the prior for a maximum entropy analysis with no consideration of atoms or molecules along the way. Such a process results in a charge density superior to that of charge flipping alone, into which atoms may then be placed in order to form a structure which is ready for Rietveld refinement.

6.1 Data Collection and Initial Attempts at Structure Solution

Powder diffraction data was collected at beamline X16C at the National Synchrotron Light Source at Brookhaven National Laboratory. The sample, nominally $Zn(SC_6H_4S)$(dien) (dien = diethylenetriamine), was loaded into a 0.7 mm thin-walled glass capillary, and spun during data collection. X-rays of 0.697 Å wavelength were selected with a Si(111) double crystal monochromator and analyzed with a Ge analyzer crystal. *TOPAS-Academic* was used to index the pattern to a lattice of $a = 43.5955$ Å, $b = 8.7976$ Å, $c = 18.8542$ Å, $\beta = 73.8657°$ with extinction symbol $C1c1$. Such a volume corresponds to 10 formula units in the unit cell. The structure was modeled in space group $C2/c$ as two Zn atoms in the general position with a third located on a special position, and similarly for the SC_6H_4S units, which were treated as Z-matrices. Three diethylenetriamine molecules were placed in general positions with all torsion angles free to refine. This resulted in a model with, at best, 48 structural parameters. Assumptions as to the geometry of the diethylenetriamine molecules could have reduced this number, had they been known, but even eliminating all of the torsion angles would leave at least 36 parameters. The possibility of space group Cc would have greatly increased this number, and was not seriously considered due to this added difficulty. Despite the daunting scale of the problem, attempts were made to solve the structure via simulated annealing in the programs *TOPAS-Academic*, *DASH*, and *PSSP* [85], none of which met with any success.

6.2 The Model Free Approach

Using intensities extracted from a Pawley fit in *TOPAS-Academic*, attempts were made to solve the structure using the program *Superflip* [86]. Although, at first glance, the resulting charge density showed little promise, elimination of the smaller density peaks left what were easily identified as Zn atoms, some of which were tetrahedrally surrounded by atoms of roughly half the charge, quickly identified as sulfur. Although no attempt to do so was made, at this point it was likely possible to locate the phenol rings based on finding the appropriate sulfur to sulfur distances. Instead, this charge map was modified by setting any pixels below a given threshold to zero, and then used as the prior for a maximum entropy analysis. This modification was necessary for two reasons, one being the residual pixels of small but negative intensity, the other being to decrease bias from artifacts in the charge flipping map. The threshold was set in such a way that the only remaining features were of a size with those identified as Zn or S atoms as shown in Figure 6.1a.

Using the modified charge density obtained from charge flipping as our prior, we performed a maximum entropy analysis, using as the χ^2 constraint the lowest 500 extracted intensities along with the full covariance matrix obtained from the Pawley fit [12]. A limited range of peaks was used to decrease the necessary computation time, although more could readily have been included had better resolution been required. The maximum entropy map revealed the location of the phenol rings, as demonstrated in Figure 6.1b, and gave a good indication of the location and orientation of the diethylenetriamines, which turned out to be in a ratio of 1.2 instead of 1 to the $Zn(SC_6C_4S)$

formula unit. At that point, it only remained to put atoms in their respective positions so that a Rietveld refinement might be performed, the results of which are shown in Figure 6.1c. The structure obtained from this model-free approach was easily refined to give excellent agreement with the measured diffraction pattern, as seen in Figure 6.2.

6.3 Conclusions

Although great strides in powder diffraction have come about thanks to the ability to incorporate as much prior information as possible, we have demonstrated at least one case in which the structure solution process is simplified by ignoring such information. The charge flipping algorithm is capable of finding the largest features in the density map, but not the smaller ones. However, the result of charge flipping is sufficiently close to the correct density to serve as a starting point for refinement via the maximum entropy method. Such an approach is roughly analogous to the heavy atom approach, wherein the heaviest atoms are located and the partial structure used in concurrent iterations of Fourier recycling in order to locate the lighter atoms. Although a structural model with atoms and molecules is necessary for the final step of Rietveld refinement, it may be beneficial to ignore such considerations during the stage of structure solution.

Figure 6.1: The structure solution process for $Zn(SC_6H_4S)(dien)_{1.2}$. (a), the charge density obtained from *Superflip* with only the largest features shown for clarity. (b), a phenol ring identified in the maximum entropy map with the final structure superimposed. (c), the final, Rietveld refined structure, imaged with *VESTA* [87].

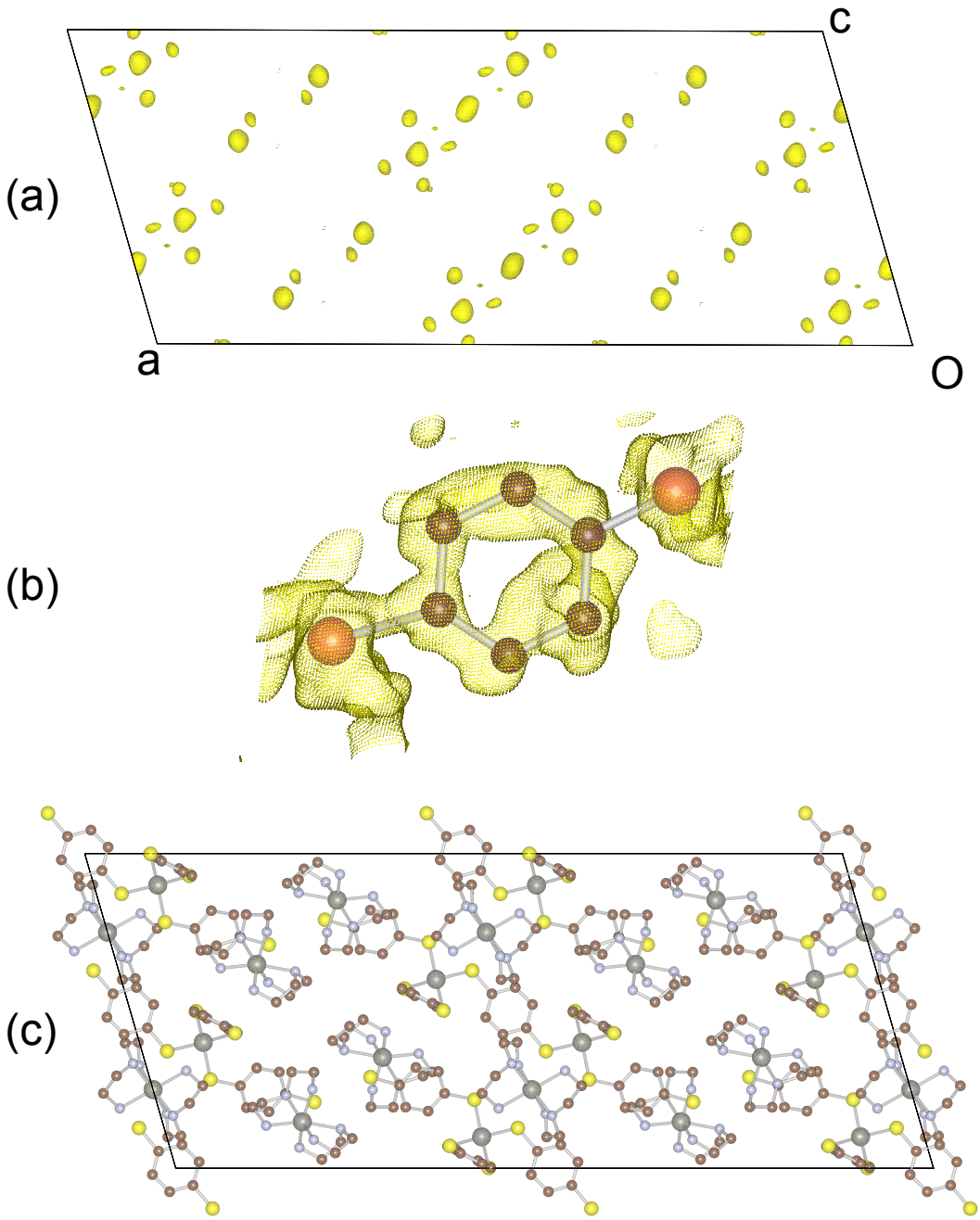

Figure 6.2: The X-ray powder diffraction pattern for $Zn(SC_6H_4S)(dien)_{1.2}$. Data is shown as the blue points, the Rietveld fit as the red line, and the difference shown in black below. The tick marks indicate the position of allowed peaks.

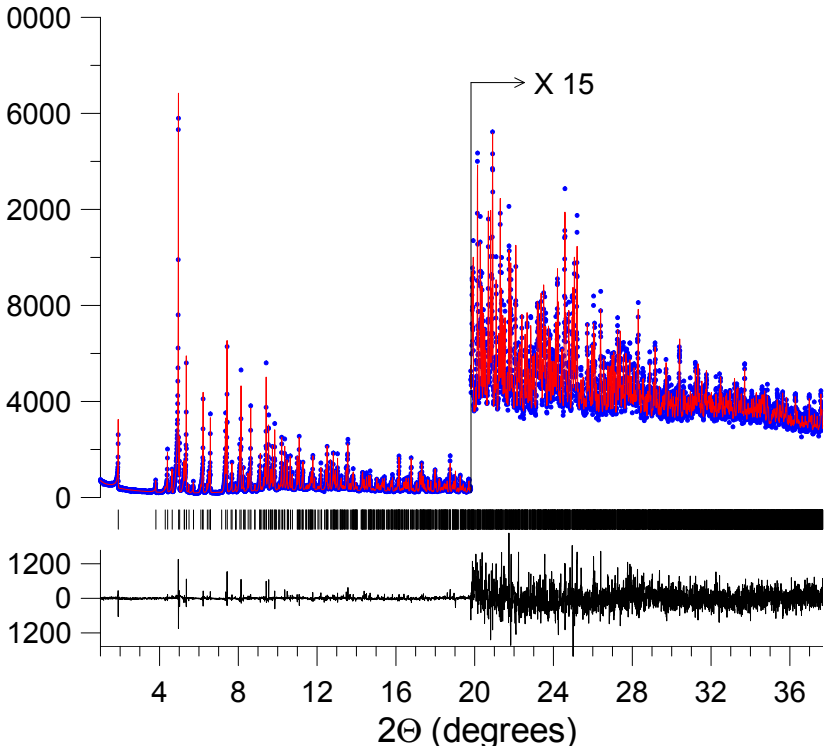

Chapter 7

Robust Rietveld Refinement in the Presence of Unmodeled Impurities

The Rietveld method has gained widespread use in the analysis of powder diffraction data. Often the last step in a structure solution, the Rietveld refinement of a model to the entire diffraction profile is crucial for the extraction of reliable structural parameters. This is commonly done by the use of a least-squares minimization routine. Such least-squares minimization, however, is predicated on the model under consideration being an accurate description of the data. Commonly with powder samples, an unidentifiable impurity is present, which contributes to the data, but defies description by the model. In such cases, the least-squares analysis, so commonly used, is poorly justified.

David [39] developed an approach based on Bayesian statistics able to deal with the presence of impurities in the powder diffraction pattern, an

approach termed robust refinement. The effect of an impurity is to create a large number of positive outliers in the data. The idea of robust statistics is to associate a lesser penalty with such outliers, an idea formalized in the development of a new target function for minimization. In this work, a means of converting standard least-squares to this robust target function using the framework available in current Rietveld refinement programs is presented. Test cases of moderate complexity are presented, as are several examples of the technique applied to previously unsolved structures.

7.1 Implementation in *TOPAS-Academic*

The following discussion, included for completeness, closely follows that of David [39]. Consider the case in which a model, M_i, is a good representation of a measured set of data points, D_i, with their associated standard errors, σ_i (the subscript i will index the value of the model and the data and standard error associated with a given point in the powder diffraction profile). In a Bayesian approach, we may ask what is the probability of the model, given the data and any other information available to us, I. This is expressed as

$$p(\{M_i\}|\{D_i\}, I), \tag{7.1}$$

where {} indicates the entire dataset. Under the assumption of the usual Gaussian counting statistics, the familiar (unreduced)

$$\chi^2 \equiv \sum_i w_i (Y_{i,obs} - Y_{i,calc})^2, \tag{7.2}$$

can be derived as

$$\chi^2 = \sum_i -2 \ln [p(M_i|D_i, I)], \tag{7.3}$$

so that the minimum χ^2 corresponds to the maximum probability that the model is correct.

Henceforth, we work with each data point separately. In order to treat the case of an unknown impurity, we must consider that we do not have full knowledge of the model, M_i. Instead, we consider the model to be a sum of a known, refinable part, R_i, which is due both to the background and to the known phase, and an unknown peak contribution, A_i. We then wish to marginalize the unknown peak contribution from our analysis, allowing us to consider only the refinable part of the model. This gives, for the ith data point,

$$p(R_i|D_i, I) = \int_0^\infty p(R_i, A_i|D_i, I) dA_i. \tag{7.4}$$

According to Bayes' Theorem

$$p(R_i, A_i|D_i, I) = \frac{p(D_i|R_i, A_i, I) p(A_i, R_i|I)}{p(D_i|I)} \tag{7.5}$$

where $p(D_i|I)$ is just a constant, so we may write

$$p(R_i|D_i, I) \propto p(R_i|I) \int_0^\infty p(D_i|A_i, R_i, I) p(A_i|I) dA_i. \tag{7.6}$$

In order to evaluate this integral, we would need to know the probability distribution for A_i, which we do not know. David therefore assumed a scale-

free Jeffreys' distribution for A_i [88] leading to

$$p(R_i|D_i, I) \propto \int_0^\infty A_i^{-1} \exp\left[-(A_i + R_i - D_i)^2/2\sigma_i^2\right] dA_i. \tag{7.7}$$

This may then be used to obtain the robust version of χ^2, summed over the full set of data:

$$\chi^2_{RR} = \sum_i -2 \ln\left[p(R_i|D_i, I)\right]. \tag{7.8}$$

Although the integral derived for (7.7) cannot be evaluated analytically, numerical approximation allows for the fitting of χ^2_{RR} by convenient functional forms.

Figure 7.1: Comparison of χ^2 (dotted line) and χ^2_{RR} (solid line), figure taken from [39].

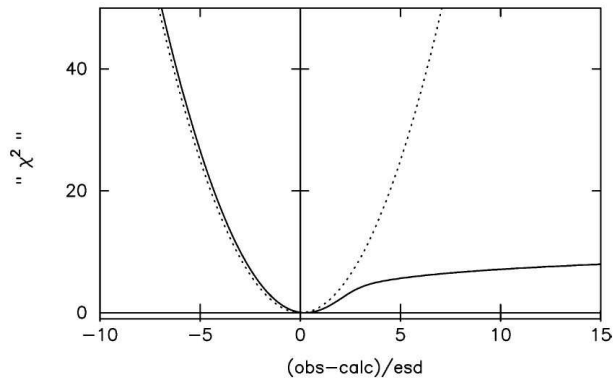

Inspection of χ^2_{RR} (Fig. 7.1) reveals that it is essentially equal to the usual χ^2 in the cases where the data exceeds the model by no more than the measured uncertainty, $(Y_{i,obs} - Y_{i,calc}) \leq \sigma_i$. It is only in the case that $(Y_{i,obs} - Y_{i,calc}) > \sigma_i$ that the two differ. In the robust version, we have allowed for the possibility of

impurities, and so will penalize a model relatively weakly for failing to account for such data.

In order to make use of the many readily available programs written for Rietveld refinement, we have found a way of converting the ordinary χ^2 to the robust version. This is not easy to accomplish directly in most Rietveld programs in current use, but it can be done by re-weighting the data at each iteration of the refinement to effectively transform χ^2 to χ^2_{RR}. Having defined χ^2 through (7.2), we need only to determine the correct function for the weights, w_i. Considering the contribution to χ^2 by a single data point, and equating that to the target function,

$$\chi^2_i = w_i(Y_{i,obs} - Y_{i,calc})^2 = \chi^2_{RR} = -2\ln[p(M|D,I)], \tag{7.9}$$

we find

$$w_i = \frac{-2\ln[p(M|D,I)]}{(Y_{i,obs} - Y_{i,calc})^2}. \tag{7.10}$$

It now only remains to implement this weighting scheme in our refinement program. For this work, this was done using the program *TOPAS-Academic*. *TOPAS-Academic* has the useful feature that it supports user defined functions and gives access to the weighting scheme used for refinement, which can be updated at each iteration. For speed of operation, (7.8) was replaced by a

polynomial and a logarithmic function such that

$$\chi^2_{RR} = \begin{cases} t^2 & \text{if } t < 0.8 \\ \sum_{n=0}^{10} A_n t^n & \text{if } 0.8 \leq t \leq 21 \\ \alpha \ln(t) + \beta & \text{if } 21 < t. \end{cases} \tag{7.11}$$

with $t = \frac{1}{\sigma_i^2}(Y_{i,obs} - Y_{i,calc})^2$. A total of thirteen parameters were chosen for fitting the functional form of χ^2_{RR}, but these need only be determined once.

One further complication to be considered is that *TOPAS-Academic* does not actually minimize χ^2, working with R_{wp} instead. In common usage, this difference is purely aesthetic, the difference being only the scaling factor $R_{exp} \equiv \sqrt{\frac{N-P}{\sum w_i Y^2_{i,obs}}}$, where N is the number of data points, P the number of parameters, w_i the weight for point i, and $Y_{i,obs}$ the observed intensity at point i. However, for our purposes, this scaling factor is not a constant, but changes as we adjust the weights. As the weights are calculated for the next iteration, the value of R_{exp} is determined by the previous iteration. Once convergence is reached, this is not an issue, as explained in more detail in Appendix A. We have implemented this in *TOPAS-Academic* through the following macro:

```
macro Robust_Refinement ()
{
'Rescale peaks according to robust refinement algorithm
prm test = Get(r_exp); :31.62037
prm N = (1/test)^2; :  0.00100
prm !p0  =0.40007404;
prm !p1  =-2.5949286;
prm !p2  =4.3513542;
prm !p3  =-1.7400101;
prm !p4  =3.6140845 * 10^-1;
prm !p5  =-4.5247609 * 10^-2;
prm !p6  =3.5986364 * 10^-3;
prm !p7  =-1.8328008 * 10^-4;
prm !p8  =5.7937184 * 10^-6;
prm !p9  =-1.035303 * 10^-7;
prm !p10 =7.9903166 * 10^-10;
prm t = ((Yobs - Ycalc)/SigmaYobs);
weighting = If( t < 0.8,
              (1/Max(SigmaYobs^2, 1))*N,
              If(t < 21, N*((((((((((p10*t + p9)*t + p8)*t + p7)
              *t + p6)*t + p5)*t + p4)*t + p3)
              *t + p2)*t + p1)*t +p0)/(Yobs - Ycalc)^2,
              N*(2.0131 * Ln(t) + 3.9183)/(Yobs - Ycalc)^2));
recal_weighting_on_iter
}
```

7.2 A Conceptual Demonstration

In order to demonstrate the principles at work, we will take as an example a portion of a diffraction pattern consisting of three partially overlapped peaks. We will fit this data as simply three peaks with no consideration of any underlying lattice or structure. The centers and intensities of the three peaks will be allowed to refine independently, with a refinable width common to all three, giving the fit shown in Figure 7.2.

Figure 7.2: The fit to three peaks of arbitrary intensity, center, and with a common width

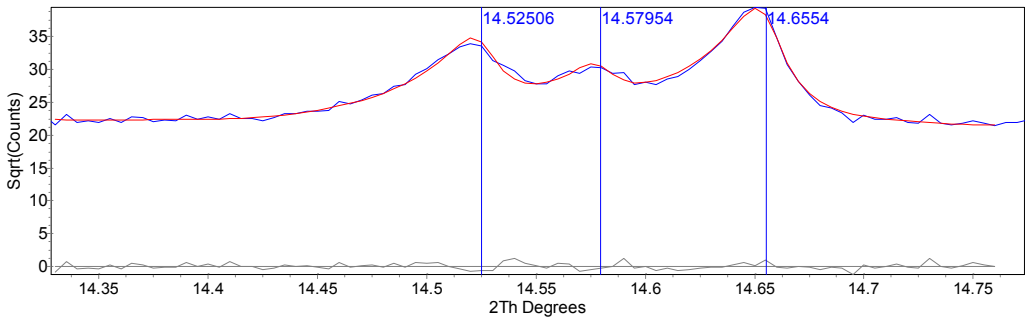

The potential for failure inherent in using the usual χ^2 metric for an incomplete model is best illustrated by the, perhaps overly contrived, demonstration of what happens if we are to fix the location of the peaks, and remove the highest angle peak.

Figure 7.3: The resulting fit of only the first two peaks, with centers held fixed, to the three peak data as above using the usual χ^2 metric.

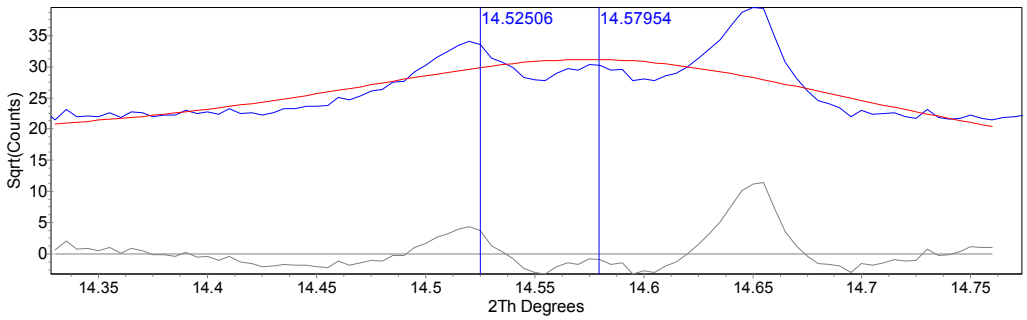

The failure in this case is striking, and demonstrates the tendency for a refinement to broaden out the available peaks in order to give some intensity

to regions of the pattern where the model allows for no peaks, but the data clearly requires them (Fig. 7.3). Of course, we have in a sense forced this result by fixing the peak locations.

If we allow them to refine, starting from the locations, widths, and intensities found from the refinement of all three peaks, meaning we start from the "correct" starting values, we do slightly better.

Figure 7.4: The resulting refinement of only two peaks (the first two) to the three peak data, this time allowing the peak locations to refine along with the intensities and the overall width according to χ^2.

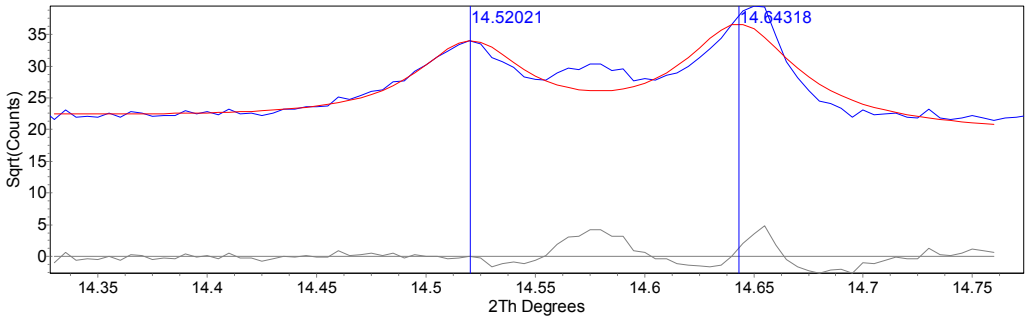

The failure in this case is less striking, but still clear. It is also interesting to note that the smallest peak, the middle one, has moved over to coincide more fully with the largest peak, the third. This is because the χ^2 statistic would prefer to fit the largest features in the data, and can do this by moving a small peak to the location of a larger one (Fig. 7.4). This will not happen in general, as it will not usually be associated with a monotonic improvement in the fit, but it is possible, as demonstrated here. Also, the overall fit is still quite poor and the peaks are overly broadened, as is typical in such cases.

We will now consider the case in which we use the robust version of χ^2 as the underlying metric in our Rietveld refinement. We begin with a recreation of our second refinement, in which we will fix the first two peaks at the correct locations and allow only the intensities and the width to refine.

Figure 7.5: The robustly refined version of the second refinement, with the first two peaks fixed in location and the intensities and overall width allowed to freely refine.

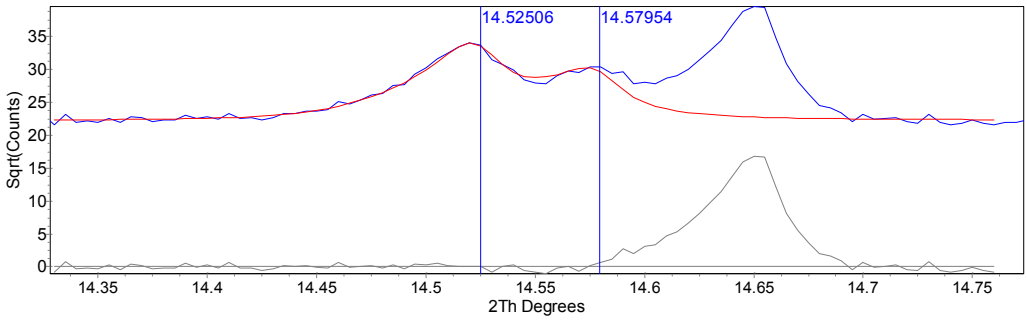

In this case, we have completely missed the third peak, but the fit to the first two is quite good (Fig. 7.5). While a quick inspection of the difference curve would seem to indicate that we have done a very poor job of fitting our data, we simply need to remember that the third peak was not included in our model, and so we should not expect to have fit it at all, exactly what we have done.

As a further test, we can recreate the third refinement, in which we also allow the peak locations to refine, this time using the robust metric.

Again, we note that we have completely missed the third peak, as we should, given our underlying model (Fig. 7.6). A close inspection reveals that

Figure 7.6: The robust version of the third refinement, in which the locations of the first two peaks additionally allowed to refine.

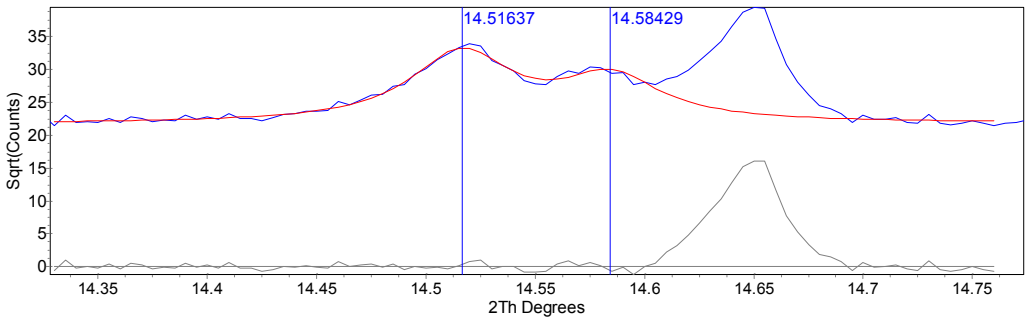

our peaks have moved slightly, with the second peak moving to slightly higher angle in order to fit some of the low angle tail of the third peak. However, it is clear that our model is being refined in order to fit as much of the data as possible, with little regard for those regions which cannot be accounted for.

7.3 Tests on Mixtures of Acetaminophen and Ibuprofen

7.3.1 Experimental Data

With a conceptual idea of how a refinement should behave when using the robust refinement approach, we can now implement this in a structural refinement. For this, we will consider mixtures of acetaminophen and ibuprofen prepared from commercial tablets. High resolution synchrotron X-ray powder diffraction patterns were collected at the X16C beamline at the National Syn-

chrotron Light Source at Brookhaven National Laboratory. X-rays of wavelength 0.6981 Å were selected using a Si(111) channel-cut monochromator. After the sample, the diffracted beam was analyzed with a Ge(111) crystal and detected by a NaI scintillation counter. Wavelength and diffractometer zero were calibrated using a sample of NIST Standard Reference Material 1976, a sintered plate of Al_2O_3. Samples were flame sealed in thin-walled glass capillaries of nominal diameter 1.0 mm and spun during data collection for improved powder averaging. Diffraction patterns were collected up to 2θ values of 32° in steps of 0.005°. Counting times were increased from 1 second at low angle to 4 seconds at higher angles to improve counting statistics.

7.3.2 Refinement Details

The composition of each mixture was determined by a simultaneous Rietveld refinement of all phases present. A small amount of lactose monohydrate was found to be present in the ibuprofen sample. The mixtures were found to consist of ibuprofen:acetaminophen:lactose weight ratios of 68:25:7, 56:38:6, 28:69:3, 19:79:2 and 6:93:1. Starting from published structures [89, 90, 91], each mixture was refined in three separate ways. First, each mixture was refined with all phases being modeled, referred to as a dual Rietveld refinement. This gave a refined percentage of each phase present, as well as a best-case scenario structural refinement. The second refinement was done using the Rietveld method with only one phase modeled, referred to as a single Rietveld refinement. Thirdly, each mixture was refined using the robust method in which only one of the phases present was modeled. In all refinements, the

contribution from β-lactose was included in the ibuprofen model as a second phase, but its structure was not refined in any way. Comparison of the refined structures was made between the three refinement procedures and the refined structures from the pure samples.

In all refinements, both the ibuprofen and acetaminophen molecules were refined via Z-matrices. In both molecules, chemically similar parameters, such as the C-C single bond length, were refined as a single parameter, while all angles and torsions, excepting those pertaining to the aromatic rings, were freely refined. The ring was constrained to remain a planar, regular hexagon, the only refined parameter being the aromatic bond length. Further details are contained in the supplementary materials.

7.3.3 Results

By considering the average atomic deviation from the true structure as a function of concentration (Figs. 7.7 and 7.8), we may gain a general sense of the effectiveness of this method. It is clear that the robust refinement procedure consistently outperforms the single-phase Rietveld method when impurities are present, while in the pure samples, Rietveld and robust refinements result in essentially equivalent structures. Given high levels of impurity, it is still preferable to model all phases present, although the robust method greatly extends the level of impurity that may be tolerated in the case that the impurity cannot be identified. Even at concentrations of only 28%, the ibuprofen structure bears a close resemblance to the true structure (Fig. 7.9), whereas the single phase Rietveld method fails catastrophically (Fig. 7.10).

Figure 7.7: Average deviation, in Å, from the true structure for each of the three refinement methods used for the acetaminophen structure.

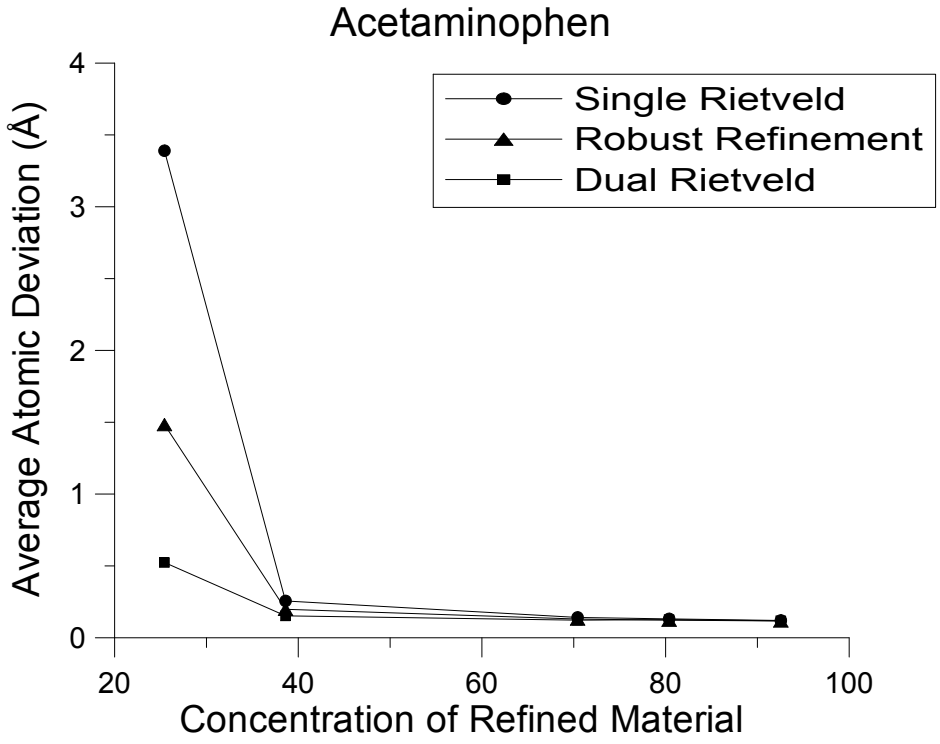

While the accuracy of the refined structure is the truest test of this new method, perhaps the clearest example of the concept is seen in the difference curve. The difference curve resulting from a robust refinement should correspond, in the ideal case, exactly to that of the impurity. This would indicate that the refinement is guided only by the portion of the data that comes from the phase being modeled. Figure 7.11 demonstrates this for the case of ibuprofen in the presence of a 69% acetaminophen impurity. Although both the robust and single-phase Rietveld refinements (Fig. 7.11a and c) manage to fit only a small portion of the diffraction pattern intensity, the difference curve

Figure 7.8: Average deviation, in Å, from the true structure for each of the three refinement methods used for the ibuprofen structure.

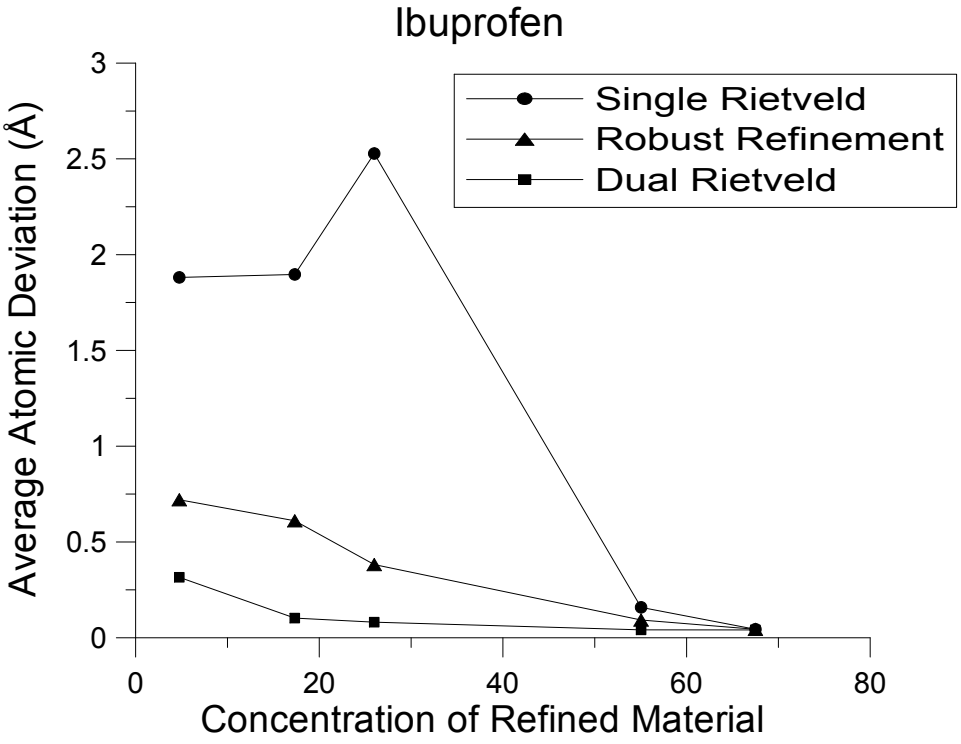

resulting from the robust refinement (Fig. 7.11d) bears a striking resemblance to that computed for the acetaminophen structure (Fig. 7.11e). On the other hand, the difference curve resulting from the single-phase Rietveld refinement (Fig. 7.11f) clearly shows that the model has been biased to fit an impurity peak while giving a poor fit to the first peak seen, which actually belongs to the phase under consideration. Of course, if possible, it is preferable to fit all phases of the sample (Fig. 7.11b), in order to make use of all available information.

Figure 7.9: Overlay of the ibuprofen molecule from Rietveld refinement of the pure sample, shown in grey and red for the oxygen atoms, with the robustly refined structure from the sample containing 28% ibuprofen, shown in black.

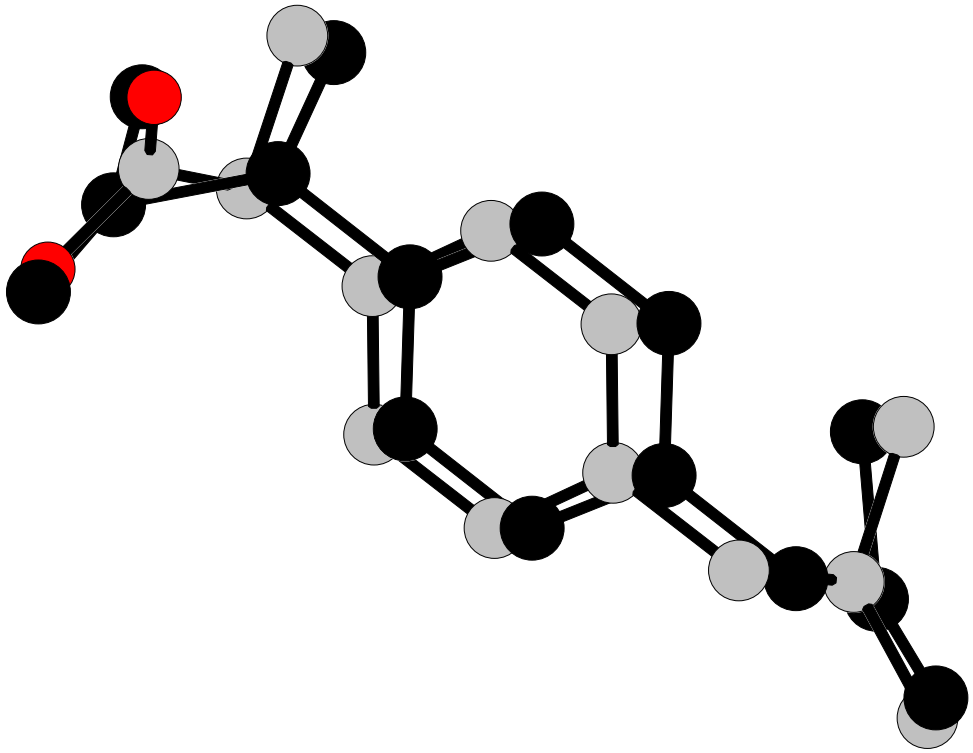

7.4 Application to Previously Unsolved Structures

Encouraged by the success of this method with test samples of known composition, we have applied it to two materials with previously unknown structures [38, 92], one of which is discussed in chapter 3.

Figure 7.10: Overlay of the ibuprofen molecule from Rietveld refinement of the pure sample, shown in grey and red for the oxygen atoms, with the single-phase Rietveld refined structure from the sample containing 28% ibuprofen, shown in black.

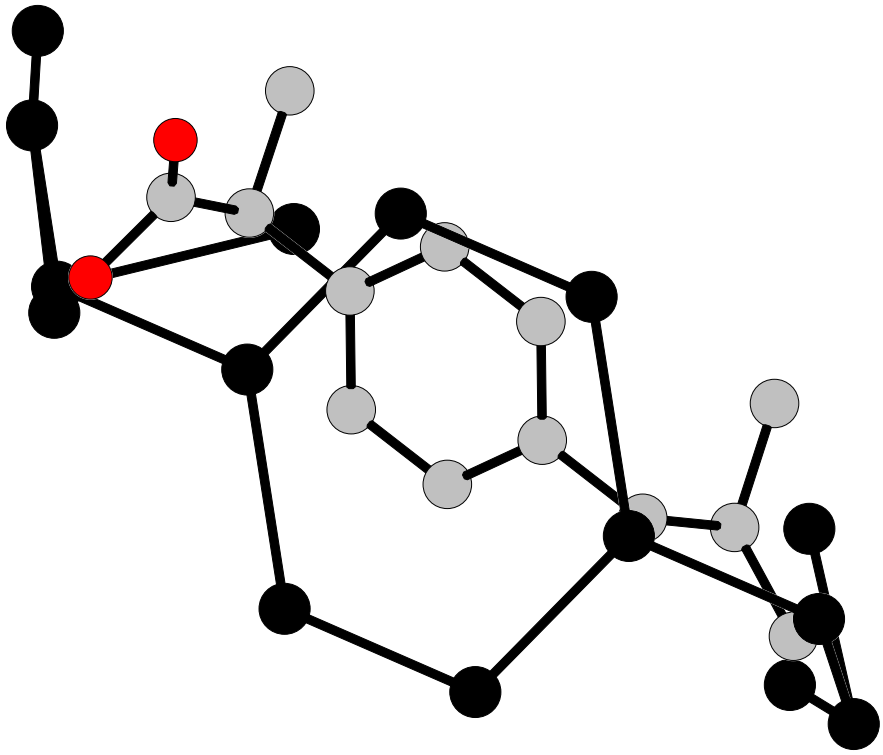

7.4.1 $Ag(pyz)_2S_2O_8$

Powder diffraction data was collected on a sample of $Ag(pyz)_2S_2O_8$. Attempts to index the data were unsuccessful, leading to the conclusion that the sample contained multiple phases. Repeating the measurement five months later, it was noted that a number of the peaks had decreased drastically in intensity, while others were left unchanged or increased (Fig. 7.12). It was hypothesized that one of the phases was undergoing a transformation into another of the

already present phases, accounting for the disappearing peaks as well as the strengthening peaks. Using only the disappearing peaks, it was possible to find a lattice in space group $C2/c$ with lattice parameters of $a = 15.969$ Å, $b = 7.133$ Å, $c = 14.586$ Å, and $\beta = 124.973°$.

The majority of the peaks associated with the remaining phase were indexed by space group $C2$ with lattice parameters of $a = 14.342$ Å, $b = 7.185$ Å, $c = 7.412$ Å, and $\beta = 104.024°$. This indexing accounted for the majority of the impurity peaks at low angle, but failed for the full profile. Using only the low-angle data where the impurity peaks could be modeled by this lattice, a Pawley fit was used to account for the impurity while the disappearing phase was solved using a simulated annealing algorithm in the program *TOPAS-Academic*. A structure, shown in Figure 7.13, was hypothesized and refined according to the robust procedure described above, converging to a value of $\chi^2_{RR} = 3.157$. The Pawley fit was abandoned at the refinement stage in order to utilize the full pattern, for which the Pawley fit was a poor model of the impurity, and to reduce the total number of parameters being refined. Attempts to find a structure for the remaining phase have, so far, not been successful. However, this is unsurprising as there is no concrete evidence that the remaining phase consists of the same chemical formula, or is even a single phase. Subsequent preparation of a single-phase sample of this material confirmed the structure obtained using the robust method [92].

7.5 Conclusion

We have successfully implemented robust refinement using the widely available Rietveld program *TOPAS-Academic*. To the best of the authors' knowledge, *TOPAS* is unique in having the convenient feature of being able to reassess the weights used in refinement at each iteration. The procedure described above may, however, be generalized for use with any Rietveld program without modification, if the step of redefining the weights is performed externally to the refinement program. In such cases, a single refinement cycle would be performed, and the results passed to a "helper" program which would rewrite the weights before passing the data back to the Rietveld program for the subsequent cycle of refinement. In addition, we hope that our successful tests of David's robust refinement principle will motivate the authors of other Rietveld software to incorporate this feature into their programs.

Robust refinement allows one to refine a structure from data containing an impurity phase with no knowledge of the composition of the impurity, nor even the certainty of its existence. The method was found to be consistently better than single-phase Rietveld refinement in the presence of unmodeled impurities when tested on pharmaceutical test cases, and the two produced similar results in the case of pure samples. Further, the method has been used to refine two, previously unknown, structures of organo-metallic materials. These structures were both subsequently confirmed by the availability of pure samples.

While this method has been demonstrated to work, and is of obvious usefulness, there are many unanswered questions still to be addressed. The most important of these: How may one be confident in a structural refinement car-

ried out using the robust method? In Rietveld refinement, it is customary to apply three criteria before a structure is believed to be correct. The structure should make chemical sense, a criterion that may still be considered in the robust case. The structure should also be stable under refinement, meaning that if the atoms are allowed to move freely, the structure is essentially unchanged, a criterion that is also applicable to the robust case. The third is that of a featureless difference curve, which is not met in the case of unmodeled impurities. In light of this, one must be especially careful before accepting a model as correct and should make every effort to identify the impurity present. Conveniently, the method of robust refinement in the presence of unidentified impurities should actually facilitate this, as the difference curve should isolate the diffraction pattern of the impurity, simplifying identification. It is obviously preferable to perform a Rietveld analysis taking account of all of the observed phases. But, when that is not possible, the use of a robust refinement may allow extraction of significant information otherwise hidden.

Figure 7.11: Robust refinement (a.) and difference (d.), dual-phase Rietveld refinement (b.), single-phase Rietveld refinement (c.) and difference (f.) of the ibuprofen phase in the mixture containing 28% ibuprofen. The calculated pattern for the unmodeled impurity (e.) is shown for comparison. The difference curve from the robust refinement clearly corresponds to that of acetaminophen whereas that from the single-phase Rietveld refinement does not.

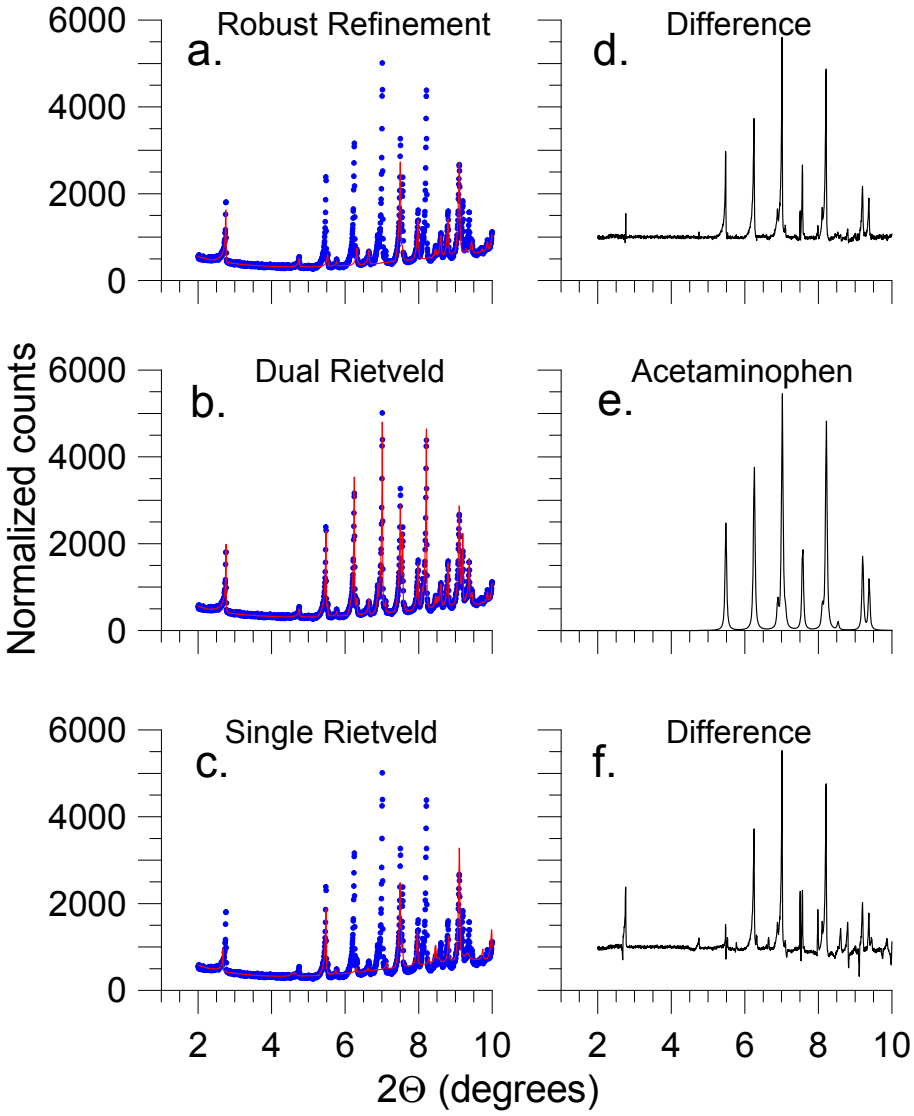

Figure 7.12: Low angle data collected on the sample of $Ag(pyz)_2S_2O_8$ when first received, shown in red, and five months later, shown in black. It is clearly seen that some peaks have decreased in intensity, indicative of a transforming phase.

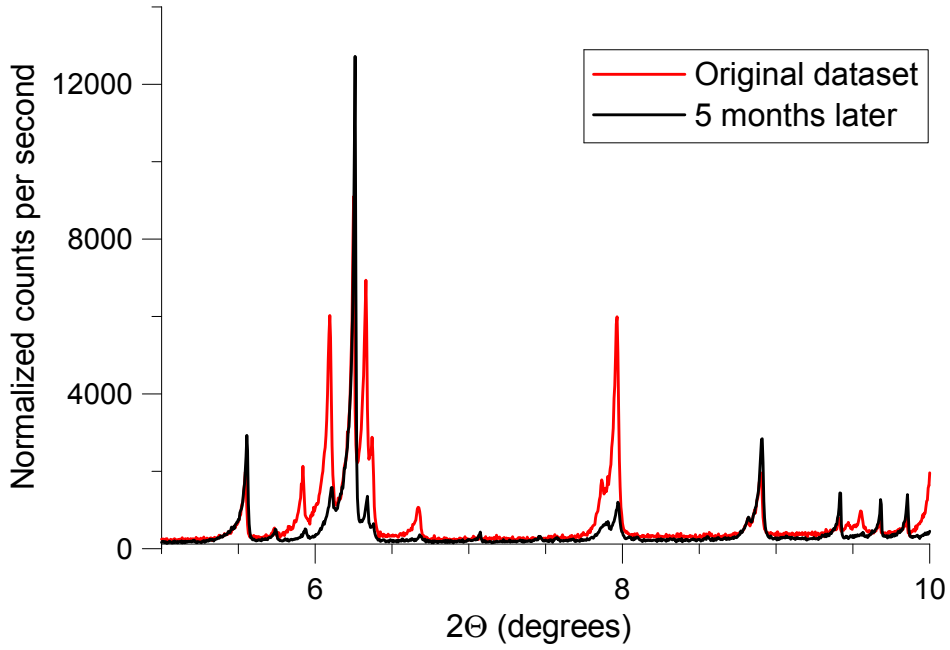

Figure 7.13: The robustly refined structure for the disappearing phase of $Ag(pyz)_2S_2O_8$ as viewed along the *b*-axis (a). The Ag atoms are nearly octahedrally coordinated by four pyrazine rings and two peroxodisulfates. This forms square planar networks of Ag and pyrazine (b) separated by the peroxodisulfates.

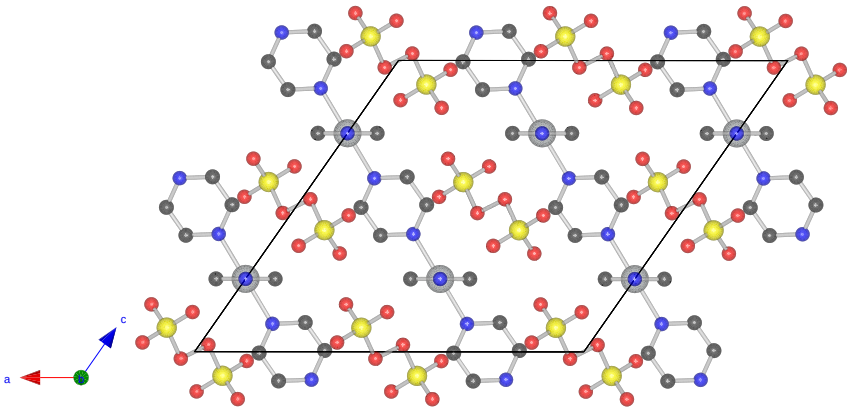

(a)

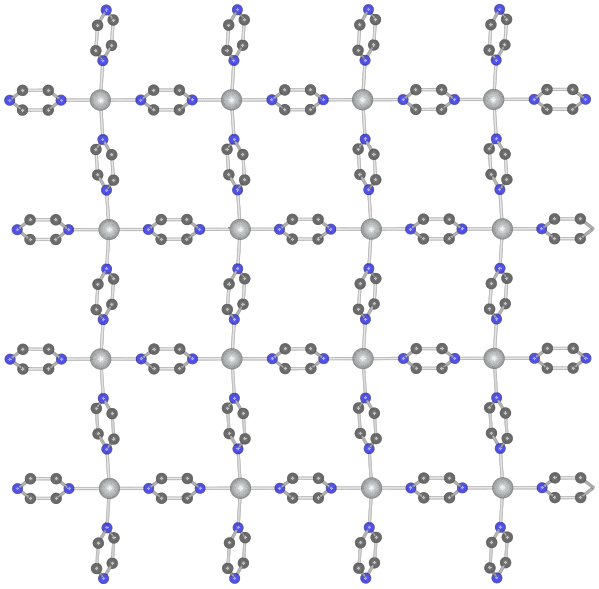

(b)

Bibliography

[1] G. H. Hardy and W. W. Rogosinski. *Fourier Series*. Dover Publications, 1999.

[2] J. Karle and H. Hauptman. *Acta Cryst.*, 3:181–187, 1950.

[3] A. J. C. Wilson. *Acta Cryst.*, 2:318–321, 1949.

[4] J. S. Kasper and K. Lonsdale, editors. *International Tables for X-Ray Crystallography*, volume II. The Kynoch Press, 1959.

[5] W. I. F. David, K. Shankland, L. B. McCusker, and Ch. Baerlocher, editors. *Structure Determination from Powder Diffraction*. Oxford University Press, 2002.

[6] N. Metropolis, A. W. Rosenbluth, M. N. Rosenbluth, A. H. Teller, and E. Teller. *J. Chem. Phys.*, 21:1087–1092, 1953.

[7] V. Favre-Nicolin and R. Cerny. *J. App. Cryst.*, 35:734–743, 2002.

[8] G. Oszlanyi and A. Suto. *Acta Cryst. A*, 64:123–134, 2008.

[9] G. Oszlanyi and A. Sueto. *Acta Cryst. A*, 63:156–163, 2007.

[10] H. M. Rietveld. *Acta Cryst.*, 22:151–&, 1967.

[11] H. M. Rietveld. *J. App. Cryst.*, 2:65–&, 1969.

[12] J. H. Her. *Ab initio structure determination from powder diffraction and maximum entropy image reconstruction*. PhD thesis, Stony Brook University, 2007.

[13] M. Takata, E. Nishibori, M. Sakata, M. Inakuma, E. Yamamoto, and H. Shinohara. *Phys. Rev. Lett.*, 83:2214–2217, 1999.

[14] T. Noritake, S. Towata, M. Aoki, Y. Seno, Y. Hirose, E. Nishibori, M. Takata, and M. Sakata. *J. Alloys Compd.*, 356:84–86, 2003.

[15] J. Netzel and S. van Smaalen. *Acta Cryst. B*, 65:624638, 2009.

[16] C. Giacovazzo, H. L. Monaco, D. Viterbo, F. Scordari, G. Gilli, G. Zanotti, and M. Catti. *Fundamentals of Crystallography.* Oxford University Press, 2000.

[17] W. I. F. David and K. Shankland. *Acta Cryst. A*, 64:52–64, 2008.

[18] J. Bernstein. *Polymorphism in Molecular Crystals.* Oxford University Press, 2002.

[19] A. A. Ebert Jr. and H. B. Gottlieb. *J. Am. Chem. Soc.*, 74:28062810, 1952.

[20] W. O. Ayuko, D. Kinchington, and T. Ng. *PCT Int. Appl.*, page 81, 1997.

[21] D. Kinchington, T. Ng, N. Mathews, M. Tisdale, D. Devine, and W. O. Ayuko. *Antiviral Chem. Chemother.*, 8:121130, 1997.

[22] M. Kuhnert-Brandstätter and M. Riedmann. *Microchim. Acta*, 2:107120, 1987.

[23] I. Barsky, J. Bernstein, P. W. Stephens, and K. H. Stone. *New J. Chem.*, 32:1747–1753, 2008.

[24] J. Bernstein, R. J. Davey, and J.-O. Henck. *Angew. Chem., Int. Ed.*, 38:3443, 1999.

[25] A. A. Coelho. *TOPAS-Academic.* TOPAS-Academic is available online., 2007.

[26] C. Weygand. *Berichte*, 57:413, 1924.

[27] C. Weygand and A. Matthes. *Liebigs Ann.*, 449:29, 1926.

[28] C. Weygand and H. Baumgartel. *Liebigs Ann.*, 469:225, 1929.

[29] C. Weygand and L. Mensdorf. *Berichte*, 68:1825, 1935.

[30] F. Toda, K. Tanaka, and M. Kato. *J. Chem. Soc., Perkin Trans*, 1:1315–1318, 1998.

[31] I. Barsky, J. Bernstein, J. O. Henck, K. H. Stone, and P. W. Stephens. *In Preparation.*

[32] A. March. *Z. Krist.*, 81:285–297, 1932.

[33] P. W. Stephens. *J. Appl. Cryst.*, 32:281–289, 1999.

[34] N. W. Ashcroft and N. D. Mermin. *Solid State Physics*. Thomson Learning, 1976.

[35] G. N. Schrauzer and H. Prakash. *Inorg. Chem.*, 14(5):1200–1204, 1975.

[36] C. W. Dirk, M. Bousseau, P. H. Barrett, F. Moraes, F. Wudl, and A. J. Heeger. *Macromolecules*, 19(2):266–269, 1986.

[37] D. L. Turner, T. P. Vaid, P. W. Stephens, K. H. Stone, A. G. DiPasquale, and A. L. Rheingold. *J. Am. Chem. Soc.*, 130(1):14+, 2008.

[38] D. L. Turner, K. H. Stone, P. W. Stephens, and T. P. Vaid. *In Preparation*.

[39] W. I. F. David. *J. App. Cryst.*, 34:691–698, 2001.

[40] I. L. Abrahams, C. D. Garner, and W. Clegg. *J. Chem. Soc., Dalton Trans.*, pages 1577–1579, 1987.

[41] A. Altomare, R. Caliandro, M. Camalli, C. Cuocci, C. Giacovazzo, A. G. G. Moliterni, and R. Rizzi. *J. App. Cryst.*, 37:1025–1028, 2004.

[42] J. S. Miller, J. C. Calabrese, H. Rommelmann, S. R. Chittipeddi, J. H. Zhang, W. M. Reiff, and A. J. Epstein. *J. Am. Chem. Soc.*, 109(3):769–781, 1987.

[43] D. Davidson and L. A. Welo. *J. Phys. Chem.*, 32:1191–1196, 1928.

[44] F. Herren, P. Fischer, A. Ludi, and W. Halg. *Inorg. Chem.*, 19(4):956–959, 1980.

[45] Y. Liao, W. W. Shum, and J. S. Miller. *J. Am. Chem. Soc.*, 124(32):9336–9337, 2002.

[46] T. E. Vos, Y. Liao, W. W. Shum, J. H. Her, P. W. Stephens, W. M. Reiff, and J. S. Miller. *J. Am. Chem. Soc.*, 126(37):11630–11639, 2004.

[47] W. W. Shum, J. H. Her, P. W. Stephens, Y. Lee, and J. S. Miller. *Adv. Mater.*, 19:2910, 2007.

[48] Z. Z. Gu, O. Sato, T. Iyoda, K. Hashimoto, and A. Fujishima. *J. Phys. Chem.*, 100(47):18289–18291, 1996.

[49] Z. Z. Gu, O. Sato, T. Iyoda, K. Hashimoto, and A. Fujishima. *Chem. Mater.*, 9(5):1092–1097, 1997.

[50] J. B. Ayers and W. H. Waggoner. *J. Inorg. & Nucl. Chem.*, 31(7):2045, 1969.

[51] S. M. Holmes and G. S. Girolami. *Mol. Cryst. Liq. Cryst. Sci. Technol., Sect. A*, 305:279–290, 1997.

[52] D. F. Mullica, D. B. Tippin, and E. L. Sappenfield. *J. Cryst. Spect. Res.*, 21(1):81–85, 1991.

[53] Y. S. You, J. H. Yoon, J. H. Lim, H. C. Kim, and C. S. Hong. *Inorg. Chim. Acta*, 360(8):2523–2531, 2007.

[54] H. Z. Kou, S. Gao, B. Q. Ma, and D. Z. Liao. *Chem. Comm.*, (8):713–714, 2000.

[55] H. Z. Kou, J. K. Tang, D. Z. Liao, S. Gao, P. Cheng, Z. H. Jiang, S. P. Yan, G. L. Wang, B. Chansou, and J. P. Tuchagues. *Inorg. Chem.*, 40(19):4839–4844, 2001.

[56] L. V. Zorina, M. Gener, S. S. Khasanov, R. P. Shibaeva, E. Canadell, L. A. Kushch, and E. B. Yagubskii. *Synth. Met.*, 128(3):325–332, 2002.

[57] M. Clemente-Leon, E. Coronado, J. R. Galan-Mascaros, C. Gimenez-Saiz, C. J. Gomez-Garcia, and J. M. Fabre. *Synth. Met.*, 103(1-3):2279–2282, 1999.

[58] D. B. Soria, M. E. C. Villalba, O. E. Piro, and P. J. Aymonino. *Polyhedron*, 21(18):1767–1774, 2002.

[59] H. Z. Kou, E. Q. Gao, D. Z. Liao, P. Cheng, Z. H. Jiang, S. P. Yan, G. L. Wang, X. K. Yao, H. G. Wang, and J. P. Tuchagues. *Acta Chem. Scand.*, 53(8):542–546, 1999.

[60] B. S. Kennon, K. H. Stone, P. W. Stephens, and J. S. Miller. *CrystEngComm*, 11(10):2185–2191, 2009.

[61] B. S. Kennon, K. H. Stone, P. W. Stephens, and J. S. Miller. *In Preparation.*

[62] J. M. Manriques, G. T. Lee, R. S. McLean, A. J. Epstein, and J. S. Miller. *Science*, 252, 1991.

[63] C. Tengstedt, M. P. de Jong, A. Kanciursewska, E. Carlegrim, and M. Fahlman. *Phys. Rev. Lett.*, 96, 2006.

[64] S. J. Blundell and F. L. Pratt. *J. Phys.: Condens. Matter*, 16, 2004.

[65] J. S. Miller and A. J. Epstein. *Angew. Chem., Int. Ed.*, 33, 1994.

[66] V. I. Ovcharenko and R. Z. Sagdeev. *Russ. Chem. Rev.*, 68, 1999.

[67] V. N. Prigoden, N. P. Raju, K. I. Pokhodnya, J. S. Miller, and A. J. Epstein. *Adv. Mater.*, 14, 2002.

[68] K. I. Pokhodnya, M. Bonner, J. H. Her, P. W. Stephens, and J. S. Miller. *J. Am. Chem. Soc.*, 128, 2006.

[69] J. Zhang, J. Ensling, V. Ksenofontov, P. Gutlich, A. J. Epstein, and J. S. Miller. *Angew. Chem., Int. Ed.*, 37, 1998.

[70] K. H. Stone, P. W. Stephens, A. C. McConnell, E. Shurda, K. I. Pokhodnya, and J. S. Miller. *In Preparation.*

[71] J. H. Her, P. W. Stephens, K. I. Pokhodnya, M. Bonner, and J. S. Miller. *Angew. Chem., Int. Ed.*, 46, 2007.

[72] A. Girtu, C. M Wynn, J. Zhang, J. S. Miller, and A. J. Epstein. *Phys. Rev. B*, 61, 2000.

[73] P. Stoltz and S. Pohl. *Z. Naturfor, B*, 43:175, 1988.

[74] R. C. Teitelbaum, S. L. Ruby, and T. J. Marks. *J. Am. Chem. Soc.*, 100:3215, 1978.

[75] M. Mizuno, J. Tanaka, and I. Harada. *J. Phys. Chem.*, 85:1789, 1981.

[76] K. I. Pokhodnya, M. Bonner, A. G. DiPasquale, A. L. Rheingold, and J. S. Miller. *Chem. Eur. J.*, 14:714–720, 2008.

[77] G. Wang, C. Slebodnick, and G. T. Yee. *Inorg. Chem.*, 46:9641–9645, 2007.

[78] $Mn(TCNE)_{3/2}(I_3)_{1/2}$ – Space Group = *Cmmm*; a = 13.170(2) Å, b = 15.926(3) Å, c = 7.6087(2) Å, V = 1595.9(3) Å^3, T = 25°C, Z = 4, R_{wp} = 0.0506, χ^2 = 2.972, CCDC Reference Number 745884; $Mn[TCNE][C_4(CN)_8]_{1/2}$ – Space group = *Cmmm*; a = 14.515(3) Å, b = 17.538(3) Å, c = 7.4551(2) Å, V = 1897.9(4) Å^3, T = 25°C, Z = 4, R_{wp} = 0.0651, χ^2 = 1.988, CCDC Reference Number 745885.

[79] The analysis included here roughly follows that of J.S. Smart, *Amer. J. Phys.*, 23:356, 1955.

[80] L. J. de Jongh and A. R. Miedema. *Experiments on Simple Magnetic Model Systems*. Taylor & Francis, 1974. p. 63.

[81] C. Weygand. *Lieb. Ann.*, 472:143, 1929.

[82] A. Warshel, E. Huler, D. Rabinovich, and Z J. Shakked. *Mol. Struct.*, 23:175191, 1974.

[83] I. Barsky, J. Bernstein, P. W. Stephens, K. H. Stone, E. Cheung, M. B. Hickey, and J. O. Henck. *Cryst. Growth & Des.*, 8:63–70, 2008.

[84] W. I. F. David, K. Shankland, J. van de Streek, E. Pidcock, W. D. S. Motherwell, and J. C. Cole. *J. App. Cryst.*, 39:910–915, 2006.

[85] S. Pagola, P. W. Stephens, D. S. Bohle, A. D. Kosar, and S. K. Madsen. *Nature*, 404:307–310, 2000. While the subject of this article is not the program *PSSP*, this is the first, and best, description of the method employed by the program.

[86] Palatinus L. and Chapuis G. *J. App. Cryst.*, 40:786–790, 2007.

[87] K. Momma and F. Izumi. *J. Appl. Cryst.*, 41:653–658, 2008.

[88] H. Jeffreys. *Theory of Probability*. Oxford University Press, 1961.

[89] J. F. McConnell. *Cryst. Struct. Commun.*, 3:73, 1974.

[90] M. Haisa, S. Kashino, R. Kawai, and H. Maeda. *Acta Cryst. B*, 32:1283, 1976.

[91] K. Hirotsu and A. Shimada. *Bull. Chem. Soc. Jpn.*, 47:1872, 1974.

[92] J. L. Manson, K. H. Stone, H. I. Southerland, T. Lancaster, A. J. Steele, S. J. Blundell, F. L. Pratt, P. J. Baker, R. D. McDonald, P. Sengupta, J. Singleton, P. A. Goddard, C. Lee, M.-H. Whangbo, M. M. Warter, C. H. Mielke, and P. W. Stephens. *J. Am. Chem. Soc.*, 131:4590–4591, 2009.

[93] B. H. Toby. *Powder Diffraction*, 21:67–70, 2006.

Appendix A

Discussion of Fitting Criteria in *TOPAS-Academic*

It is useful to take a careful look at the computations performed by *TOPAS-Academic* when we implement the robust weighting scheme described above. *TOPAS-Academic* actually minimizes the quantity

$$R_{wp}^2 = \frac{\sum_i w_i (Y_{i,obs} - Y_{i,calc})^2}{\sum_i w_i Y_{i,obs}^2} \tag{A.1}$$

instead of

$$\chi^2 = \frac{\sum_i w_i (Y_{i,obs} - Y_{i,calc})^2}{N - P}. \tag{A.2}$$

Although we have previously used the unreduced form of χ^2, we henceforth use the reduced form as defined in (A.2) in this Appendix, as it is the form computed by *TOPAS-Academic*. If we use a standard weighting scheme based on the statistical uncertainty of each data point, determined simply from counting statistics, then these two differ merely by a constant of proportionality which is $R_{exp}^2 = \frac{N-P}{\sum w_i Y_{i,obs}^2}$, such that

$$R_{wp}^2 = \chi^2 R_{exp}^2. \tag{A.3}$$

Complications arise, however, when we allow our weighting scheme to change as the refinement progresses. R_{exp} is no longer a constant, but will depend on the weights at a given iteration. In fact, if we insert the function for our

weights, we see that, at iteration n,

$$R^2_{exp}(n) = \frac{(N-P)R^2_{exp}(n-1)}{\sum \frac{\chi^2_{RR}}{(Y_{obs}-Y_{calc})^2} Y_{obs} o^2}. \tag{A.4}$$

As the refinement nears convergence, the number $\frac{(N-P)}{\sum \frac{\chi^2_{RR}}{(Y_{obs}-Y_{calc})^2} Y^2_{obs}}$ becomes nearly constant and R_{exp} grows geometrically. Given that the weights are inversely proportional to R^2_{exp}, this would seem catastrophic. However, since all of the weights are multiplied by a common factor, we may just normalize χ^2_{RR} by the same factor and eliminate the problem. One significant consequence of this, however, is the meaning of the reported value of R_{wp}. The weights were altered to effectively change this from the standard definition to the robust metric χ^2_{RR}. What is actually reported as R_{wp}, however, is

$$\sqrt{\frac{(N-P)}{\sum \frac{\chi^2_{RR}}{(Y_{obs}-Y_{calc})^2} Y^2_{obs}} \chi^2_{RR}}. \tag{A.5}$$

The difference arises because the normalization of χ^2_{RR} is done using the value of R_{exp} from the previous iteration instead of the current one. Once R_{exp} reaches the stage at which it behaves geometrically (when convergence is approached), this difference is unimportant except for obtaining the correct value for χ^2_{RR} to report.

Having obtained the correct value for χ^2_{RR}, one should ask what is the significance of this value, if any? Even with data from pure samples, the meaning of the numerical value of χ^2 is hardly straightforward, see [93]. In the robust case especially, it is difficult to define a threshold below which a fit may be considered correct. While the contribution to χ^2_{RR} from the impurity peaks is greatly down-weighted, it still constitutes a non-zero addition. Thus χ^2_{RR} will rise with the level of impurity present in the sample, even in the case of a perfect fit for the refined phase. Ultimately, the quality of a fit is determined not by the value of χ^2_{RR} achieved, but rather the certainty that a lower value cannot be found. For the purposes of refinement, which works from the assumption that our starting point is not so far from the global minimum, we need not worry about ensuring that the minima refined to is the global one, merely that the local minima is correctly found. In order to extend the method to that of structure solution, however, such issues will need to be addressed.

Appendix B

List of Publications and Solved Structures

B.1 Publications

Semiconducting Lead-Sulfur-Organic Network Solids
Dayna L. Turner, Thomas P. Vaid, Peter W. Stephens, Kevin H. Stone, Antonio G. DiPasquale, and Arnold L. Rheingold
J. Am. Chem. Soc. **2008** *130*(1), 14-15. doi: 10.1021/ja0770983

Disappearing and Reappearing Polymorphism in p-Methylchalcone
Inna Barsky, Joel Bernstein, Peter W. Stephens, Kevin H. Stone, Eugene Cheung, Magali B. Hickey, and Jan-Olav Henck
Cryst. Growth Des. **2008** *8*(1), 63-70. doi: 10.1021/cg7007733

Superconductivity in $LaFe_{1-x}Co_xAsO$
Athena S. Sefat, Ashfia Huq, Michael A. McGuire, Rongying Jin, Brian C. Sales, David Mandrus, Lachlan M. D. Cranswick, Peter W. Stephens, and Kevin H. Stone
Phys. Rev. B **2008** 78, 104505. doi: 10.1103/PhysRevB.78.104505

The study of the polymorphic system of 2-chloro-4-nitrobenzoic acid
Inna Barsky, Joel Bernstein, Peter W. Stephens, and Kevin H. Stone
New J. Chem. **2008** 32, 1747-1753. doi: 10.1039/b812017j

Implementation and use of robust refinement in powder diffraction in the presence of impurities
Kevin H. Stone, Saul H. Lapidus, and Peter W. Stephens
J. Appl. Cryst. **2009** 42, 385-391. doi: 10.1107/S0021889809008450

Characterization of the antiferromagnetism in $Ag(pyz)_2(S_2O_8)$ (pyz = pyrazine) with a two-dimensional square lattice of Ag^{2+} ions
Jamie L. Manson, Kevin H. Stone, Heather I. Southerland, Tom Lancaster, Andrew J. Steele, Stephen J. Blundell, Francis L. Pratt, Peter J. Baker, Ross D. McDonald, Pinaki Sengupta, John Singleton, Paul A. Goddard, Changhoon Lee, Myung-Hwan Whangbo, Michelle M. Warter, Charles H. Mielke, and Peter W. Stephens
J. Am. Chem. Soc. **2009** 131, 4590-4591. doi: 10.1021/ja9005223

Interpenetrating Diruthenium Tetraformate Monocation, $[Ru^{II/III}{}_2(O_2CH)_4]^+$, Based 3-D Molecule-based Magnets
Bretni S. Kennon, Kevin H. Stone, Peter W. Stephens, and Joel S. Miller,
CrystEngComm **2009** 11, 2185-2195. doi: 10.1039/B906437K

Cadmium Thiolate and Selenolate Anionic Network Solids
Dayna L. Turner, Kevin H. Stone, Peter W. Stephens, and Thomas P. Vaid
In Preparation

A New Family of 3-D Network-Structured Organic-Based Magnets
Kevin H. Stone, Peter W. Stephens, Amber C. McConnell, Endrit Shurdha, Konstantin I. Pokhodnya, and Joel. S. Miller
In Preparation

Preparation and Structure of $[Ru_2^{II/III}(O_2CMe)_4]_2[Fe(CN)_5NO]$ and Magnetically Ordered $H_x[Ru_2^{II/III}(O_2CMe)_4]_{3-x}[Cr(CN)_5NO]$ Possessing Interpenetrating Lattices
Bretni S. Kennon, Kevin H. Stone, Peter W. Stephens, and Joel S. Miller
In Preparation

B.2 Structures

Details of structures discussed in this work are available through the Cambridge Structural Database (CCDC).

Table B.1: Solved structures and CCDC reference numbers

Material	**CCDC Code**
2-chloro-4-nitrobenzoic acid	700780-700784
p'-Methylchalcone	757369
$[Cd(en)_3][Cd(SC_6H_4)_2]$	704799
$[Cd(en)_3][Cd(SeC_6H_4Se)_2]$	704801
$[Zn(en)_3][Zn(SC_6H_4S)_2]$	704802
$[Mg_{0.82}Cd_{0.18}(en)_3][Cd_{0.98}Mg_{0.02}(SC_6H_4S)_2]$	704800
$[NMe_4]_2[Cd_2(SC_6H_4S)_3]$	704803
$[NEt_4]_2[Cd_2(SC_6H_4S)_3]$	704804
$[NMe_4]_2[Cd_2(SeC_6H_4Se)_3]$	704805
$Pb_2(S_2C_6H_2S_2)(en)$	678534
$Pb_3(C_6S_6)$	678535
$Pb_3(SeC_6H_4Se)_3(en)_2$	757370
$Tl_2(SC_6H_4S)$	757367
$Tl_2(SeC_6H_4Se)$	757368
$[Ru_2(O_2CH)_4]_3[Co(CN)_6]$	709218
$[Ru_2(O_2CH)_4]_3[Fe(CN)_6]$	709219
$[Ru_2(O_2CMe)_4]_3[Cr(CN)_5NO]$	749333
$[Ru_2(O_2CMe)_4]_2[Fe(CN)_5NO]$	749334
$Mn(TCNE)_{3/2}(I_3)_{1/2}$	745884
$Mn[TCNE][C_4(CN)_8]_{1/2}$	745885
p-Methylchalcone	652154
$Zn(SC_6H_4S)(dien)_{1.2}$	757366
$Ag(pyz)_2S_2O_8$	702323